ION BEAM ENHANCED GRAIN GROWTH
in
THIN FILMS

by

Harry Albert Atwater, Jr.

S.B., Massachusetts Institute of Technology
(1982)

S.M., Massachusetts Institute of Technology
(1983)

Submitted to the Department of
Electrical Engineering and Computer Science
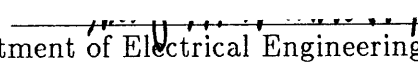In Partial Fulfillment of the Requirements
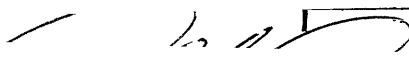For the Degree of

DOCTOR OF PHILOSOPHY

at the

MASSACHUSETTS INSTITUTE OF TECHNOLOGY
March, 1987

©Massachusetts Institute of Technology

Signature of Author _____
Department of Electrical Engineering and Computer Science
March 27, 1987

Certified by _____
Henry I. Smith
Thesis Supervisor

Certified by _____
Carl V. Thompson
Thesis Supervisor

Accepted by _____
Arthur C. Smith
Chairman, Departmental Committee on Graduate Students

ION BEAM ENHANCED GRAIN GROWTH IN THIN FILMS

by
Harry A. Atwater, Jr.
Submitted to the Department of Electrical Engineering and Computer
Science
on February 1, 1987 in partial fulfillment of the requirements for the
Degree of Doctor of Philosophy in
Electrical Engineering and Computer Science

Abstract

A research program has been established to study ion beam enhanced grain growth (IBEGG). Ion beam enhanced grain growth has been studied experimentally in Ge, Au and Si films. IBEGG has been characterized by varying the ion dose, ion energy, ion flux, ion species, temperature, and thin film deposition conditions. The effect of these parameters on grain size and microstructure has been analyzed both qualitatively and quantitatively using transmission electron microscopy (TEM).

A transition state model has been developed to describe the motion of grain boundaries during ion bombardment. The model has three criteria, which are based on experimental observations and simple assumptions: first, only elastic collisions at or very near grain boundaries contribute to enhanced grain growth; second, heating of the film by inelastic collisions has a negligible effect on grain growth; and third, ion bombardment does not influence the driving force for grain boundary migration. The model accounts for the dependence of IBEGG on the experimental parameters cited above. An atomistic picture of the jump rate at grain boundaries during IBEGG is presented. Monte-Carlo simulation of ion range and defect production was performed using the TRIM code and a modified Kinchin Pease formula. The calculated defect yield per incident ion was found to be directly related to enhanced grain growth, and was used to estimate the number of atomic jumps at the grain boundary per defect generated at the boundary for a given driving force. The IBEGG and thermal growth rates are related to their respective point defect populations.

Also described is a study of the correlation of strain and microstructure during ion beam enhanced grain growth and thermal annealing of polycrystalline Ge films. Raman spectroscopy was employed as a probe of biaxial strain in the thin Ge films. The first-order Stokes Raman peak at 304 cm^{-1} in Ge was related to the biaxial strain, and values for strain and stress were calculated from previously measured components of the Raman-strain tensor. Strain and stress were studied as a function of annealing temperature, ion dose and grain size for Ge films deposited under different conditions. The strain energy of the Ge thin film was calculated and compared to the surface energy and grain boundary energy of the film.

Thesis Supervisor: Dr. Henry I. Smith

Title: Professor of Electrical Engineering

Thesis Supervisor: Dr. Carl V. Thompson

Title: Professor of Materials Science and Engineering

Acknowledgments

First, I would like to thank my thesis advisors, Professor Henry I. Smith and Professor Carl V. Thompson, for their guidance and support throughout the entire work. Their expertise, enthusiasm, and guidance were invaluable, and are reflected in this thesis.

I am grateful to the members and technical staff of the Submicron Structures Laboratory for their expert assistance. Jim Carter, Mark Porter, and Darrell Roan kept the lab running smoothly and thereby made research possible. At Lincoln Laboratory, the efforts of Mark McAleese and John Woodhouse were indispensable to this thesis. They generously shared their time and experience to make possible the ion implantations which were done under novel (and extreme!) conditions. At GTE Laboratories, Dr. Ray Chen, Steve Brown and John Hryniewicz provided access to and assistance with Raman spectroscopy, and are to be heartily acknowledged. Dr. James F. Ziegler of IBM research provided an IBM PC version of TRIM, which was extremely helpful.

Helpful discussions with Walter Brown, Bob Cammarata, Rob Elliman, Jerry Floro, Nicole Herbots, Gillis Holmen, Hyoung-June Kim and Jan Linnros expanded my understanding of ion-solid interactions and kinetics, and are gratefully acknowledged.

Thanks go to my fellow students and friends who have been with me in really good times, really bad times and everything in between: Erik, Chee, Joyce, Eva, Jim, and Josie; Brewster, Amy, Karl, Andy, John, Karla, Regan, Ellen, Clea, Evie, Jeff, Alexandra, Tom and Ruth, Mark and Susan.

For Teresa

.

Contents

List of Figures

10

List of Tables

Chapter 1

Introduction

Ion-solid interactions have been the subject of intensive research in recent years, principally because ion beams are demonstrably useful for enhancing the kinetics of solid phase processes, or making possible kinetic paths that are not accessible by thermal processing alone. Previous research has included investigations of sputtering, ion implantation, ion beam mixing, ion beam enhanced diffusion, ion beam induced epitaxy, and ion beam deposition. From a technological point of view, ion beam processing is attractive because it can be used to enhance surface or thin film kinetics. This typically permits processing to be performed at temperatures much lower than those employed in conventional thermal processes.

Grain growth has been studied for many years, both in bulk and thin film materials. Early grain growth research concentrated on bulk metallic materials. Recently, grain growth has acquired new interest and importance

in the form of thin film studies, whose primary application has been in integrated circuit development. The study of the kinetics of grain growth is important to device performance, and circuit and system reliability. As circuits diminish in size and grow in complexity, it becomes ever more desirable to produce thin films with controlled microstructures.

Recently, grain growth has also been pursued as a potential process for producing device-quality semiconductor-on-insulator thin films. The constraints of Very Large Scale Integration (VLSI) limit the range of promising semiconductor-on-insulator technologies to those which are solid phase processes. These processes include porous oxidation of silicon (FIPOS), high dose oxygen implantation (SIMOX), epitaxial lateral overgrowth (ELO), and epitaxial growth on crystalline insulators. Grain growth is attractive because it is a solid phase process which does not require a crystalline substrate or underlying crystal. Moreover, when the film is sufficiently thin, surface energy anisotropy can be a significant driving force for grain growth. Hence surface-energy-driven secondary grain growth (SEDSGG) can lead to the development of uniform texture in the thin film. If the amorphous substrate is made artificially anisotropic with patterned surface relief structures, it should be also possible to achieve a well-controlled in-plane crystallographic orientation by surface energy minimization.

This thesis comprises the first systematic study which combines the study of ion-solid interactions and grain growth. A research program has been established to study ion beam enhanced grain growth (IBEGG). Ion beam enhanced grain growth has been studied experimentally in Ge, Au and Si films. IBEGG has been characterized by varying the ion dose, ion

energy, ion flux, ion species, temperature, and thin film deposition conditions. The effect of these parameters on grain size and microstructure has been analyzed both qualitatively and quantitatively using transmission electron microscopy (TEM).

A transition state model has been developed to describe the motion of grain boundaries during ion bombardment. The model has three criteria, which are based on experimental observations and simple assumptions: first, only elastic collisions at or very near grain boundaries contribute to enhanced grain growth; second, heating of the film by inelastic collisions has a negligible effect on grain growth; and third, ion bombardment does not influence the driving force for grain boundary migration. The model accounts for the dependence of IBEGG on the experimental parameters cited above. An atomistic picture of the jump rate at grain boundaries during IBEGG is presented. Monte-Carlo simulation of ion range and defect production was performed using the TRIM code and a modified Kinchin Pease formula. The calculated defect yield per incident ion was correlated with enhanced grain growth, and used to estimate the number of atomic jumps at the grain boundary per defect generated at the boundary for a given driving force. The IBEGG and thermal growth rates are related to their respective point defect populations.

Interest in the problem of ion beam enhanced grain growth is growing. During the course of this thesis research, IBEGG has been reported for Ge[1,2], Au, Si [1], Ni-Ag[4], and Ni films[5].

Also described is a study of the correlation of strain and microstructure during ion beam enhanced grain growth and thermal annealing of polycrys-

talline Ge films. Raman spectroscopy was employed as a probe of biaxial strain in the thin Ge films. The first-order Stokes Raman peak at 304 cm^{-1} in Ge was related to the biaxial strain, and values for strain and stress were calculated from previously measured components of the Raman-strain tensor. Strain and stress were studied as a function of annealing temperature, ion dose and grain size for Ge films deposited under different conditions. The strain energy of the Ge thin film was calculated and compared to the surface energy and grain boundary energy of the film.

The thesis is organized as follows:

Chapter 1 provides an overview of the thesis and introduces general concepts of grain growth and ion beam enhanced grain growth. Chapter 2 reviews the basic understanding of ion-solid interactions, including elastic collision kinematics, inelastic energy loss, ion range calculations models for defect production, high density cascades, and simulation of ion-solid interactions. Chapter 3 describes the research and theoretical development of ion beam enhanced grain growth. Chapter 4 describes the correlated strain and microstructural studies of thin Ge films. Chapter 5 summarizes the IBEGG experiments and modeling. The characteristics of other ion beam enhanced kinetic processes are briefly described and compared to ion beam enhanced grain growth. The work on strain and microstructure is summarized, and directions for future work are outlined.

1.1 Grain Growth

Important to the discussion of IBEGG is a general understanding of the concepts central to film deposition, normal grain growth and secondary grain growth. In this work, two modes of film deposition are referred to. The first, denoted as-deposited polycrystalline, is depicted in Fig. 1.1a). In this mode, crystalline domains nucleate and grow during film deposition as shown at the top. These domains grow until they impinge on each other and begin to coalesce. The film grows by filling voids in the coalescing film until a continuous film is formed. The film develops into a somewhat columnar microstructure[1]. Typically, the continuous film has distinct grooves which occur where grain boundaries intersect the surface of the film. As grain growth proceeds, the film becomes progressively more columnar as the grain size increases.

The second mode of deposition, denoted as-deposited amorphous, is depicted in Fig. 1.1b). The film is deposited at a low temperature so that it is amorphous during deposition. Subsequent to deposition, the film is heated. Nucleation and growth of crystalline phases occurs in such a way that the completely crystallized film consists of small polyhedral, non-columnar grains which do not span the film thickness. After crystallization the film typically remains very smooth. During subsequent grain growth, the film grows to a columnar structure, and can develop grain boundary

---

[1] A columnar microstructure is one characterized by grains which span the film thickness with boundaries that are normal to the plane of the film and have no curvature normal to the plane of the film.
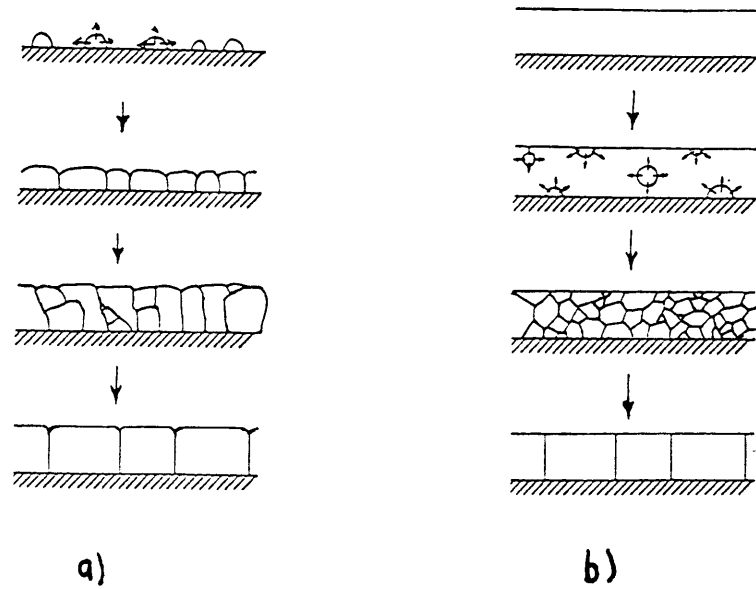
Figure 1.1: Evolution of microstructure in a) as-deposited polycrystalline and b) as-deposited amorphous films.

grooves.

It is also important to develop definitions for normal grain growth and secondary grain growth. Normal grain growth, which can occur in either two or three dimensions, refers to a mode of growth for which the driving force is the reduction of grain boundary energy. Normal grain growth, which is depicted in two dimensions in Fig. 1.2a), is characterized by a monomodal grain size distribution whose average size increases with time. Normal grain size distributions are found to be approximately lognormal experimentally[6], but other forms for the distribution are predicted by existing theories[7,8]. It has been found experimentally that normal grain growth slows down much more rapidly than is predicted by the aforementioned theories[7,8] when the grain size is comparable to the film thickness.

An explanation for the stagnation of normal grain growth has been offered in terms of the drag on grain boundaries exerted by impurities. However, stagnation of normal grain growth also occurs in very pure materials, so that another explanation is required. It is possible that grain boundary grooving [9] could be responsible for the slowing of normal grain growth in pure materials.

Secondary grain growth in thin films, which is depicted schematically in Fig. 1.2b), begins after the development of a columnar normal grain structure. It is characterized by the appearance of large abnormal grains within a matrix of small normal grains. This implies that the grain size distribution is bimodal during secondary grain growth, with one peak corresponding to the normal grain population, and another corresponding to the emerging secondary grain population. After secondary grain growth is completed, the distribution once more becomes monomodal, but with an average grain size much greater than the film thickness. Secondary grain growth has been observed experimentally in alloys[10,11,12] as well as thin Si, Ge and Au films[14,15,13,16]. Recently a model for secondary grain growth has been given which proposed that the principal driving force for secondary grain growth is the difference in surface energy between adjacent grains[17]. Arguments have been given to support the assertion that grain boundary energy cannot alone result in secondary grain growth, and that an additional driving such as surface energy is required[18].
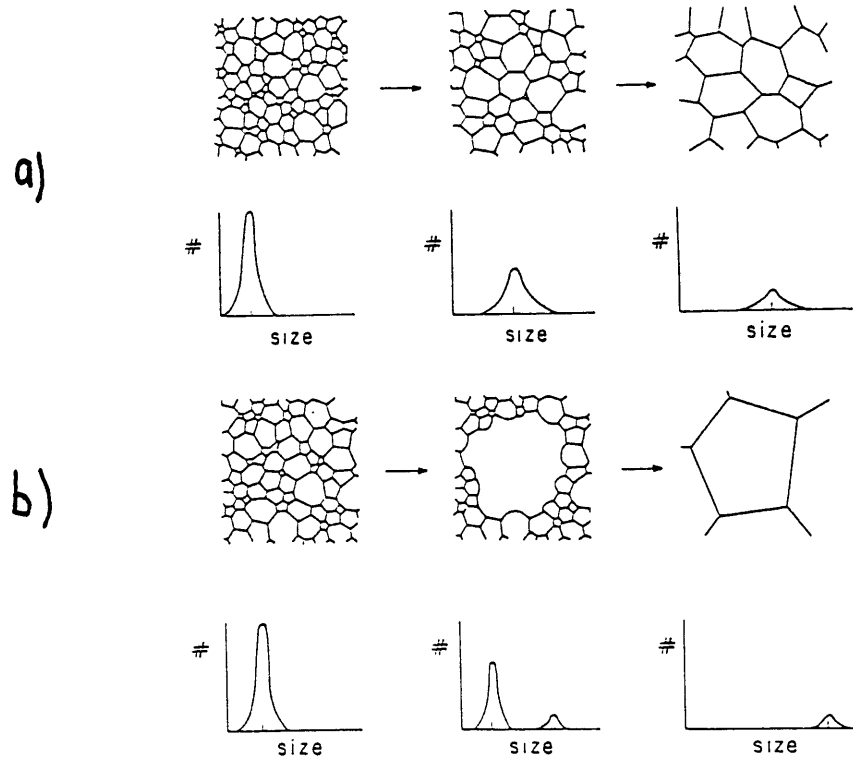
Figure 1.2: Grain topologies and grain size distributions for a) normal grain growth and b) secondary growth growth.
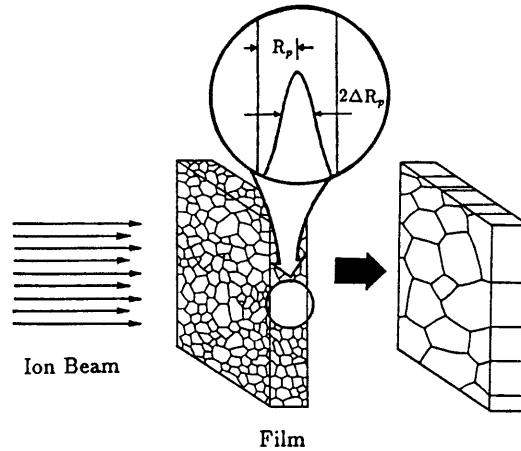
Figure 1.3: Schematic of the IBEGG process showing the development of a columnar grain structure.

1.2 IBEGG

The research on ion beam enhanced grain growth described here focused on grain growth up to and slightly beyond a columnar grain structure. The ion energy varied from 40 - 200 keV, and was chosen so that the peak of the ion damage profile was approximately in the center of the film, as depicted in Fig. 1.3. The thin films were either unsupported (to facilitate TEM observation) or deposited on thermally-grown SiO_2 substrates. The film thickness was chosen to be comparable to the standard deviation of the ion damage profile. Coincidentally, this film thickness regime is the one in which secondary grain growth has been observed in all three materials. For the work on Ge and Si films, the substrate temperature was sufficiently high to dynamically anneal ion damage as IBEGG proceeded. In Au films,

the substrate was held at room temperature in order to prevent thermal grain growth from competing with IBEGG. It is possible that the incident ion beam was at least partially channeled in certain, well-oriented grains. However, channeling does not seem to have played a role in selectively promoting grain growth, since no preferred texture was seen in the films as a result of IBEGG.

Because of the projected ion ranges and doses employed in the IBEGG research described here, a distinction can be drawn between IBEGG and other related ion beam techniques such as ion beam deposition[20,21] and simultaneous ion bombardment and film deposition[22]. The basic strategy of IBEGG can be thought of as the enhancement of the kinetics within the film rather than at the surface. Choosing the projected range to be in the center of the film results in an increased ion damage to sputtering ratio, with respect to lower energy beams.

Chapter 2

Fundamentals of Ion-Solid Interactions

2.1 Introduction

In this chapter, we will examine the physical interactions which occur when an energetic ion incident upon a solid target slows down and comes to rest in the solid. In the process of stopping, the ion loses energy *elastically* in collisions with atoms in the target. Energy is also lost *inelastically* by the ion in the form of electron-electron interactions and electron-nucleii interactions. In general, these energy loss processes should be coupled, however the coupling appears to be quite weak. Hence in virtually all models of ion-solid interactions, the elastic and inelastic energy losses are

27

considered to be independent, and are modeled separately.

In a collision, elastic energy is transferred from the moving ion to the initially stationary target atoms. The energy imparted to the struck target atoms can be sufficient to cause them to be displaced from their lattice positions and recoil implanted into the solid. The form of the elastic energy transfer will determine the details of the trajectories of the incident ion and displaced target atoms. A brief review of elastic collision theory is given here and details have been developed elsewhere [23,24,25].

An elastic collision also has the effect of creating points defects in the solid in excess of their equilibrium concentrations. These defects may be usefully thought of as the medium by which the kinetic energy of the incident ion is converted to a potential energy of the solid. Hence the energy of the crystalline solid is raised above the energy of a crystal in thermal equilibrium at the same temperature. These ion beam-generated point defects are critical to the process of ion beam enhanced grain growth.

Inelastic energy loss occurs when the electronic charge distributions surrounding the interacting nucleii begin to overlap. Ionization and excitation of electrons can occur. In the subsequent decay process, photon emission and electron emission are possible. In general, the emitted photon or electron does not contribute to the kinetic energy of the moving ions and recoils, or to the potential energy of the crystal, so they are the source of the inelastic energy loss.

After the ion has lost almost all of its initial energy so that its remaining kinetic energy is insufficient to displace another target atom, the ion imparts its remaining energy to the lattice as phonons and comes to rest

in a substitutional or interstitial lattice site. This represents another form of inelastic energy loss.

The ion-solid interaction can also be either individual or collective. That is, we may treat the interaction as a series of binary collisions between individual ions and target atoms or as a many-particle interaction, as in the case of a very high density collision cascade. The major portion of this chapter focuses on the former treatment, which we will call the *binary collision approximation*. This assumption underlies almost all the models for ion-solid interactions discussed here. Much less is known about high density cascades, and modeling their effects requires a many-body approach. However, we will briefly remark on some of the observations [26,27,28] which have been made about high density cascades.

In the discussion that follows, we will assume that the solid target is crystalline, but that ion channeling by the crystalline lattice can be ignored. Accounts of ion channeling effects can be found elsewhere [24,25]. This is an assumption that is appropriate during ion beam-enhanced grain growth, since channeling is likely to be attenuated during the development of a columnar structure in IBEGG.

2.2 Elastic Collisions

The various models for elastic collisions are all classical mechanical treatments of two-body scattering in a central force potential. Therefore, it is reasonable to ask whether classical mechanics provides a valid description

of the interaction [29]. For an incident ion with energy E_o, which has a wavelength

$$\lambda = \hbar [\frac{2\pi}{M_1 E_o}]^{\frac{1}{2}} \qquad (2.1)$$

there are two criteria to consider:

- Is the particle wavelength λ much smaller than the distance, a, over which atomic forces act?

$$\lambda \ll a = \frac{a_B}{(Z_1 Z_2)^{\frac{1}{6}}} \qquad (2.2)$$

so we must require

$$E_o \gg \frac{2\hbar^2}{M_1 a^2} \qquad (2.3)$$

- Is the scattering angle much larger than the diffraction angle?

$$\phi \gg \frac{\lambda}{a} \qquad (2.4)$$

Thus

$$\phi^2 E_o \gg \frac{2\hbar^2}{M_1 a^2} \qquad (2.5)$$

For heavy ions such as Ge^+ or Si^+, these conditions are satisfied for $E_o > 10$ eV, so the use of classical mechanics seems justified here. It is noteworthy that the displacement energy E_d in a semiconductor is approximately 15 - 20 eV. Hence atomic displacements, which are crucial to ion beam enhanced grain growth can be modeled using classical mechanics.

2.2.1 Coulomb Interactions

A useful simplification of the complex collision process is to consider the repulsive interaction to be governed by a Coulomb potential, and to assume

that the electronic charge distributions act only to screen the Coulombic repulsion. The attractive Coulomb interaction is ignored here, which is a reasonable assumption for energies above $\approx$ 10-20 eV. (The attractive Coulomb potential is important, however, in determining the atomic displacement energy). Hence

$$V(r) = \frac{Z_{1eff} Z_{2eff} e^2}{4\pi \epsilon_o r} \qquad (2.6)$$

where Z_{1eff} and Z_{2eff} are the effective charge on the ion and target atom respectively, and r is the radius of interaction.

2.2.2 Hard Sphere Approximation

An even simpler assumption is the interaction potential

$$V(r) = V_o \qquad\qquad r \leq r_o \qquad (2.7)$$

$$V(r) = 0 \qquad\qquad r \geq r_o \qquad (2.8)$$

where r_o is the atomic radius. This potential results from the *hard sphere approximation*. The hard sphere approximation seems justifiable when the interaction distances are considered: the greatest value that r can have is approximately half a lattice constant (1 - 3 Å) and its smallest value is approximately 0.1 Å. Furthermore, since hard sphere scattering is simply a geometric problem, it is easy to solve analytically. Thus it is mainly a heuristic model, useful for building an intuition about the general nature of ion-solid interactions.
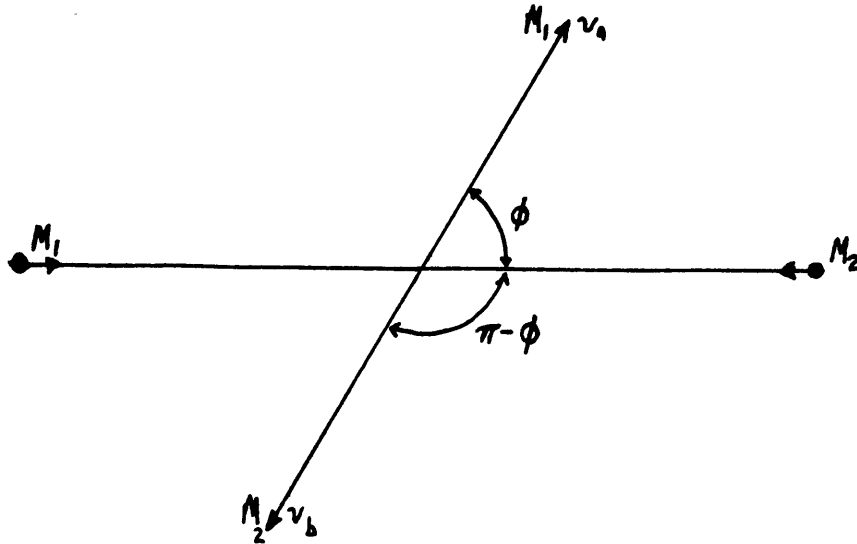
Figure 2.1: Schematic diagram of scattering of hard spheres in the center of mass frame of reference.

The strategy here, as in most scattering calculations, is to find the scattering angle, and the energy transferred from the incident ion to the struck atom. From these quantities, the differential scattering cross section and the nuclear stopping power can be found, as will be shown later.

It is most convenient to solve the ion-atom collision problem in the center of mass coordinate system. Figure 2.1 depicts the collision schematically in the center of mass system. Following the notation of Ref. [24], The center of mass travels along a path parallel to the incident ion at a distance of $p(M_2/M_1 + M_2)$ from the incident ion path, where M_1 and M_2 are the incident ion and target atom masses, respectively and p is the impact

parameter[1]. The center of mass momentum and energy are

$$p_{cm} = (M_1 + M_2)v_{cm} \qquad (2.9)$$

$$E_{cm} = \frac{(M_1 + M_2)v_{cm}^2}{2} \qquad (2.10)$$

where v_{cm} is the center of mass velocity. In terms of the incident ion velocity, v_o,

$$v_{cm} = \frac{M_1 v_o}{M_1 + M_2} \qquad (2.11)$$

The ion velocity relative to the center of mass, v_a, is

$$v_a = \frac{M_2 v_o}{M_1 + M_2} \qquad (2.12)$$

The target atom velocity relative to the center of mass, v_b, is

$$v_b = -\frac{M_1 v_o}{M_1 + M_2} \qquad (2.13)$$

In order to preserve the center of mass motion, the velocities v_a and v_b have the same magnitudes before and after the collision. If the ion is scattered through an angle of ϕ in the center of mass frame, then the target atom is scattered through an angle $\pi - \phi$. After vector addition in the center of mass frame and transformation back to the laboratory frame, we obtain the final ion velocity, v_1, and atom velocity v_2. In the laboratory frame, the ion is scattered through an angle θ and the atom is scattered through ψ.

$$\frac{v_1^2}{v_o^2} = \left(\frac{M_2 \sin\phi}{M_1 + M_2}\right)^2 + \left(\frac{M_1 + M_2 \cos\phi}{M_1 + M_2}\right)^2 \qquad (2.14)$$

---

[1]The impact parameter is shown in Fig. 2.2.

$$\frac{v_1^2}{v_o^2} = [1 - \frac{4M_1M_2}{(M_1 + M_2)^2} \sin^2(\frac{\phi}{2})]$$ (2.15)

The energy retained by the ion is

$$E_1 = [1 - \frac{4M_1M_2}{(M_1 + M_2)^2} \sin^2(\frac{\phi}{2})]E_o$$ (2.16)

where E_o is the incident ion energy. The energy transferred to the struck target atom is

$$E_2 = E_o[\frac{4M_1M_2}{(M_1 + M_2)^2} \sin^2(\frac{\phi}{2})]$$ (2.17)

Note that when $\phi = 0$, the energy transfer is at a minimum(i.e., $E_2 = 0$) This corresponds to the situation in which the incident ion just misses the target atom. By contrast, when $\phi = \pi$ the energy transfer is at its maximum. This corresponds to a head-on collision. The maximum transferred energy E_m is

$$E_m = E_o[\frac{4M_1M_2}{(M_1 + M_2)^2}]$$ (2.18)

Hence, if we vary ϕ in the range $0 < \phi < \pi$,

$$0 < E_2 < E_o[\frac{4M_1M_2}{(M_1 + M_2)^2}]$$ (2.19)

An interesting result occurs if $\phi = \pi$ and if $M_1 = M_2$. Then $E_m = E_o$. This implies that the incident particle comes to rest after transferring all of its energy to the struck atom, the condition for a *replacement collision*.

Now we want to obtain the energies and angles in the laboratory frame coordinates. Figure 2.2 is a diagram of the collision in the laboratory frame. Both particles are assumed to have a radius r_o. The distance perpendicular to the ion velocity between the centers of mass of the particles is called the *impact parameter*. The incident ion is scattered by an angle θ and the
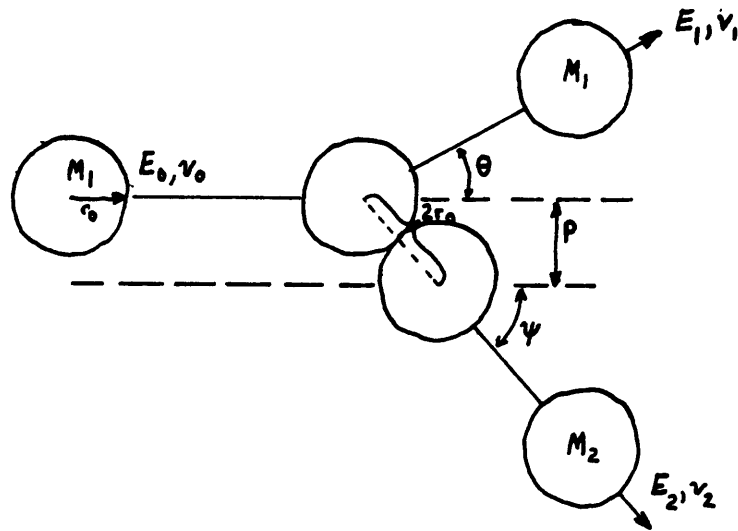
Figure 2.2: Schematic diagram of hard sphere scattering in the laboratory frame.

target atom is scattered by an angle ψ. From the geometry of the problem it is clear that

$$\sin \psi = \frac{p}{2r_o} \tag{2.20}$$

Referring again to Fig. 2.1, note

$$v_1 \sin \theta = v_a \sin \phi \tag{2.21}$$

and

$$v_1 \cos \theta = v_{cm} + v_a \cos \phi \tag{2.22}$$

Hence

$$\tan \theta = \frac{\frac{M_2 \sin \phi}{M_1 + M_2}}{\frac{M_1 + M_2 \cos \phi}{M_1 + M_2}} \tag{2.23}$$

If we substitute $A = M_2/M_1$, then this is simply

$$\tan \theta = \frac{A \sin \phi}{1 + A \cos \phi} \tag{2.24}$$

When $A < 1$, the heavier incident ion is always forward scattered; that is, $0 \leq \theta \leq \pi/2$. When $A > 1$, the ion can be scattered through $0 \leq \theta \leq \pi$. Note that this implies that a lighter ion can be *backscattered*. (This is why Rutherford backscattering analysis is done with He^+ rather than, say, Xe^+ ions).

Using the same arguments, and referring to Fig. 2.1, it can be seen that the scattering angle of the target atom in the laboratory frame, ψ, is given by

$$\tan \psi = \frac{M_1 v_o \sin(\pi - \phi)}{\frac{M_1 v_o}{M_1 + M_2} + \frac{M_1 v_o}{M_1 + M_2} \cos(\pi - \phi)} \tag{2.25}$$

Thus

$$\tan \psi = \tan\left(\frac{\pi - \phi}{2}\right) \tag{2.26}$$
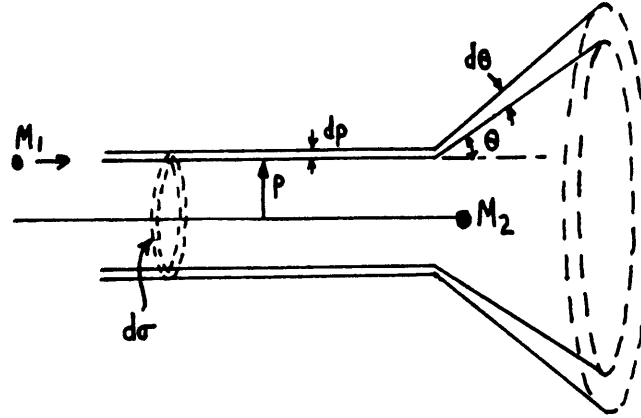
Figure 2.3: The differential scattering cross section.

or

$$\psi = \frac{\pi}{2} - \frac{\phi}{2} \tag{2.27}$$

We already found that $0 \leq \phi \leq \pi$, so this implies that $0 \leq \psi \leq \pi/2$. This is the intuitively obvious but important result that target atoms can only be forward scattered.

If there is, instead of one ion, a flux of many ions impinging on the target atom, only those with impact parameters $p \leq 2r_o$ are scattered. Thus the total scattering cross section, σ, is

$$\sigma = \pi p^2 = 4\pi r_o^2 \tag{2.28}$$

Now we can compute the *differential scattering cross section* in terms of

the transferred energy, E_2. For a flux of ions, those which will be scattered between θ and $\theta + d\theta$ have a cross section

$$d\sigma = 2\pi p\,dp \tag{2.29}$$

as shown in Fig. 2.3. Since

$$\psi = \frac{\pi}{2} - \frac{\phi}{2} \tag{2.30}$$

and

$$\sin\psi = \frac{p}{2r_o} \tag{2.31}$$

then

$$\cos\left(\frac{\phi}{2}\right) = \frac{p}{2r_o} \tag{2.32}$$

Combining this with

$$E_2 = E_o\left[\frac{4M_1M_2}{(M_1 + M_2)^2}\sin^2\left(\frac{\phi}{2}\right)\right] \tag{2.33}$$

yields the impact parameter in terms of the transferred energy.

$$p^2 = 4r_o^2\left(1 - \frac{E_2}{E_m}\right) \tag{2.34}$$

Differentiating gives the differential cross section in terms of the transferred energy.

$$2\pi p\,dp = \frac{4\pi r_o^2}{E_m}dE_2 \tag{2.35}$$

This shows that the differential cross section for energy transfer by hard sphere collisions is *independent of the transferred energy*. It depends only on the maximum transfer E_m and the hard sphere radius r_o. Also implied is the fact that the differential cross section is independent of center of mass scattering angle. All values of energy transfer $0 \leq E_2 \leq E_m$ and scattering angle $0 \leq \phi \leq \pi$ are equally likely, so the scattering is isotropic.

2.2.3   Realistic Interatomic Potentials

The hard sphere potential, while readily solved and analyzed is obviously a drastic simplification of the actual potential of a nuclear charge screened by the electronic charge distribution. In this section, we will review those potentials which yield better descriptions of the scattering process. Different potentials are appropriate models for collisions between atoms with different values of nuclear charge and mass. Only a few give analytically tractable scattering angle results. However, the others are useful since we can extract scattering angles and differential cross sections by solving the scattering integral numerically as well as analytically, as we will see shortly. Recently, an attempt has been made to develop a universal potential which works for all nuclear charges, Z_1 and Z_2 [30].

For interaction distances less than the Bohr radius, a_B, an unscreened Coulomb potential is a good approximation to the potential between the nucleii, since there are no electronic orbitals with radii smaller than this distance. Hence

$$V(r) = \frac{Z_1 Z_2 e^2}{4\pi \epsilon_o r} \qquad\qquad 0 \le r \le a_B \qquad\qquad (2.36)$$

For $r > a_B$, electrons screen the repulsive nuclear interaction. Except for the Born-Mayer potential, all the potentials can be represented as the product of an unscreened Coulomb potential and a screening function $\Phi(r)$

$$V(r) = \frac{Z_1 Z_2 e^2}{4\pi \epsilon_o r}\Phi(r) \qquad\qquad r > a_B \qquad\qquad (2.37)$$

The potentials are:

Born-Mayer Potential

Each atom has a closed shell structure which partially screens the repulsive Coulombic forces [31].

$$V(r) = A \exp(\frac{-r}{a}) \qquad\qquad a, A \; constant \qquad (2.38)$$

Bohr Potential

Bohr, Firsov and Abrahamson [29,32,33] suggested the use of a screened potential, based on a Thomas-Fermi model of screening, of the form

$$V(r) = \frac{Z_1 Z_2 e^2}{4\pi\epsilon_o r} \exp(\frac{-r}{a_s}) \qquad (2.39)$$

where a_s, the Thomas-Fermi screening length is

$a_s = 0.8843 a_B (Z_1^{\frac{1}{2}} + Z_2^{\frac{1}{2}})^{-\frac{2}{3}}$.

Linhard Potential

Linhard [34] and others [35] have proposed an inverse power potential of the form

$$V(r) = \frac{C}{r^s} \qquad\qquad C = \frac{Z_1 Z_2 e^2 a_s^{s-1}}{4\pi\epsilon_o s} \qquad (2.40)$$

where s is an exponent in the range from 1-4.

Thomas-Fermi Potential

The form of this potential was originally proposed by Sommerfeld [36].

$$V(r) = \frac{Z_1 Z_2 e^2}{4\pi\epsilon_o r}[1 + (\frac{r}{ka_s})^\lambda]^{-\frac{3}{\lambda}} \qquad (2.41)$$

where $\lambda = .8034$ and $k = 12^{2/3}$.

Molière Potential

Another screened potential was proposed by Molière [37].

$$V(r) = \frac{Z_1 Z_2 e^2}{4\pi\epsilon_o r}\Phi(r) \tag{2.42}$$

where

$$\Phi(r) = 0.35\exp-(\frac{0.3r}{a_s}) + 5.5\exp-(\frac{1.2r}{a_s})$$
$$+0.1\exp-(\frac{6r}{a_s}) \tag{2.43}$$

Lenz-Jensen Potential

The Lenz-Jensen potential [38,39] has the same
functional form as the Molière potential given above. The screening function is

$$\Phi(r) = 0.7466\exp-(\frac{1.038r}{a_s}) + 0.2433\exp-(\frac{0.3876r}{a_s})$$
$$+0.01018\exp-(\frac{0.206r}{a_s}) \tag{2.44}$$

Universal Potential

Recently, Ziegler, Biersack and Littmark [30] have made accurate calculations of the screening functions for various values of Z_1 and Z_2. In the calculation, nuclear-nuclear repulsion, electronic-nuclear attraction, electron-electron interaction, Pauli excitation and exchange interactions were taken into account. In general, these yield different screening functions for different atom-ion combinations. A best fit was made to these various screening
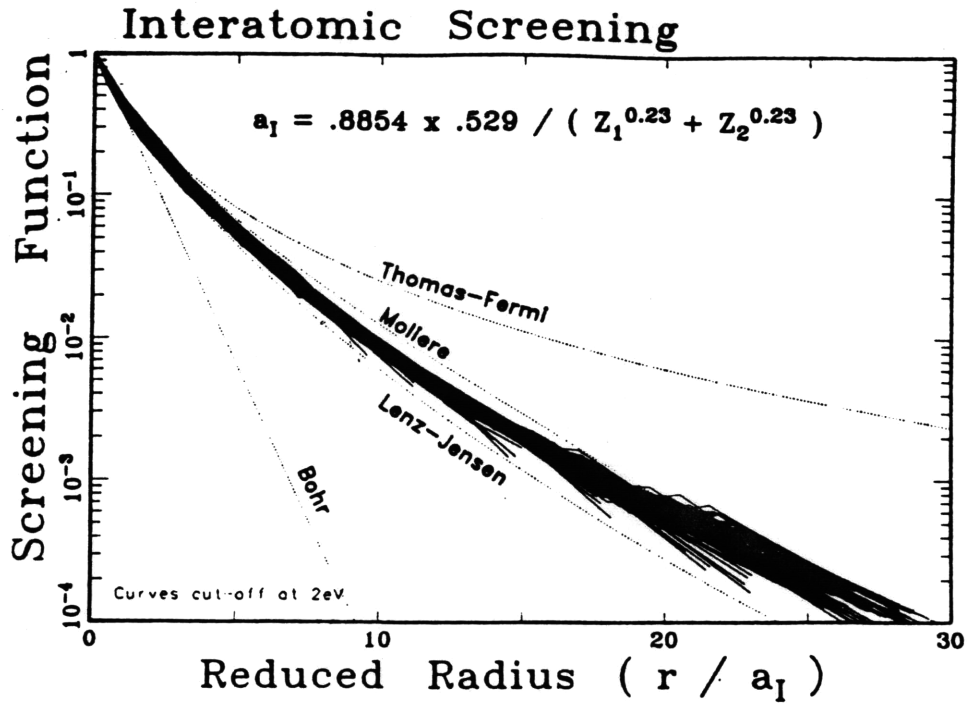
Figure 2.4: Comparison of various screening functions. The solid lines are simulation data which were used to generate a fit to the universal potential.

functions, yielding a universal screening function:

$$\Phi(r) = 0.1818 \exp -(\frac{3.2r}{a_I}) + 0.5099 \exp -(\frac{0.9423r}{a_I})$$

$$+0.2802 \exp -(\frac{0.4028r}{a_I}) + 0.02817 \exp -(\frac{0.2016r}{a_I}) \qquad (2.45)$$

where $a_I = 0.8854 a_B/(Z_1^{0.23} + Z_2^{0.23})$. A comparison of the various screening lengths is shown in Fig. 2.4 (after Ziegler, et.al. [30]).

In general the Born-Mayer potential is valid for heavy ions and atoms at low energies, in the range of 0.1 to 1000 eV. For implantation energies, between 1-100 keV, the various screened Coulomb potentials are useful(Bohr, Thomas-Fermi, Molière, Lenz-Jensen and Universal). Also useful in this regime is the inverse power (Linhard) potential if one uses $s \approx 2$. For

light ions at high energies, beyond 1 MeV(the Rutherford backscattering regime), an unscreened Coulomb potential is generally valid.

2.2.4 Collision Mechanics for a General Potential

In order to make use of the screened potentials outlined above, we now develop a classical solution to the two body collision for an arbitrary potential. Consider a two particle interaction in the center of mass frame, as shown in Fig. 2.5. The scattering angle is ϕ, and the impact parameter is p. The instantaneous distances of particles 1 and 2 from the center of mass are r_1 and r_2, respectively. The distance of closest approach is given by R_m, where $R_m = 2r_o$. The angle between the perpendicular bisector of R_m and r_1 is given by α.

The relative energy of collision is the relative kinetic energy of the two particles before collision, when $V(r) = 0$.

$$E_r = \frac{1}{2}M_1 v_a^2 + \frac{1}{2}M_2 v_b^2 \qquad (2.46)$$

$$E_r = \frac{1}{2}[M_1(\frac{M_2}{M_1 + M_2})^2 v_o^2 + M_2(\frac{-M_1}{M_1 + M_2})^2 v_o^2] \qquad (2.47)$$

so that

$$E_r = \frac{1}{2}(\frac{M_1 M_2}{M_1 + M_2})v_o^2 = \frac{M_2}{M_1 + M_2}E_o \qquad (2.48)$$

By energy conservation the total energy during the collision is equal to the relative energy, E_r

$$\frac{M_2 E_o}{M_1 + M_2} = V(r_1 + r_2) + \frac{1}{2}M_1(\dot{r}_1^2 + r_1^2\dot{\alpha}^2) + \frac{1}{2}M_2(\dot{r}_2^2 + r_2^2\dot{\alpha}^2) \qquad (2.49)$$
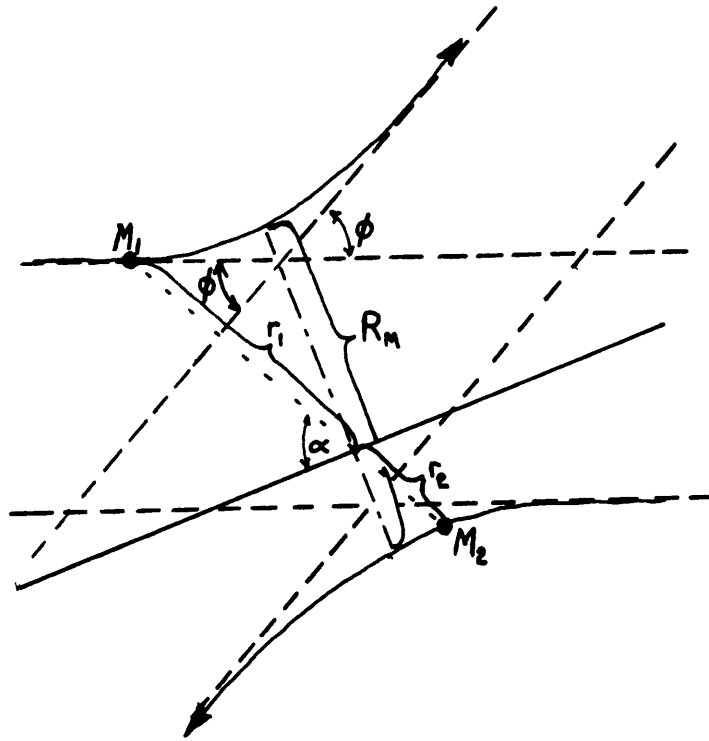
Figure 2.5: Schematic diagram of two body scattering in the center of mass frame for a general potential $V(r)$.

where the dotted quantities denote time derivatives. Now substituting

$$r_1 = \left(\frac{M_2}{M_1 + M_2}\right)r \tag{2.50}$$

and

$$r_2 = \left(\frac{M_1}{M_1 + M_2}\right)r \tag{2.51}$$

we obtain

$$\frac{M_2 E_o}{M_1 + M_2} = V(r) + \frac{1}{2}\left(\frac{M_1 M_2}{M_1 + M_2}\right)(\dot{r}^2 + r^2\dot{\alpha}^2) \tag{2.52}$$

Similarly, angular momentum conservation allows the equation of the initial and instantaneous values of the angular momentum.

$$\frac{M_1 M_2 v_o p}{M_1 + M_2} = M_1 r_1^2 \dot{\alpha} + M_2 r_2^2 \dot{\alpha} \tag{2.53}$$

Hence

$$\dot{\alpha} = \frac{p v_o}{r^2} \tag{2.54}$$

By chain rule differentiation

$$\dot{r} = \frac{dr}{d\alpha}\frac{d\alpha}{dt} = \dot{\alpha}\frac{dr}{d\alpha} \tag{2.55}$$

Let $u = 1/r$, and substituting the momentum equation into the energy equation to obtain

$$\frac{du}{d\alpha} = \{\frac{1}{p^2}[1 - \frac{V(u)(M_1 + M_2)}{E_o M_2}] - u^2\}^{\frac{1}{2}}\frac{du}{d\alpha} = \{\frac{1}{p^2}[1 - \frac{V(u)}{E_r}] - u^2\}^{\frac{1}{2}} \tag{2.56}$$

The total scattering angle is ϕ. Therefore in coming from $r = \infty$ to $r = r_m$, half of the total scattering angle is experienced. This angle is

$$\int_{\frac{\phi}{2}}^{\alpha} d\alpha = \int_0^u \frac{p\,du}{[1 - \frac{V(u)}{E_r} - (pu)^2]^{\frac{1}{2}}} \tag{2.57}$$

$$\int_{\frac{\phi}{2}}^{\alpha} d\alpha = -\int_{-\infty}^{r} \frac{p\,dr}{r^2[1 - \frac{V(r)}{E_r} - \frac{p^2}{r^2}]^{\frac{1}{2}}} \tag{2.58}$$

At minimum separation, r_m, $\alpha = \frac{\pi}{2}$ so

$$\int_{\frac{\phi}{2}}^{\frac{\pi}{2}} d\alpha = \frac{\pi}{2} - \frac{\phi}{2} = -\int_{-\infty}^{r_m} \frac{p\,dr}{r^2[1 - \frac{V(r)}{E_r} - \frac{p^2}{r^2}]^{\frac{1}{2}}} \tag{2.59}$$

Hence ϕ is

$$\phi = \pi - 2p \int_{-\infty}^{r_m} \frac{dr}{r^2[1 - \frac{V(r)}{E_r} - \frac{p^2}{r^2}]^{\frac{1}{2}}} \tag{2.60}$$

This is a very important result known as the *scattering integral*. Once the scattering angle is known, the transferred energy and the scattering angle in the laboratory frame can be found, as before with

$$E_2 = \frac{4M_1 M_2}{(M_1 + M_2)^2} \sin^2(\frac{\phi}{2}) \tag{2.61}$$

and

$$\tan \theta = \frac{A \sin \phi}{1 + A \cos \phi} \tag{2.62}$$

In general, the scattering integral cannot be be solved analytically. Some workers have constructed computer codes which solve the scattering integral for each ion-atom combination using various potentials [40,41]. An important simplification of the scattering problem has been developed by Biersack et.al. [42] , as will be discussed in the section on TRIM. However, there are a few potentials for which the scattering integral is tractable. The inverse power potentials for $s = 1$ or $s = 2$ are two such cases. For $s = 1$, the potential simply reduces to the Coulomb potential

$$\frac{Z_1 Z_2 e^2}{4\pi \epsilon_o r} \tag{2.63}$$

The differential scattering cross section is

$$d\sigma = (\frac{Z_1 Z_2 e^2}{E_o 4\pi \epsilon_o})^2 \frac{\pi (M_1 + M_2)^2 \cos(\frac{\phi}{2}) d\phi}{4M_2 \sin^3(\frac{\phi}{2})}$$

$$= \frac{\pi (Z_1 Z_2 e^2)^2 dE_2}{16\pi^2 \epsilon_o^2 A E_o E_2^2} \qquad (2.64)$$

For $s = 2$,

$$V(r) = \frac{Z_1 Z_2 e^2 a_s}{8\pi \epsilon_o r^2}$$

$$= \frac{C}{r^2} \qquad (2.65)$$

The differential scattering cross section is

$$d\sigma = \frac{C(M_1 + M_2)^3 dE_2}{M_1 M_2^2 E_o^2 (1 - 4\gamma^2)^2 [x(1 - x)]^{\frac{1}{2}}} \qquad (2.66)$$

where

$$\cos \pi \gamma = x^{\frac{1}{2}}, \qquad x = \frac{(M_1 + M_2)^2 E_2}{4M_1 M_2 E_o} \qquad (2.67)$$

We can consider the hard sphere potential as an inverse power potential with

$$s = 0, \ r \le r_m$$

$$s = \infty, \ r > r_m \qquad (2.68)$$

For this potential

$$d\sigma = (M_1 + M_2)^2 \frac{\pi r_m^2 dE_2}{4M_1 M_2 E_o} \qquad (2.69)$$

This is equivalent to the differential scattering cross section derived earlier in terms of the scattering angle ϕ.

We can make a few qualitative comparisons between the hard sphere results and the Coulomb potential. Note that the total scattering cross section for the hard sphere potential is finite; $\sigma = \pi r_m^2$. For the Coulomb potential, however, the total scattering cross section is infinite. This implies that scattering occurs for all impact parameters. The angle of deflection, from the scattering integral, decreases as the impact parameter increases, an intuitively reasonable result.

2.3 Inelastic Collisions

When the electronic charge distributions on an incident ion and a target atom begin to overlap, electrons in the ground state of both distributions are excited. These excited electrons subsequently lose energy through photon, phonon or electron emission, rather than restoring kinetic or potential energy to the ions and recoils. Over the range of interest to ion beam enhanced grain growth, for heavy ions(i.e., ions other than H^+ or He^+) and energies between 50 and 200 keV, all the models for electronic energy loss yield a electronic stopping power linearly proportional to the ion velocity.

2.3.1 A Semiclassical Approach

The inelastic collision problem is fundamentally quantum mechanical in nature, however a semiclassical analysis allows us to estimate the regime in which inelastic scattering is important. The energy transfer, E_e from an

ion M_1 to an electron M_e for a head on collision in a hard sphere model is

$$E_e = \frac{4M_1 M_e}{(M_1 + M_e)^2} E_o \approx \frac{4M_e E_o}{M_1} \qquad since \ M_1 \gg M_e \qquad (2.70)$$

If the minimum energy for electron excitation is E_{ex}, then the excitation will only occur when

$$\frac{4M_e E_o}{M_1} > E_{ex} \qquad (2.71)$$

Since E_{ex} is of the order of several eV, and the ratio of masses of a nucleon to the electron is approximately 2000, electron excitation is important for

$$E_o \geq 1000 M_1 \qquad (eV) \qquad (2.72)$$

where M_1 is given in amu.

Another way of looking at the problem classically is to consider the ion to be a perturbation on the potential experienced by the electron. If the ion has mass M_1, velocity v_1 and energy E_1, then the duration of the perturbation is approximately

$$t \approx \frac{a_B}{v_1} \qquad (2.73)$$

Hence the frequency is

$$\omega \approx \frac{v_1}{a_B} \qquad (2.74)$$

If the energy of the ion is greater than the excitation energy E_{ex},

$$\hbar \omega \geq E_{ex} \qquad (2.75)$$

then ionization can occur. Since the ion energy is classically

$$E_1 = \frac{1}{2} M_1 v_1^2 \qquad (2.76)$$

the condition for excitation is

$$E_1 = \frac{M_1 E_{ex}^2 a_B}{2\hbar^2} \qquad (2.77)$$

2.3.2 The Firsov Model

In the Firsov approach [43], it is assumed that as the ion approaches the target atom, a quasi-molecule forms and electrons move back and forth across the quasi-boundary between the atoms. The electrons are assigned the momentum appropriate to atom to which they are attached. Thus electrons which move from the ion to the struck atom lose momentum and those that move from the atom to the ion gain momentum. The flux of electrons across the quasi-boundary is described by a kinetic gas model where the electron flux, J_e is

$$J_e = \frac{1}{4} n \langle v \rangle^2 \qquad (2.78)$$

where n is the electron density and $\langle v \rangle$ is the average electron density. The electron flux is integrated over the moving quasi-boundary to give

$$E_e = [\frac{4.3 \; x \; 10^{-8}(Z_1 + Z_2)^{\frac{5}{3}}}{[1 + 3.1 \; x \; 10^7(Z_1 + Z_2)^{\frac{1}{3}}p]^5}]v_o \qquad (eV) \qquad (2.79)$$

As noted above, the electronic energy transfer is proportional to the incident ion velocity, and hence is proportional to $E_o^{\frac{1}{2}}$.

2.3.3 The Linhard Model

The Linhard model [44] of electronic energy loss is a many-body treatment of the response of a free electron gas to a perturbation. The free electron

gas is assumed to be of constant density, and at zero temperature. All interactions are assumed to be nonrelativistic. For ion velocity v_o less than the Fermi velocity

$$E_2 = f(Z_1, \ Z_2, \ M_1, \ M_2, \ a_o)v_o \tag{2.80}$$

The other features of the Linhard electronic energy loss model are presented in the discussion of the LSS theory.

2.4 Ion Range Calculations

One of the quantities which is most commonly of interest in ion solid interactions is the range of incident ions in the solid target. Once we know the scattering angle and the energy transferred to the struck atom the range can be readily found. The energy loss rate with distance is proportional to the sum of the nuclear stopping power, $S_n(E)$, and the electronic stopping power, $S_e(E)$,

$$-\frac{dE}{dx} = N[S_n(E) + S_e(E)] \tag{2.81}$$

The total ion range is found by rearranging the relation above

$$N \int_0^R dx = -\int_{E_.,}^0 \frac{dE}{S_n(E) + S_e(E)} \tag{2.82}$$

$$R = \frac{1}{N} \int_0^{E_.,} \frac{dE}{S_n(E) + S_e(E)} \tag{2.83}$$

Now we need to evaluate $S_n(E)$ and $S_e(E)$. The nuclear stopping power is the integrated energy transferred from a moving ion to the target atoms.

$$S_n(E) = \int E_2 d\sigma \tag{2.84}$$

To evaluate this expression, the differential cross section $d\sigma$ is cast in terms of E_2 as follows. We recall that

$$E_2 = E_o \frac{4M_1 M_2}{(M_1 + M_2)^2} \sin^2 \frac{\phi}{2} = E_m \sin^2 \frac{\phi}{2} \qquad (2.85)$$

we can substitute for ϕ in the scattering integral

$$\phi = \pi - 2p \int_{-\infty}^{r_m} \frac{dr}{r^2 [1 - \frac{V(r)}{E_r} - \frac{p^2}{r^2}]^{\frac{1}{2}}} \qquad (2.86)$$

to yield an expression for p^2 in terms of E_2

$$p^2 = f(E_2, E_m) \qquad (2.87)$$

Differentiation of this and multiplication by π gives the differential scattering cross section

$$d\sigma = 2\pi p dp = \pi df(E_2, E_m) \qquad (2.88)$$

From an experimental point of view, the *projected range* is of greater interest than total range. The projected range, R_p, is the range of the ion projected into the target, perpendicular to the surface. By contrast the range, R, is the total path length of the particle in the target. Linhard, Scharff and Schiøtt [34] have computed the relationship between R and R_p. An approximate relationship useful for $M_2 > M_1$ is

$$\frac{R}{R_p} \approx (1 + \frac{M_2}{3M_1}) \qquad (2.89)$$

2.4.1 The LSS Theory

The theory of Linhard, Scharff and Schiøtt [34] (commonly referred to as LSS) is the most remarkable and most comprehensive analytic treatment of

stopping powers and ranges. The greatest success of the LSS theory is the formulation of a universal function for nuclear stopping by expressing the energy loss and range in the appropriate reduced coordinates. No single universal function for electronic stopping exists, but LSS were able to derive an analytic expression for electronic stopping. The assumed potential is the Thomas-Fermi potential

$$V(r) = \frac{Z_1 Z_2 e^2}{4\pi\epsilon_o r}[1 + (\frac{r}{ka_s})^\lambda]^{-\frac{3}{\lambda}} \qquad (2.90)$$

The Thomas-Fermi screening length assumed is

$$a_s = \frac{a_B}{(Z_1^{\frac{2}{3}} + Z_2^{\frac{2}{3}})^{\frac{1}{2}}} \qquad (2.91)$$

The LSS universal reduced nuclear stopping, $(d\epsilon/d\rho)_n$, is shown in Fig. 2.6, where

$$\epsilon = \frac{E a_s M_2}{Z_1 Z_2 e^2 (M_1 + M_2)} \qquad (2.92)$$

and

$$\rho = \frac{RN4\pi a_s^2 M_1 M_2}{(M_1 + M_2)^2} \qquad (2.93)$$

The reduced electronic stopping power is

$$(\frac{d\epsilon}{d\rho})_e = k\epsilon^{\frac{1}{2}} \qquad (2.94)$$

where

$$k = \frac{0.0793 Z_1^{\frac{2}{3}} Z_2^{\frac{1}{2}} (M_1 + M_2)^{\frac{3}{2}}}{(Z_1^{\frac{2}{3}} + Z_2^{\frac{2}{3}})^{\frac{3}{4}} M_1^{\frac{3}{2}} M_2^{\frac{1}{2}}} \qquad (2.95)$$

This relation gives a family of curves for various Z_1, Z_2, M_1, M_2. Two such electronic stopping curves are given in Fig. 2.6 above.
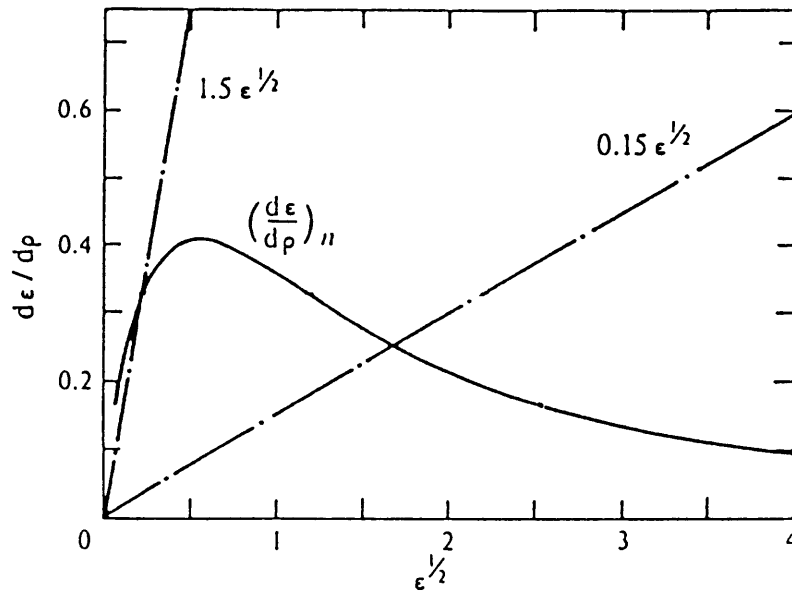
Figure 2.6: Electronic and nuclear stopping powers for LSS theory (After (ref LSS)).

As mentioned above, LSS also developed relations for the projected range. In addition the moments of the range distribution were calculated. The first moment of the range distribution, ΔR_p is called the *straggle* or standard deviation of the distribution. Various publications subsequent to the seminal 1963 paper of LSS developed the LSS theory results in forms that are more useful experimentally. A very useful reference for range distributions calculated using the LSS theory is that of Johnson and Gibbons [45]. They give ranges and higher moments of the range distributions for a variety of ions and solid targets. From these data, quite accurate approximations to the LSS range distributions can be generated.

2.5 Defect Production

2.5.1 Basic Concepts

One of the most interesting aspects of ion bombardment of solid targets is the production of point defects in the crystalline solid. If the ion flux and energy are sufficiently large, the concentration of defects generated by the ion beam can greatly exceed the thermal equilibrium concentration of point defects. Once formed, defects can conceivably enhance the rate of kinetic processes in the solid where they are generated, or can migrate through the solid. These processes can include impurity diffusion, dislocation motion, crystallization, and grain growth.

Each energetic ion can engage in many displacement-producing colli-

sions before losing all of its incident energy. The recoil atoms may them-
selves cause further displacement collisions until each of them has lost the
energy transferred to it by the incident ion. The entire event takes place
very quickly, in less than approximately 10^{-12} seconds. The array of dam-
age resulting from the stopping of a single incident ion is thus called a
collision cascade.

When a displacement event occurs, each recoil leaves behind it a vacancy
and is itself a high velocity interstitial which comes to rest at the periphery
of the collision cascade. The cascade will thus have a vacancy-rich central
zone and an interstitial rich outer zone, as confirmed by field ion microscopy
studies [46,47,48] and electron microscopy studies [49,50]. The cascade
will have a somewhat ellipsoidal shape, and the center of the ellipsoid will
correspond to a maximum in nuclear stopping. At the peak of the nuclear
stopping curve shown in Fig. 2.7(a), the transferred energy is maximum,
and the ion paths are thought to be as depicted in Fig. 2.7(b). At both
lower and higher energies, the transferred energy per collision is lower so
the ion paths are thought to look like those shown in Fig. 2.7(c).

Of course, defects can be generated thermally as well as by ion bombard-
ment. For comparison sake, it is useful to discuss the energies involved in
thermal point defect creation and motion. Typical energies for vacancy for-
mation are approximately 1 eV for metals (e.g., Au) [51] and approximately
2 eV for elemental semiconductors (e.g., Ge or Si) [52]. In semiconductors
interstitial formation energies are not well known, however they are thought
to be higher than vacancy formation energies. This assumption, by anal-
ogy to the case of metals, would imply diffusion by a vacancy mechanism.
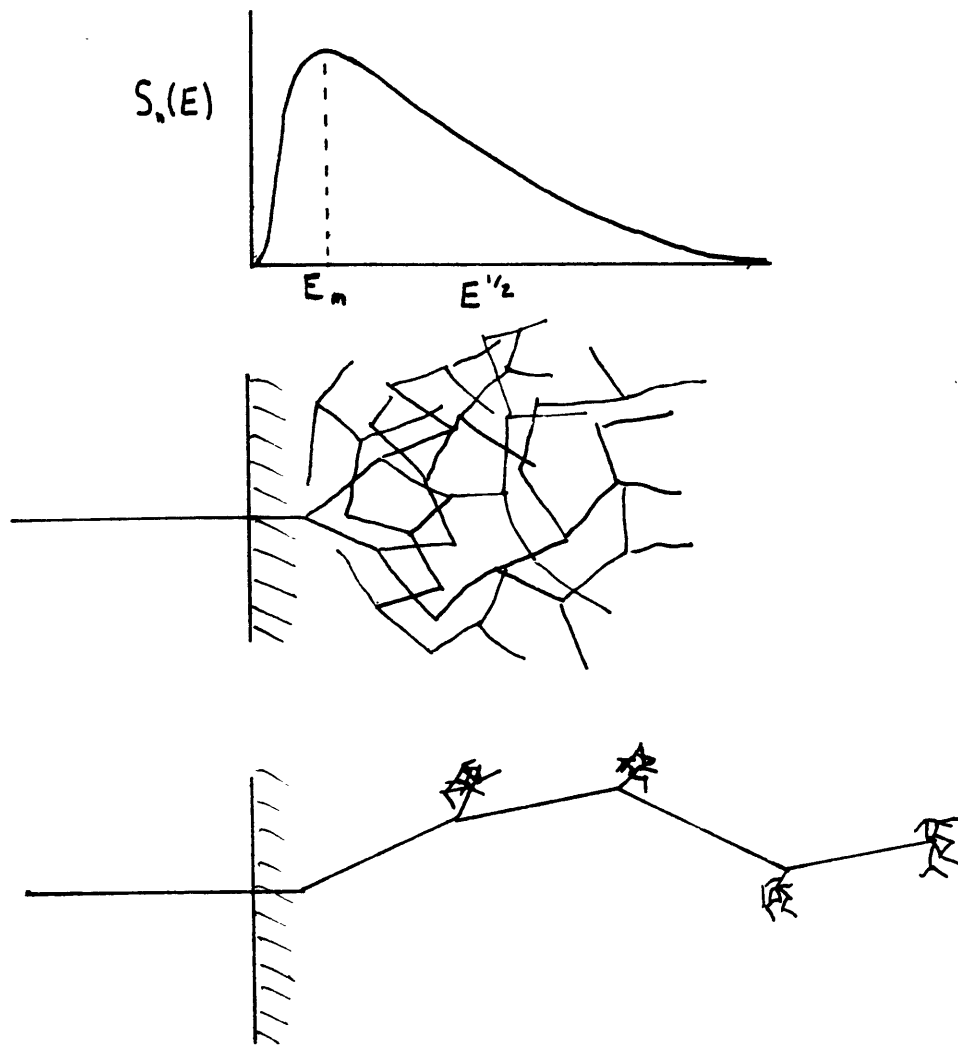
Figure 2.7: In (a), the variation of nuclear stopping with energy is shown. The ion paths at $E = E_m$ are shown in (b), and the ion paths at lower and higher energies are shown in (c).

Although Ge apparently diffuses by a vacancy mechanism, Si does not [52], so the analogy does not seem appropriate. For Si and Ge, estimates for the interstitial formation energy range from a theoretical value of 0.5 eV [53] to several eV [52]. Vacancy migration energy estimates range from approximately 0.5 eV to 1 eV for Si and Ge [53,55]. Interstitial migration energies, even less well known, are estimated at several tenths of an eV in Si and Ge [53,54].

2.5.2 Displacement Energy Estimates

Of considerable interest in analyzing defect production in a solid is the energy required for the incoming ion to displace a target atom, or *displacement energy*. At first thought, one might be tempted to assume that the displacement energy should be related to the measured energies of formation for vacancies and interstitials. However, this notion neglects the fact that the energies of formation are usually measured under isothermal equilibrium conditions. Hence the formation energy of a point defect is measured while its neighbors are all at the same temperature. During ion bombardment, the collision which results in defect formation takes place extremely rapidly (in less than 10^{-12} sec) and the collision process is thought to be quasi-adiabatic. Unlike the struck atom, the neighboring atoms in the solid are at the ambient temperature. In general, the ambient temperature can be much less than the temperature required for defect generation in thermal equilibrium. In fact, some radiation damage experiments are carried out at low temperature so that defect annealing, which can interfere

with an accurate defect count, is avoided.

In the model of Seitz [56], it is assumed that the energy required to create a defect pair in equilibrium is about twice the sublimation energy of the solid. Under the nonequilibrium conditions of the collision event, Seitz assumed that the displacement energy is twice this value, or approximately four times the sublimation energy of the solid. For many solids, the sublimation energy is approximately 5-6 eV, so the displacement energy is estimated to be 20-25 eV.

Some authors [57,58] have included directional effects in the bonding between atoms, a model appropriate for the covalently bonded semiconductors. Assuming a bond energy of 2-4 eV gives a displacement energy of 8-16 eV.

Since semiconductors can be rendered amorphous, an independent check of the estimates of the displacement energy can be made [59]. The critical dose for amorphization at a given ion energy has been measured for Si and Ge [60]. Also, the number of defects created for a given incident ion dose and an assumed displacement energy can be calculated using a Kinchin-Pease model or a more detailed treatment with a TRIM code. One can then adjust the displacement energy until the total number of calculated defects is equal to the number of defects needed to create an amorphous region. If this is done, a displacement energy of approximately 15 eV provides the best agreement with the experimental data for Si.

It is reasonable to assume that the displacement energy is also a function of direction in a solid. Variations in the displacement energies as a function of direction have been calculated [61,62,63] and have been seen
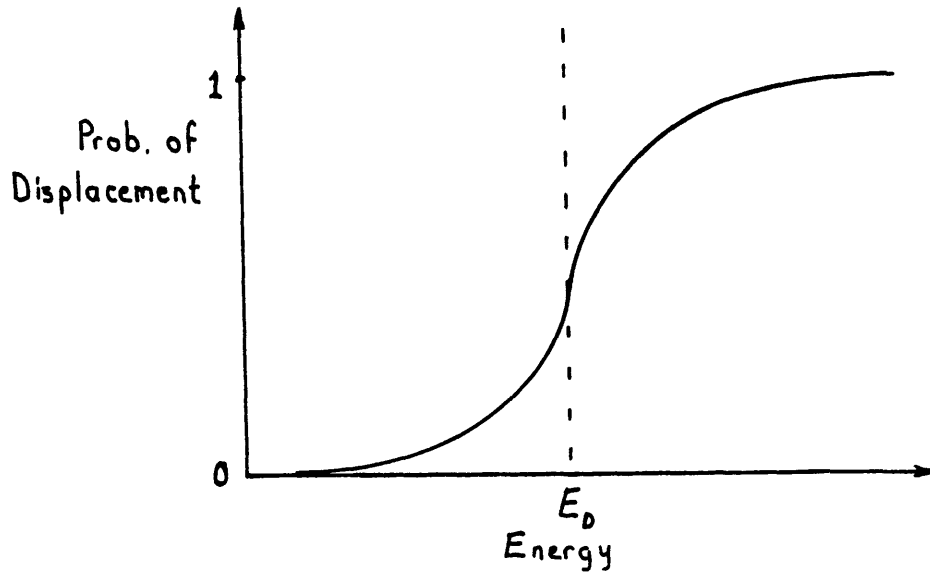
Figure 2.8: The displacement probability as a function of energy, averaged over all scattering angles.

experimentally [64]. Thus, the displacement energy for one scattering angle may be different from the displacement energy for another scattering angle. When collisions in all directions are considered, it may be more useful to think of a displacement probability which rises gradually from zero with increasing energy and approaches unity at some higher energy, rather than rising discontinuously from zero to unity at some specific energy. This idea is depicted in Fig. 2.8 below.

Finally, for the context of this work, it should be pointed out that the displacement energy at a grain boundary may not be equal to the displacement energy for a bulk single crystal. However, since nothing is known about the displacement energy at a grain boundary, it will be assumed to equal the bulk displacement energy.

2.5.3   The Kinchin-Pease Model

One of the most widely cited and simplest models for calculating the number of displaced atoms during a collision is due to Kinchin and Pease [65,66]. Several important simplifying assumptions are requisites of the model.

- Collisions are between like particles (e.g, Si and Si).

- The interatomic potential is a hard sphere potential.

- The target is considered to be amorphous.

- All of the energy transfer is elastic; no inelastic losses are treated.

- All collisions are two body collisions.

- When an incident ion transfers energy to the target, all of the energy is transferred to the target atoms. None is stored as a defect energy in the lattice.

- If a target atom receives less than E_d, it is not displaced. Also, if an incident ion emerges from a collision with $E < E_d$, it does not contribute to further defect production. Thus for $E_d < E < 2E_d$, no increase in the number of displaced atoms occurs.

In a collision with $E \gg E_d$, the probability that an incident particle emerges with energy between E' and dE' is

$$P\{E' < E < E' + dE'\} = \frac{d\sigma}{\sigma} \qquad (2.96)$$

where $E' = E - E_2$. For hard spheres,

$$\frac{d\sigma}{\sigma} = \frac{dE'}{E} = \frac{dE_2}{E} \tag{2.97}$$

The number of collisions produced by a scattered particle, $\mathcal{N}$, is

$$\mathcal{N} = \int_{E_d}^{E} \nu(E') \frac{dE'}{E} \tag{2.98}$$

where $\nu(E')$ is the number of collisions at energy E'. The number of collisions produced by the recoiling target atom, $\mathcal{M}$, is

$$\mathcal{M} = \int_{E_d}^{E} \frac{\nu(E_2)}{E} dE_2 \tag{2.99}$$

The total number of collisions is

$$\nu(E) = \mathcal{N} + \mathcal{M} = \int_{E_d}^{E} \nu(E') \frac{dE'}{E} + \int_{E_d}^{E} \frac{\nu(E_2)}{E} dE_2 \tag{2.100}$$

$$\nu(E) = \frac{2}{E} \int_{E_d}^{E} \nu(x) dx \tag{2.101}$$

For $E^2 \gg E_d^2$,

$$\nu(E) = kE \tag{2.102}$$

The boundary conditions for the assumptions made are

1. $\nu(E) = 0$, for $E < E_d$

2. $\nu(E) = 1$, for $E_d < E < 2E_d$

3. $\nu(E) = 1$, for $E = 2E_d$

These conditions give

$$k = \frac{1}{2E_d} \tag{2.103}$$

or

$$\nu(E) = \frac{E}{2E_d} \qquad (2.104)$$

for $E \gg E_d$. Kinchin and Pease also assumed that for energies higher than the threshold energy for efficient ionization, E_c, the displacement density was constant at

$$\nu(E) = \frac{E_c}{2E_d} \qquad (2.105)$$

2.5.4 Other Models

Improvements to the Kinchin-Pease model have been developed by other workers. Sigmund and Sanders [68,67] replaced the hard sphere potential with an inverse power potential, which gives for s = 1

$$\nu(E) = 0.52 \frac{E}{2E_d} \qquad (2.106)$$

At high energies, the neglect of inelastic energy losses is a serious problem. Linhard, Winterbon, and Brice [69,70,71] have developed modifications of the Kinchin-Pease model in which the contributions from electronic and nuclear stopping are separately assessed. Below E_c, the basic result of these improved models for electronic stopping is to reduce the number of displacements per incident ion by 10-20 percent. Above E_c, $\nu(E)$ rises in a sublinear fashion with increasing energy.

The dimensions of the collision cascade have been analyzed by Winterbon, Sigmund and Sanders [35] using a Boltzmann transport analysis. The analysis yields values for the moments of the damage distribution rather

than an expression for the distribution itself. Several important observations can be drawn from the analysis:

- The mean range of the incident ions is greater than the mean depth of the damage distribution.

- The standard deviation or straggle of the damage distribution is less than the mean depth of the damage distribution, except when $M_2 \gg M_1$.

- The transverse straggle of the damage distribution is less than the longitudinal straggle.

- The damage profile deviates from a Gaussian shape much more markedly than does the incident ion range.

2.6 High Density Cascades

When the mean path length of the ion between collisions approaches the lattice constant, we can no longer model the cascade using the binary collision approximation. This phenomenon, which was first proposed by Brinkman [72,73], is a common occurrence during heavy ion bombardment at low energies. The models for what happens when the ion path length approaches a lattice constant are not well developed. Nonetheless, there is significant experimental evidence, based on sputtering and damage production for a regime which cannot be described by linear cascade theory [26,27,28].

2.6.1   Damage Production

The case of damage production at low energies offers an example of an ion-solid interaction which is nonlinear in the deposited nuclear energy. Figure 2.9 illustrates experimental results of Walker and Thompson [74] on the number of displaced silicon atoms per incident ion, N_D, versus the energy deposited in nuclear collisions. Several features of this data are noteworthy. First, the slope of the experimental curves are higher than that of the displacements predicted by the Kinchin-Pease model, shown as a dotted line in Fig. 2.9. That is, there is initially a superlinear increase in N_D with increasing deposited nuclear energy. At higher energies, the slopes approach that of the Kinchin-Pease curve, which is plausible since we expect that the path length will be longer than the lattice parameter at some higher energy. Similar experiments were performed with germanium substrates and As^+, Te^+, and Tl^+ ions. Computer simulations corroborated the onset of the high density cascade regime [79].

Sigmund [75] has pointed out that quenching times of a thermal spike within the region of an ion track is 10^{-12}-10^{-13} sec. Comparisons can be made between the quenching behavior of an ultra-short laser pulse and an ion. Consideration of the planar geometry of an energy spike leads to the prediction of a shorter quenching time for the energy spike [28]. Such a quenching rate leads to the prediction of an interface velocity during crystallization of at least hundreds of meters per second. Transient conductance experiments have demonstrated that when the interfacial velocity is greater than approximately 15 m/sec, the regrown layer is amorphous [76].
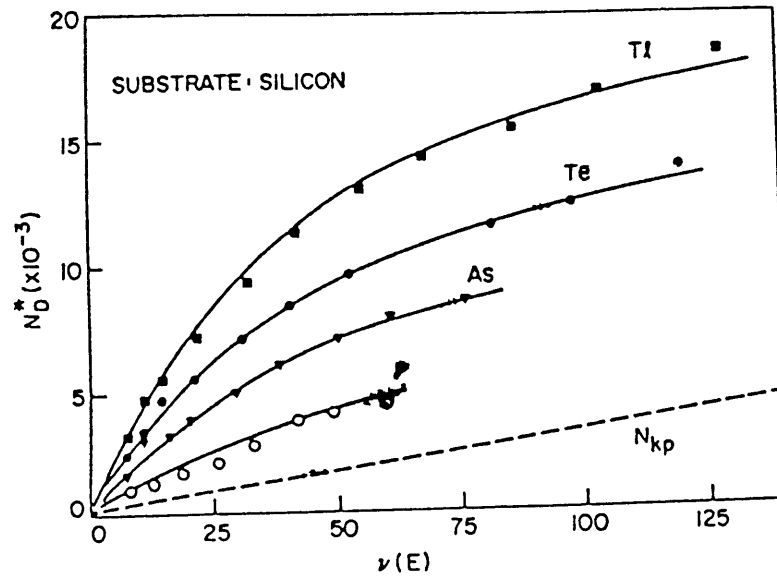
Figure 2.9: Variation of total number of displaced silicon atoms per incident ion with the total energy deposited in nuclear collisions. The dashed line is the number of displaced atoms/ion predicted by the Kinchin-Pease formula.

One might speculate, therefore, that an ion which has generated a high density cascade, or energy spike, might leave amorphous zones in its wake. This speculation has been substantiated by the very interesting finding of amorphous zones following bombardment of silicon by low energy Bi^+ ions [77,78]. TEM observation revealed amorphous regions ranging from 25-50 Å in diameter. Annealing studies revealed that the incident ion mass had a pronounced effect on the type and extent of damage production. In general, heavier ions produced more extensive damage which required higher annealing temperatures [80].

2.6.2 Sputtering Yield

Another indication of the onset of a high density cascade can be seen by examining the sputtering yield as a function of the density of nuclear energy deposited in a solid. Figure 2.9 is a plot of the total sputtering yields of Ag, Au, and Pt as a function of F_D, the collisional energy density deposited at the surface [81]. For low energy densities, the yield of sputtered particles is linearly proportional to the deposited energy density. At approximately $F_D = 1\text{-}4$ eV/atom, the sputtered particle yield changes from a linear to a cubic dependence on the deposited energy density. This clearly indicates a departure from the linear collision cascade regime. However, the cubic dependence is interesting, since evaporation of a heated surface layer is expected to vary as the square of the deposited energy density [82]. Referring to Fig. 2.10 reveals that the break in the data occurs at sputtered particle yields of approximately 20. This may indicate a change in the surface
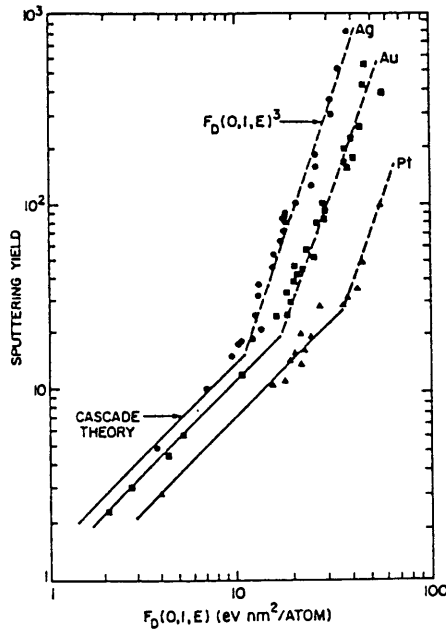
Figure 2.10: Sputtering yields for Ag, Au and Pt as a function of the nuclear energy density deposited at the surface.

binding energy at high sputter yields.

2.7 Simulation of Ion-Solid Interactions

2.7.1 An Overview

Because ion-solid interactions affect very small volumes during very short periods of time, it is extremely difficult to directly access these interactions with experimental probes which have sufficient temporal and spatial resolution. Therefore, the study of ion-solid interactions relies heavily on

indirect methods. Experimentally, these methods consist of "post-mortem" or after-the-fact observations performed hours or days after the experiment is over. Examples include TEM and electrical measurements of the implanted layers.

Direct study of ion-solid interactions can be approached theoretically as well as experimentally. The development of powerful computers has allowed rapid progress in the simulation of ion-solid interactions. Although computers have long been used to calculate moments of the range and damage distribution [34,45], they have recently also been used to great advantage to perform atomistic simulations in which the histories of individual ions are recorded. It is these Monte-Carlo type simulation programs that are discussed in this section. Such programs are extremely useful because they give estimates for quantities which are very difficult to measure, such as the point defect populations generated by an incident ion and the fractions of the total ion energy which go into nuclear, electronic and phonon energy loss. The Monte-Carlo simulations also predict quantities which can be related to experimentally measured quantities, such as the projected range and straggle for both incident and knock-on ions.

Several different simulation programs have been developed [40,83,90] Only the MARLOWE program of Oen and coworkers [40,87] includes an exact numerical computation of the classical scattering integral. Some authors base their formalisms on the momentum approximation [90,91] or fitted truncated Coulomb potentials [84,88,89]. An important simplification of the center-of-mass scattering problem has been developed by Biersack [42] which allows an analytical evaluation of the scattering angle. Because
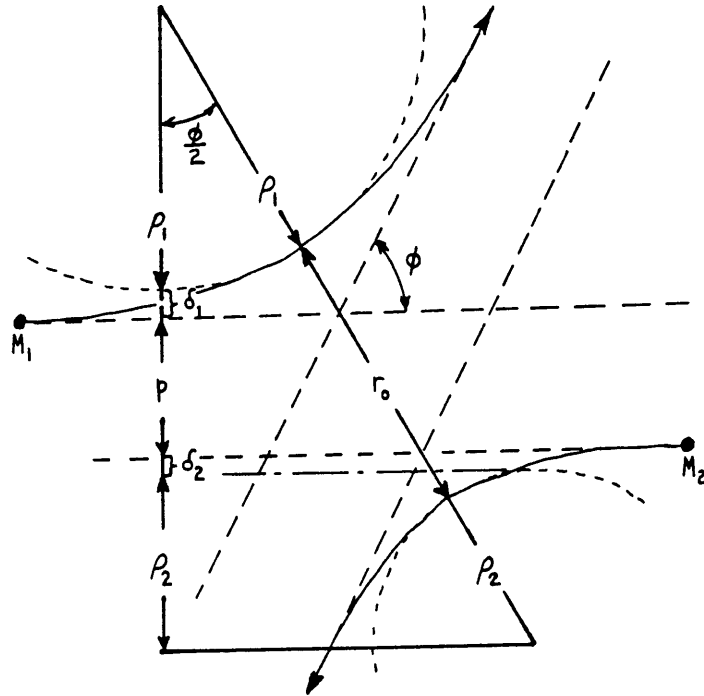
Figure 2.11: The scattering triangle in the center of mass coordinate system

of this trick, the program of Biersack, et. al., which has been named TRIM, provides an unusual combination of precision and computational efficiency. Hence it is deserving of special mention.

2.7.2 TRIM

Although there are, at this point, many versions of TRIM, they all rely on a common scattering formalism outlined by Biersack, et. al. in 1980 [42]. The crux of Biersack's formalism is the scattering triangle, shown in Fig. 2.11.

By inspection of the scattering triangle,

$$\cos \frac{\theta}{2} = \frac{\rho + p + \delta}{\rho + r_o} \qquad (2.107)$$

where $\rho = \rho_1 + \rho_2$, and $\delta = \delta_1 + \delta_2$. The parameters ρ_1 and ρ_2 are the radii of curvature and δ_1 and δ_2 are correction terms in the scattering triangle. The value of r_o is obtained from

$$1 - \frac{V(r_o)}{E_c} - \left(\frac{p}{r_o}\right)^2 = 0 \qquad (2.108)$$

where $E_c = 1/2(M_1 v_1^2 + M_2 v_2^2) + V(r_o)$. This equation can be solved iteratively in a few steps. The value for ρ can be found from the centrifugal force, f_c, on the particles

$$\rho = (M_1 v_1^2 + M_2 v_2^2)/f_c \qquad (2.109)$$

The centrifugal force is the gradient of the interatomic potential at r_o.

$$\rho = \frac{2[E_c - V(r_o)]}{-V'(r_o)} \qquad (2.110)$$

The authors have developed a fitting formula for δ.

The original TRIM code employed a Molière potential at low energies and an unscreened Coulomb potential at higher energies. Recently, Ziegler, et. al. have developed a TRIM code which employs the Universal potential [30]. This program is designated TRIM followed by the year of its release; e.g., TRIM-86. TRIM uses the Linhard model for inelastic scattering.

In the basic version of TRIM, defect populations are calculated using a modified Kinchin-Pease formula [92,93]. An improved model which follows individual knock-ons, as well as incident ions, has also been developed. This model, called TRIM-CAS, provides an accurate count of the defects produced, but is computationally more demanding.

Chapter 3

Ion Beam Enhanced Grain

Growth

This chapter discusses research on a new application of ion bombardment to enhance the kinetics of a solid-state process, ion beam enhanced grain growth (IBEGG). The microstructure of thin films of Ge, Au and Si was studied both qualitatively and quantitatively during IBEGG. The experimental procedure, including deposition, thermal annealing, ion beam parameters, observation by transmission electron microscopy, and data acquisition are described. Monte Carlo simulation of ion transport in the thin films of interest here was studied using the TRIM computer program. The dependence of thermal and ion beam enhanced grain growth upon various kinetic parameters is presented for three experimental systems. Finally, a

model for ion beam enhanced grain growth, which accounts for the results obtained, is developed. This model suggests a simple mechanism for the growth process.

3.1 Experimental Procedure

The final microstructure of a thin film is influenced by all of the various phase transformations and kinetic processes which occur during each stage of an experiment. Therefore, it is essential to monitor the microstructure of the film at each stage during experiments. Hence the microstructure of the film was characterized by transmission electron microscopy (TEM), transmission electron diffraction (TED), and cross-sectional transmission electron microscopy (XTEM) after (1) deposition (2) crystallization (3) grain growth during thermal annealing and (4) ion beam enhanced grain growth.

3.1.1 Sample Preparation

Germanium Thin Films

Thin germanium films were prepared in several ways:

1. Unsupported (freestanding) films were formed by room temperature electron beam evaporation of Ge onto freshly cleaved NaCl substrates. The evaporation rate was 10 Å/sec. These films were floated off the NaCl substrates in deionized water (DI-H_2O) onto TEM Grids. These

samples were amorphous as-deposited, as indicated by transmission electron diffraction. The Ge film underwent crystallization while being heated to the temperature for ion beam enhanced grain growth, as illustrated by the micrographs in Fig. 3.1. The crystallized films exhibited a random polycrystalline texture, as measured by transmission electron diffraction. All Ge samples are 500 Å thick, unless otherwise noted.

2. Samples were formed by room-temperature electron beam evaporation of Ge onto clean thermally grown SiO_2 on Si substrates. The substrates were cleaned using a standard RCA cleaning procedure, and were either immediately loaded into the evaporation chamber or stored under rough vacuum until being loaded. Cleanliness was monitored using the steam nucleation test[1]. The SiO_2 was grown by a dry oxidation process at 1050 °C on (100) Si wafers, and the thickness ranged from 910 - 1150 Å, as measured by an ellipsometer. These Ge samples were also presumably amorphous as-deposited, and were crystallized while being heated to the temperature for ion beam enhanced grain growth, as shown in Fig. 3.2. The crystallographic texture of these films appeared to be random.

3. Samples were deposited onto clean thermally grown SiO_2 on Si substrates at a temperature of 400 °C. These samples were found to be polycrystalline, as seen in Fig. 3.3. These films also exhibited ran-

---

[1]The steam nucleation test is a standard procedure of the MIT Submicron Structures lab. A description can be found in the lab procedure book.

dom polycrystalline texture. The polycrystalline as-deposited films prepared by this method exhibited columnar morphology, while the amorphous-deposited films that were subsequently crystallized were noncolumnar. This is shown in the cross-sectional transmission electron micrographs of Fig. 3.4.

Silicon Thin Films

Silicon films were deposited on thermally grown SiO_2 by room temperature electron beam evaporation, at a deposition of 1 Å/sec. As with Ge films, the Si films were crystallized while being heated to the temperature for ion beam enhanced grain growth. These films also exhibited random polycrystalline texture, All Si films are 1000 Å thick, unless otherwise noted. Figure 3.5 shows the amorphous as-deposited film after crystallization. In Fig. 3.6, a cross-sectional view of the as-deposited film is shown.

Gold Thin Films

Gold films were deposited onto cleaned SiO_2 substrates by room temperature electron beam evaporation, at a rate of 10 Å/sec. Some of the films were 250 Å thick, and others were 500 Å thick. The films were then floated off the SiO_2 as soon as possible after deposition onto TEM grids in DI-H_2O. Typically, this time was 10 min.

Gold films are polycrystalline when deposited at room temperature, as seen in Fig. 3.7. A small fraction of the 250 Å thick film in Fig. 3.7
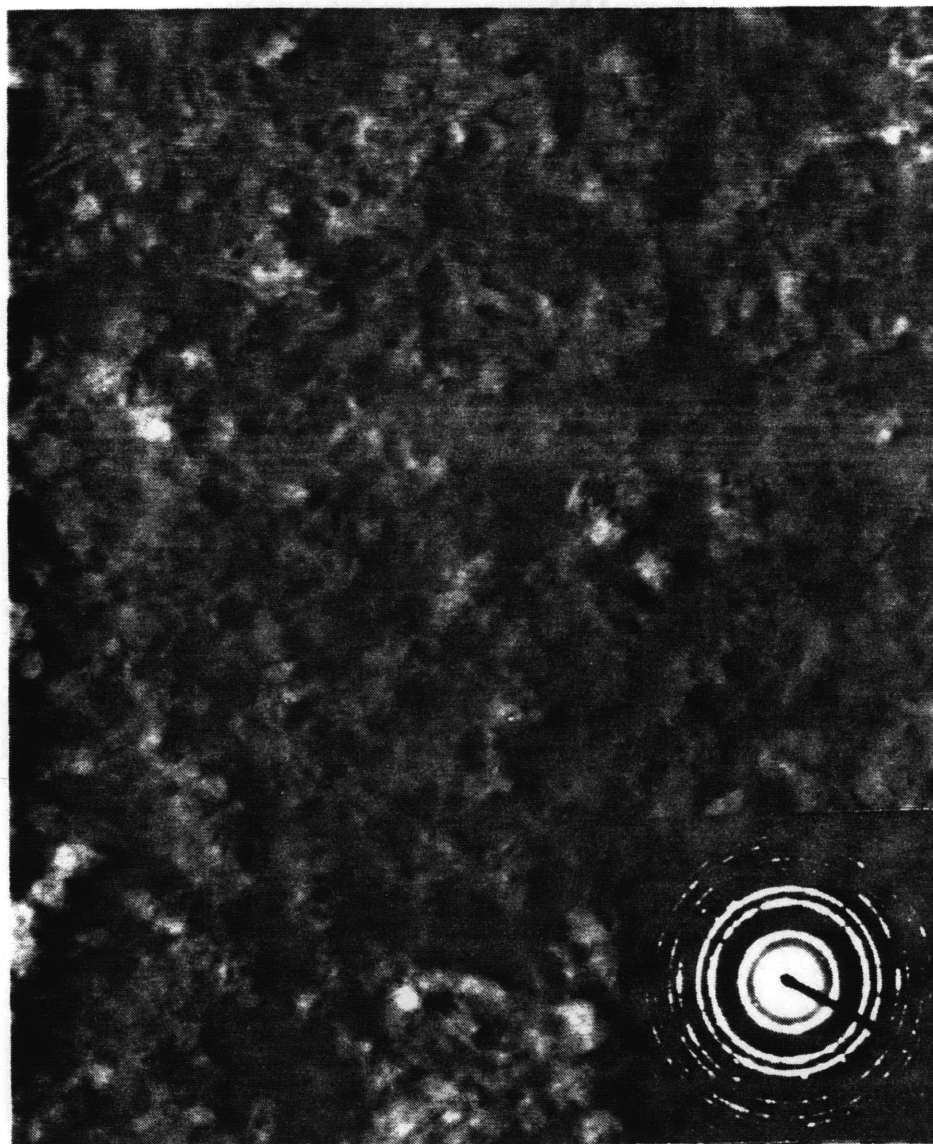
Figure 3.1: Transmission electron micrograph and transmission electron diffraction pattern for unsupported amorphous as-deposited Ge film after crystallization.
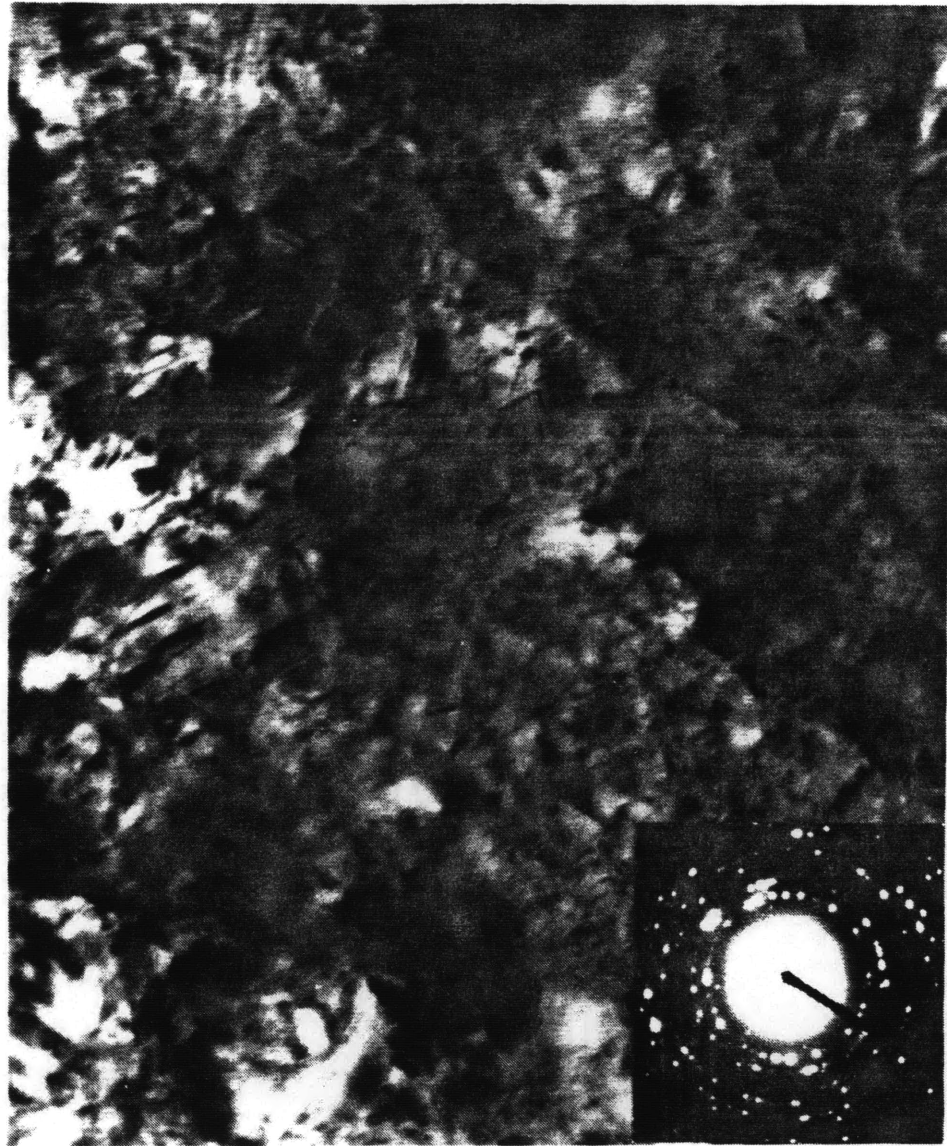
Figure 3.2: Transmission electron micrograph and transmission electron diffraction pattern for amorphous as-deposited Ge film on thermal SiO$_2$ after crystallization.

Figure 3.3: Transmission electron micrograph and transmission electron diffraction pattern for polycrystalline as-deposited Ge film on thermal SiO_2 after deposition at 400 °C.
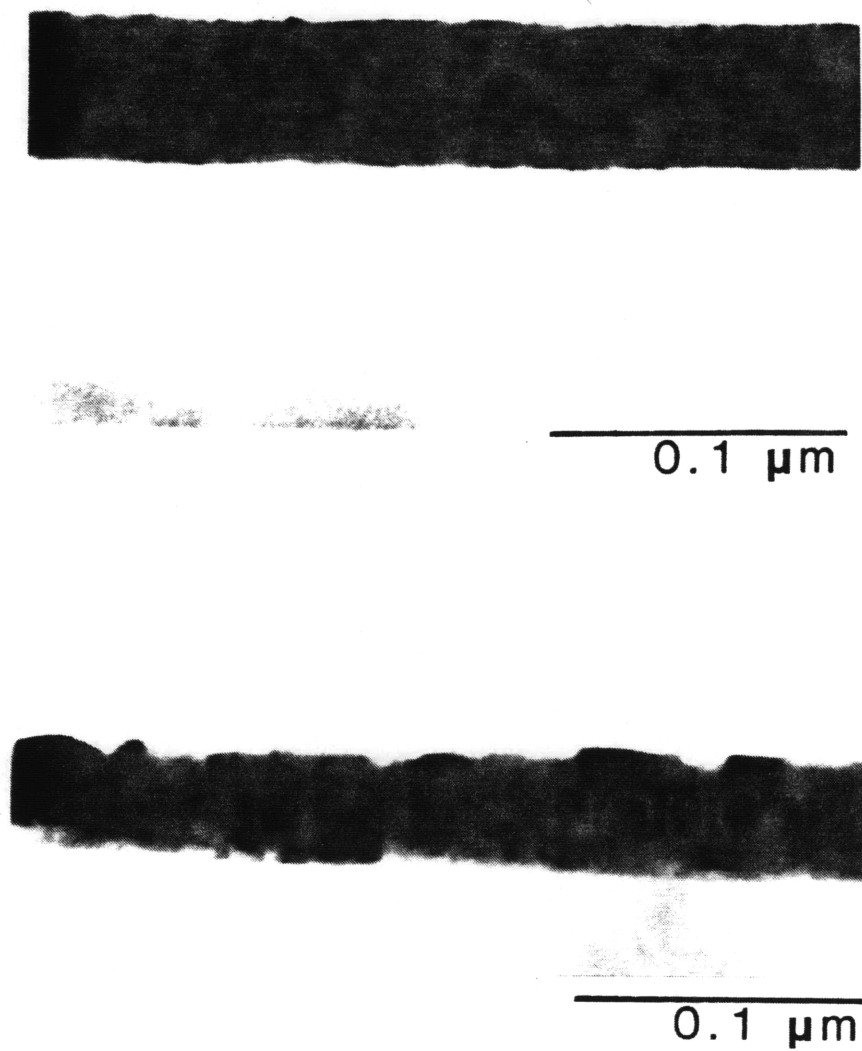
Figure 3.4: Cross-sectional electron micrographs of (a) an amorphous as-deposited Ge film after crystallization and (b) a polycrystalline as-deposited Ge film.

has undergone secondary grain growth [2]. The crystallographic texture in the as-deposited films was random. Wong [16] has shown that gold films adhere poorly to SiO_2 substrates, and thus can be floated off. He has also shown [16] that grain growth in thin gold films occurs readily at room temperature on SiO_2 substrates but that it virtually stops in films that have been rendered freestanding. In order to prevent confusion between thermal and ion beam enhanced grain growth, freestanding gold films were used exclusively in the experiments described herein. That is, thermally induced grain growth is halted in freestanding films.

3.1.2   Thermal Annealing

The samples that were subjected to thermal annealing were placed in quartz ampules which were pumped to approximately 10^{-7} Torr by a turbomolecular pump. The ampules were then sealed under vacuum and annealed in a constant temperature furnace. After deposition and prior to annealing, silicon samples were cleaned using a standard RCA-1 cleaning procedure. The germanium samples were cleaned in an ultraviolet-ozone cleaning system. Several wet chemical cleaning approaches similar to the silicon RCA clean were tried, but were not used because they resulted in removal of the

---

[2]Grain growth is discussed briefly in the section on modeling of ion beam enhanced grain growth which follows. A recent model for surface-energy-driven secondary grain growth can be found in [17]. A brief, general review of recovery, recrystallization and grain growth can be found in [16].
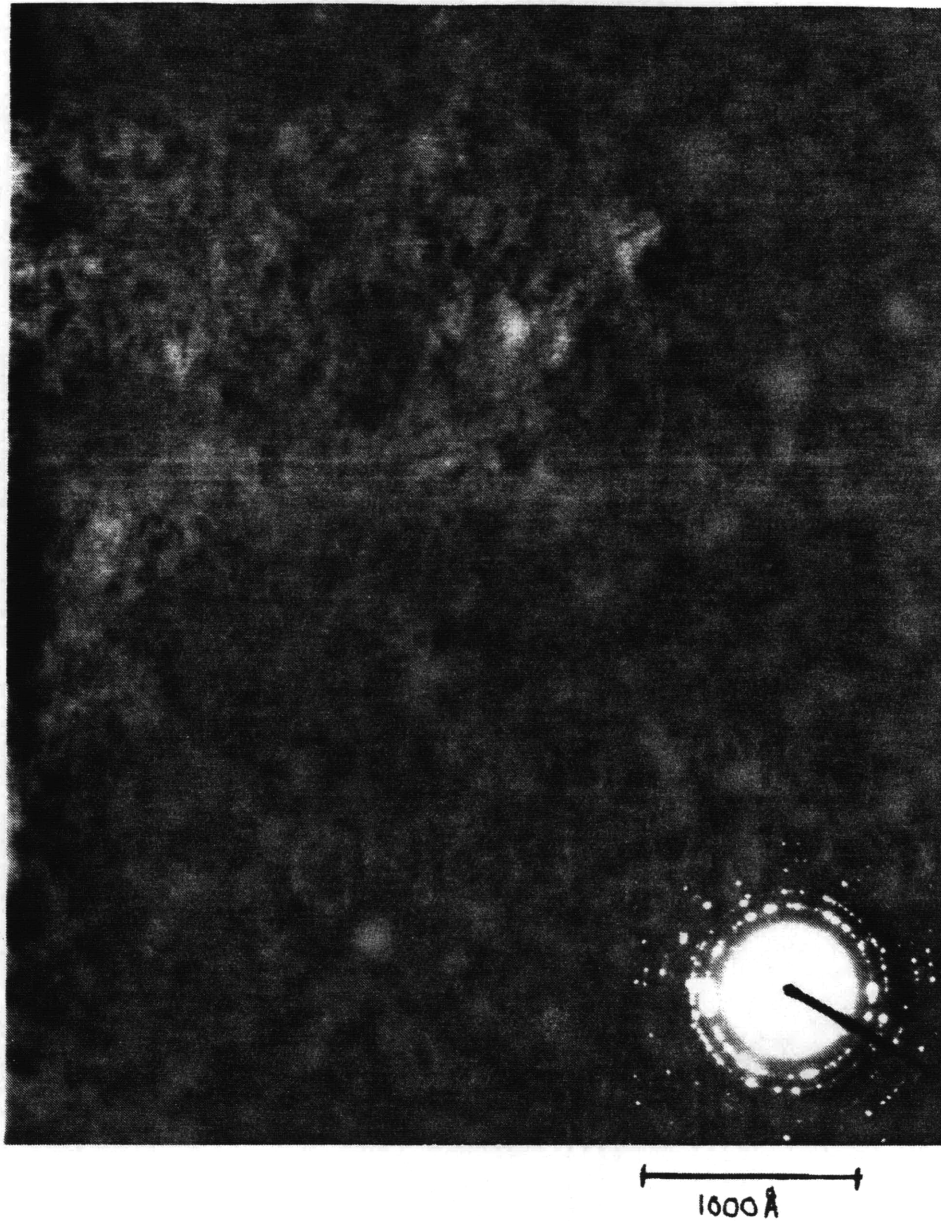
Figure 3.5: Transmission electron micrograph and transmission electron diffraction pattern for amorphous as-deposited Si film on thermal SiO_2 after crystallization.
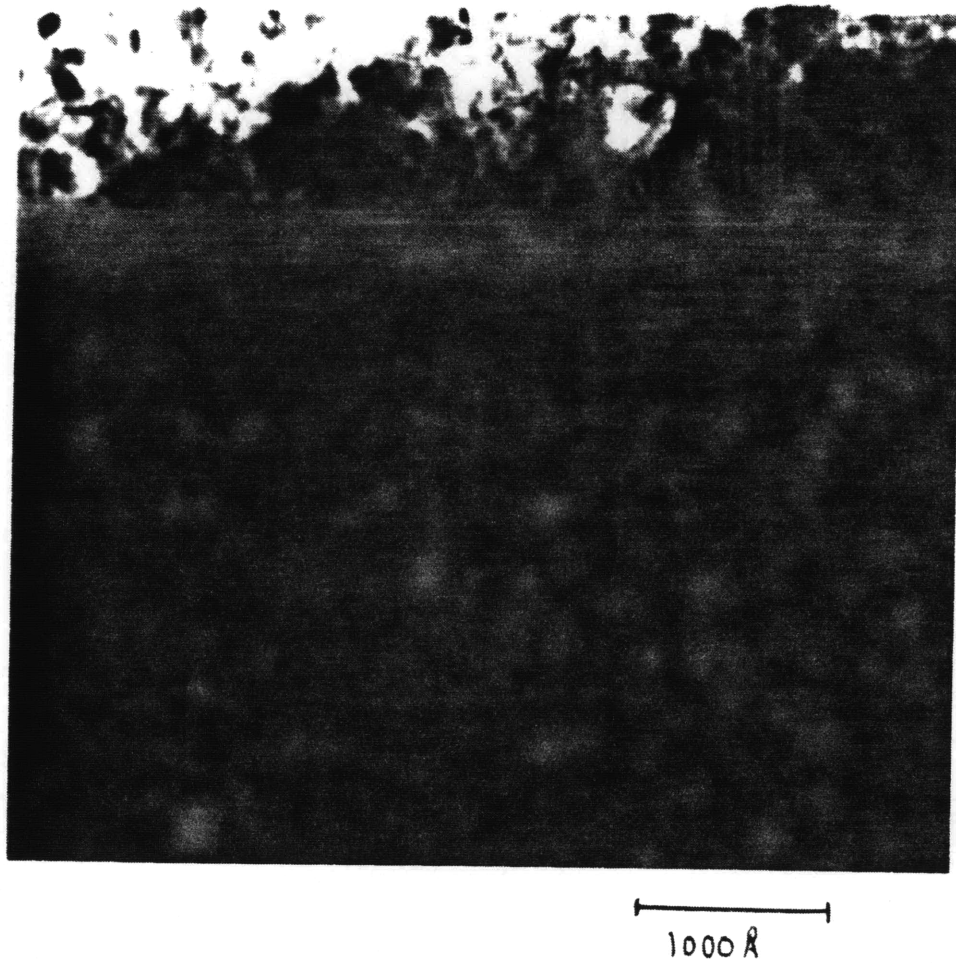
Figure 3.6:   Cross-sectional electron micrographs of an amorphous as-deposited 1000 Å thick Si film on SiO_2 after crystallization.
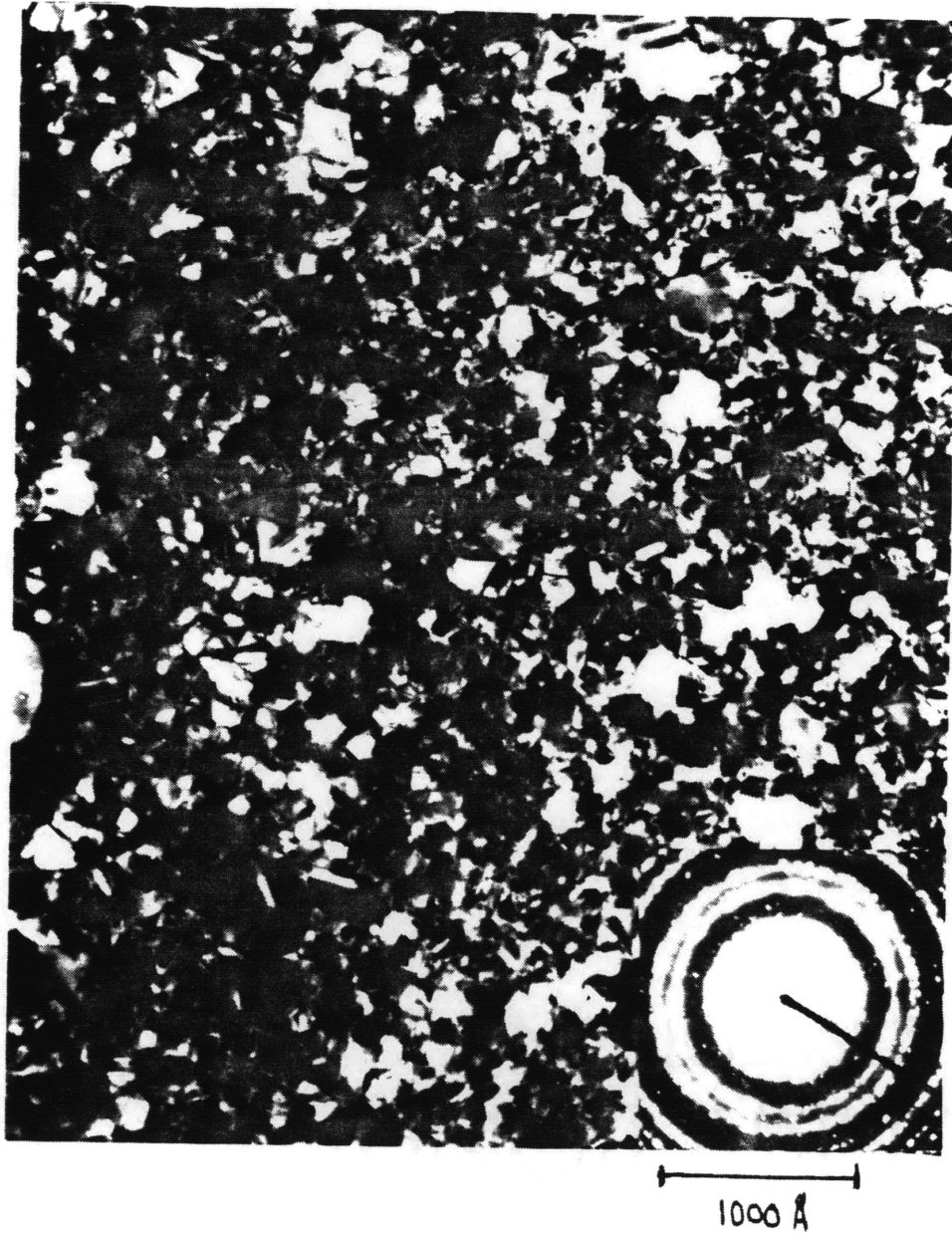
Figure 3.7: Transmission electron micrograph and transmission electron diffraction pattern for polycrystalline as-deposited Au film, deposited on thermal SiO_2 substrate and after removal from the substrate.

germanium film. The Au films were also cleaned in an ultraviolet-ozone cleaning system prior to grain growth.

3.1.3 Ion Beam Apparatus

Several ion implanters were used during the course of this work[3]. The details of accelerator design and configuration are, for the most part, unimportant to the process of ion beam enhanced grain growth.

The projectile ions were chosen to be either native species($i.e.$, Ge^+ in Ge) or noble gases in order to avoid confusion between physical and chemical kinetic enhancement, such as dopant enhanced boundary migration[15,94,95,96]. In all cases, the base pressure in the implantation chamber was between 5 x 10^{-7} Torr and 1 x 10^{-6} Torr. Source gas purity was in the ppm range, and mass separation was used to generate a beam consisting only of the source gas material. Silicon and germanium beams were generated by creating a discharge in silane or germane gas. Beams of Ar^+, Kr^+, and Xe^+ were generated using research purity monatomic gas sources.

Since it is sometimes a problem, a comment should be made about the purity of silicon beams. Impurities can be inadvertently implanted when

---

[3] The Eaton-Nova 200 at Surface Alloys Corp., Danvers, MA was used for initial experiments with Ge and Au films. Subsequent work on Ge and Si films was carried out using the custom-designed 400 keV implanter at MIT Lincoln Laboratory. Subsequent work on Au films was performed using the 250 keV implanter of the MIT Center for Materials Science and Engineering.

^{28}Si is the source gas, even when mass separation is employed because CO radicals also have a mass of 28 amu. One approach to eliminating the problem is to use ^{30}Si as the source gas. However, ^{30}Si is very expensive. The approach taken in this work was to monitor the ratio of the total ion beam current to the current due to background impurities when the source gas is turned off. During this work, the ratio of total beam current to background beam current was in the range of 300:1 to 1000:1, which was considered an acceptable level.

Heating stages were designed for both the Eaton-Nova machine and the 400 keV Lincoln Lab machine. Although different in detail, they were conceptually identical. The stage designed for the Lincoln Lab machine is shown schematically in Fig. 3.8. The entire stage is mounted on an O-ring seal flange. High current electrical feedthroughs were welded onto the flange. Clamps were attached to the ends of the feedthrough which held the resistively heated graphite heater in place. Samples were placed directly on the 40 mil-thick graphite heater and clamped with graphite tabs. Temperature measurement was made by embedding chromel-alumel thermocouple junctions fashioned out of 5 mil wire within the graphite strip. Two thermocouples were used, with one attached to the bottom of the strip and the other attached to the top of the strip. The thermocouple readings agreed within approximately ± 10 °C. Between 650 °C and 900°C, the thermocouple readings were compared with measurements made using a disappearing filament-type optical pyrometer. The pyrometric temperature measurements were compared with similar measurements made with Si substrates annealed under vacuum in a constant temperature furnace. Power was sup-

plied to the graphite strip by a Research, Inc. Model 662 phase-angle power controller, through a 20:1 voltage step-down transformer. A Research, Inc., microprocessor controller was programmed to receive the temperature measurement from the thermocouple and control the power delivered to the graphite strip by the power controller. This feedback system maintained a constant temperature within ±5°C. From pyrometric measurements, the Si substrate material was found to be approximately 50 °C lower than the stage temperature measured by the thermocouples. For temperatures lower than 650 °C, which could not be probed by the optical pyrometer, the substrate temperature was assumed also to be approximately 50 °C lower than the stage temperature. The hot stage has been operated at temperatures as high as 1100 °C, and is probably capable of higher temperatures[4]. At temperatures above 700 °C, a box fan was used to cool the flange on which the stage is mounted.

3.1.4 Transmission Electron Microscopy

The film microstructure and crystallographic orientation were characterized by transmission electron microscopy (TEM) and transmission electron diffraction (TED) using JEOL JEM-200CX electron microscopes. The grain size and morphology were examined by bright field and dark field TEM. The grains imaged in bright and dark field micrographs were dig-

---

[4]The greatest limitation on stage temperature is heating of the end station chamber to the point where the O-rings outgas appreciably, or are damaged. By using a smaller graphite heater strip, higher temperatures can be achieved with the same total power.

To External Circuit

High-Current

Electrodes→

O-ring Seal

Alumina Beads

Thermocouple

0.040" Graphite Strip

Substrate
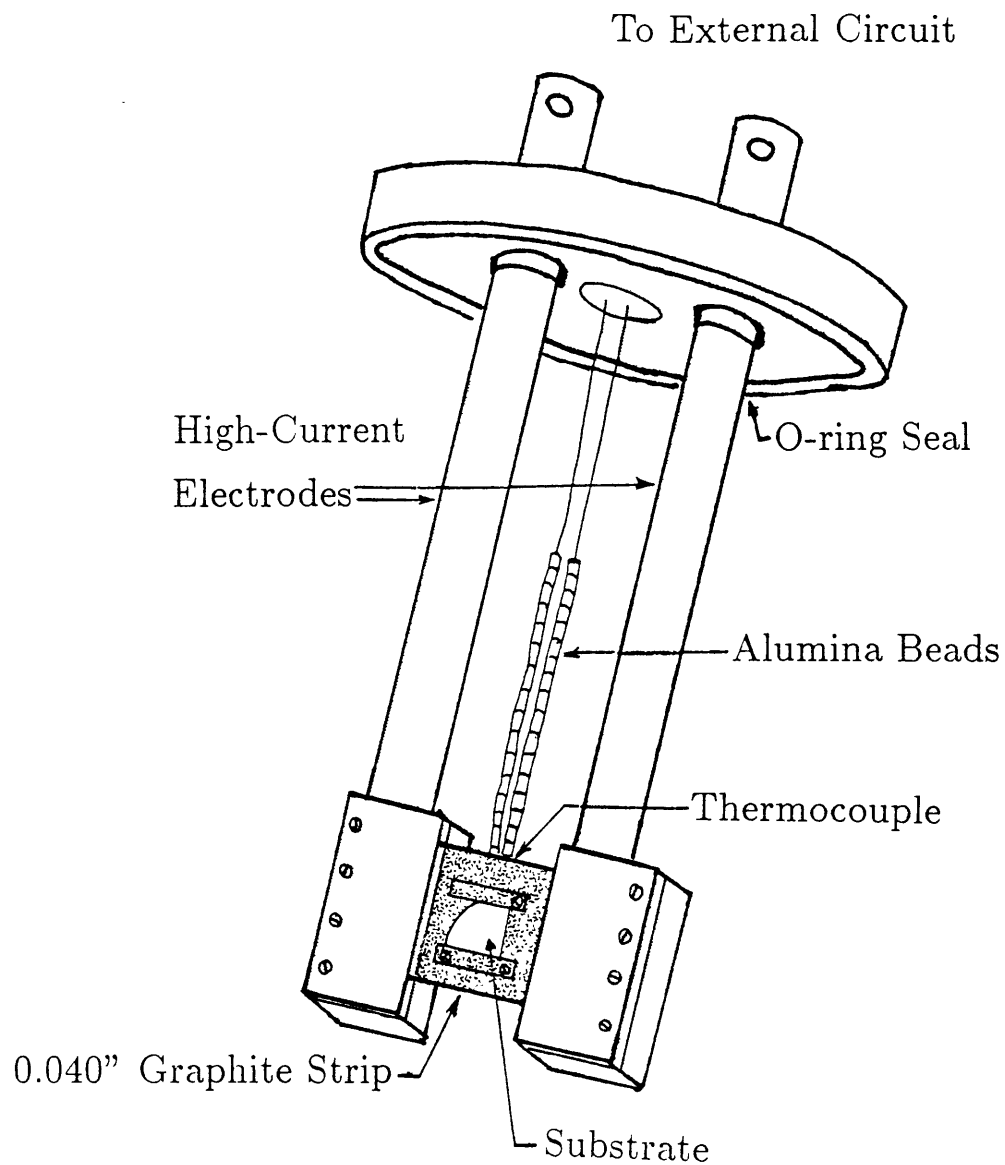
Figure 3.8: Schematic of hot stage designed for the MIT Lincoln Laboratory 400 keV ion implanter.

itized to facilitate computer generation of grain size distributions. Grain size data were fitted to lognormal distributions. Because individual grains in a film with noncolumnar structure are difficult to resolve in bright field, grain size measurements in the non-columnar films were taken from dark field micrographs. The grain size measurements in the columnar films were derived from both bright field and dark field micrographs, which gave identical results. X-ray microanalysis and microdiffraction data were taken on selected samples using a VG HB-5 scanning transmission electron microscope.

Conventional TEM samples were prepared using two techniques. First, some films were floated onto TEM grids prior to grain growth. These samples were simply viewed as-is in the TEM. Second, for films on thermally oxidized Si wafers, samples were thinned by etching the Si substrate. This backside etching technique is depicted schematically in Fig. 3.9. After grain growth and prior to thinning, the samples are scribed and broken into 2 x 2 mm squares. Then the samples are placed face down on a clean glass microscope slide. Black wax is applied to the edges of the sample, so as to protect the film from the etching solution. A circular spot in the center of the sample approximately 0.5 mm in diameter is left uncovered with black wax. Then a 1:1 solution of concentrated hydrofluoric acid (HF) and nitric acid (HNO_3) totaling 10 ml is mixed. This etching solution is applied to the opening in the black wax mask on the sample, one drop at a time, using a capillary tube. The rate of etching is monitored visually under a

3x stereomicroscope[5]. Gaseous reaction products cause the drop of etching solution to bubble, giving an indication of the etching rate. The HF-HNO$_3$ etching solution etches the Si somewhat selectively with respect to the SiO$_2$ layer. When the SiO$_2$ layer is reached, the appearance of the region being etched changes from dull to shiny. This is a cue to stop etching the Si substrate by immersing the sample in DI-H$_2$O. The sample is now removed from the glass slide by dissolving the black wax in (1,1,1) trichloroethane[6]. Using this technique, membranes which are several hundred microns in diameter can be obtained. This backetching technique has two advantages over conventional jet etching methods for sample preparation. First, it is applicable to materials which are opaque in thin film form, such as metals. Second, if proper ventilation is used, it is somewhat safer, since the total volume of etching solution is small (10 ml).

Cross-sectional TEM samples were prepared with Ge and Si films deposited on thermally oxidized Si wafers. The fabrication procedure used to prepare cross-sectional TEM samples is given in Appendix A.

3.1.5   Grain Size Data Acquisition and Analysis

Grain size data was collected by digitizing grains imaged in plan view electron micrographs, and forming grain size distributions. The micrographs were photographically enlarged so that the grain size on the printed mi-

---

[5]This procedure should *only* be performed under a well ventilated hood.

[6](1,1,1) trichloroethane is a less toxic substitute for trichloroethylene.
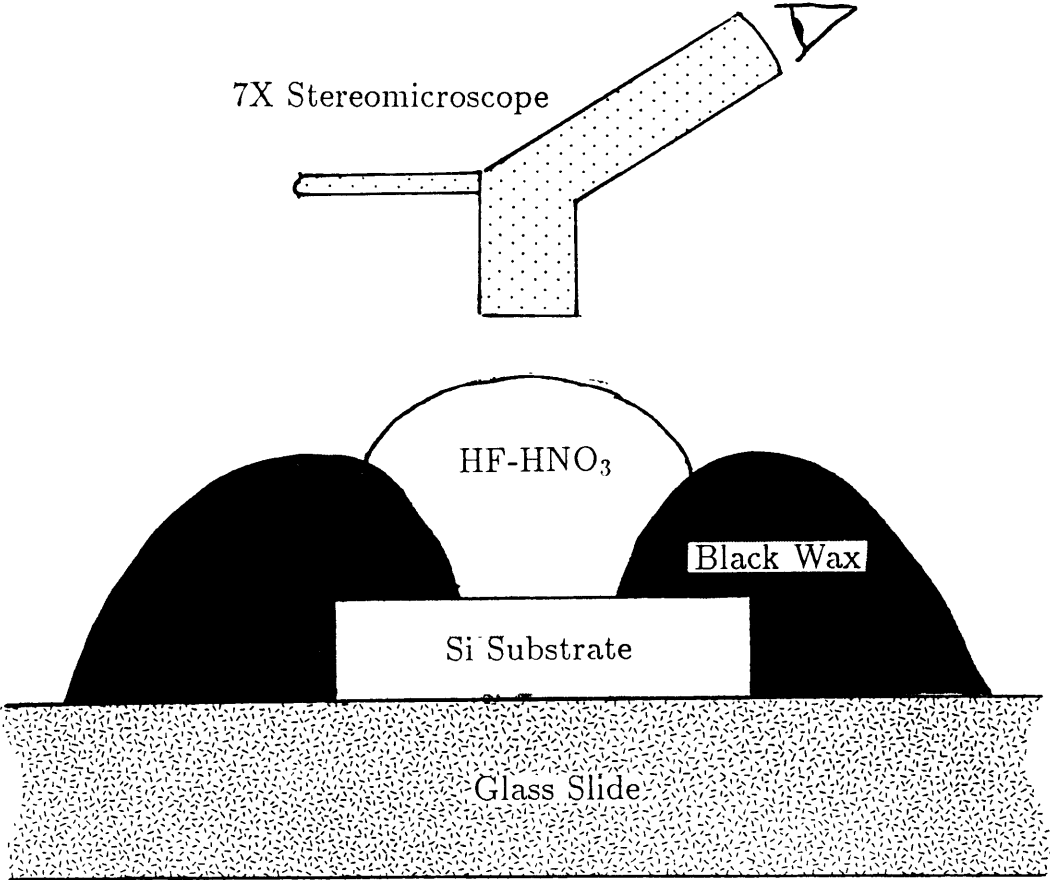
Figure 3.9: Schematic of backside etching technique for TEM specimen preparation

crograph was large compared to the measurement error in the digitizing process. Digitizing was done manually using a Summagraphics digitizing tablet and a program developed for the IBM PC in BASIC[97]. The parameter used to measure grain size was the maxmimum dimension of a grain. The data thus collected was formed into grain size distributions, which typically included 400 - 1000 grains. The distributions were approximately lognormal for all the experiments conducted in this work. This is consistent with previous observation of grain size distributions in normal grain growth[6,103].

3.1.6 TRIM Calculations

The TRIM-86 Monte-Carlo simulation program [105] was used for various ion transport calculations[7]. The program, implemented on an IBM PC, was used to determine the projected range of implanted ions, and to estimate the Frenkel defect yield per incident ion via a modified Kinchin Pease algorithm, as discussed in Chapter 2. The program requires as an input the displacement energy of an atom on a lattice site. For Si and Ge, a displacement energy of 15 eV was used, while for Au, an energy of 25 eV was assumed. For each case, the program was run until statistical fluctuations in the projected range and defect yield were less than 3%. This usually required histories of 100-300 ions per simulation.

TRIM has been shown to be very successful at matching experimental

---

[7]Copies of the TRIM-86 program are available from the authors

data for the projected range of implanted ions [23]. However, a word of caution about defect yield calculations is in order: there is not a definitive experimental technique to verify the defect yield/incident ion. Electron microscopy studies to measured the defect yield have been performed [26], but the results of such studies are almost always questionable. This is because thermal defect annealing causes an underestimation of the defect population, even at low temperatures. Nonetheless, it is assumed in this work that the TRIM calculations of defect generation produce reasonable results.

3.2 Results and Discussion

In this section, experimental results on ion beam enhanced grain growth are presented. Comparison is made in each case between the kinetics observed during IBEGG and isothermal furnace annealing. Normal grain growth during thermal annealing in Si and Au films has been previously investigated. However, data for normal grain growth for Ge in the regime of interest here did not exist, so thermal annealing experiments were conducted in Ge.

3.2.1   Germanium Thin Film Kinetics

Time Dependence for Thermal Annealing

The time dependence of grain growth to a columnar structure for an unencapsulated 500 Å thick amorphous-deposited film during thermal annealing at T = 775°C is shown in Fig. 3.10. The data indicate that the grain radius, r, is

$$r(t) \propto t^{0.28} \tag{3.1}$$

where t is time. This is consistent with the experimentally observed time dependence in metals[99,100] and ceramics[101,102], but is inconsistent with existing theories for normal grain growth[6,7,8]. More importantly, a comparison of the observed time dependence during thermal annealing and IBEGG is relevant to the problem of determining the mechanism for IBEGG, as will be seen shortly.

Temperature Dependence for Thermal Annealing

The temperature dependence of grain growth in a 500 Å thick film during the development of a columnar structure for thermal annealing is shown in Fig. 3.11. Data were taken between 750 - 815 °C. Below 750 °C, grain growth was not observable in a convenient time interval, and above 815 °C, beading of the film prevented observation of grain growth. The growth rate indicated is the growth rate at one-half of the final grain size. Thus the driving force due to grain boundary energy, which is proportional to the grain size, was assumed to be constant. Using a simple model for normal grain growth, the activation energy for grain growth is estimated
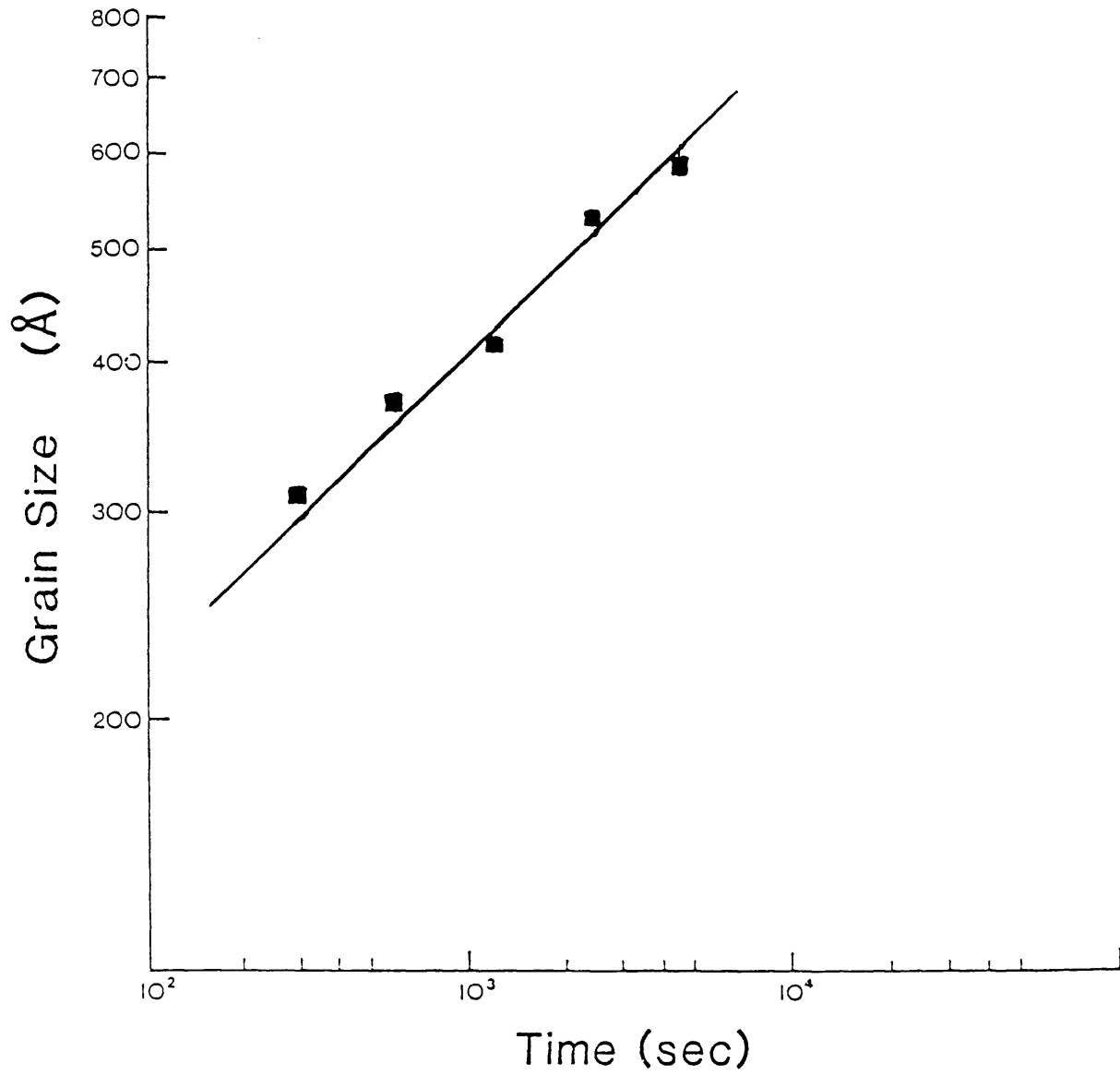
Figure 3.10: Time dependence of grain growth in amorphous-deposited Ge films for thermal annealing at 775 °C.

to be $E_a = 2.7 \pm 0.7$ eV. The uncertainty in this measurement is due to thermal grooving of the Ge film, which complicated grain size measurement. This measurement indicates that the activation energy for thermal grain boundary motion is between two-thirds of and approximately equal to the activation energy of self-diffusion, $E_{sd}(E_{sd} = 3.1$ eV [52]).

IBEGG Film Morphology

The electron micrographs of Fig. 3.12 illustrate the morphology of a free-standing Ge film which has undergone ion beam enhanced grain growth at 600 °C. A 50 keV Ge^+ beam was used, with a current density of 1.56 x 10^{12} ions/cm^2-sec. Figure 3.12(a) is an electron micrograph of a film implanted with an ion dose of 5 x 10^{13}/cm^2. The average grain size is approximately 100 Å and the microstructure is noncolumnar. Close inspection reveals a high density of dislocations within grains. Figure 3.12(b) is a similar micrograph of a film implanted with an ion dose of 5 x 10^{14}/cm^2, and Fig. 3.12(c) is a film implanted with an ion dose of 5 x 10^{15}/cm^2. The increase in grain size in Figs. 3.12(b) and 3.12(c) is apparent, and the change in morphology with increasing grain size is consistent with our understanding that normal grain growth is driven by a reduction in grain boundary energy. That is, as the grain size increases the grain boundary curvature is reduced. Boundary curvature normal to the plane of the film is eliminated as the film develops a columnar grain structure. The grain size distributions corresponding to the micrographs of Fig. 3.12 are shown in Fig. 3.13. These distributions, which are typical of Ge films undergoing thermal or
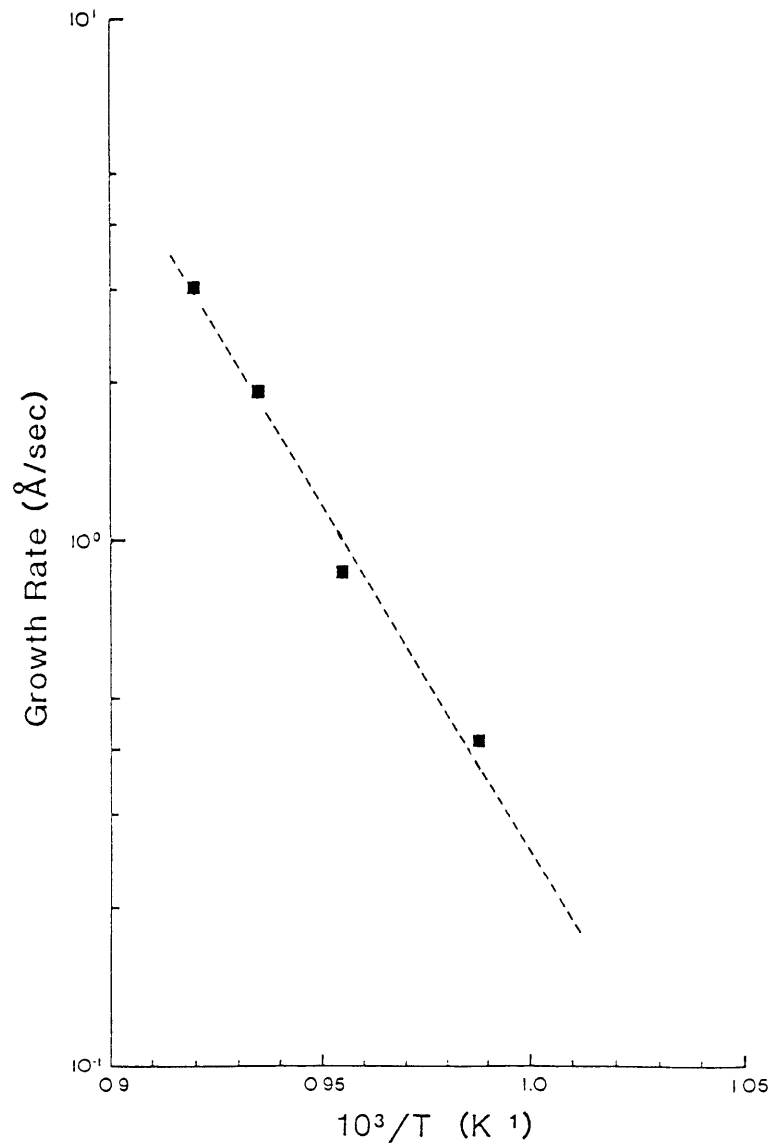
Figure 3.11: Temperature dependence of grain growth in Ge films during thermal annealing.

ion beam enhanced grain growth, are seen to be approximately lognormal in shape, which is also consistent with other investigations of normal grain growth[6]. The peak of the lognormal distribution moves to larger grain sizes with increasing ion dose.

Figure 3.14 illustrates the morphology and change in grain size of a freestanding Ge film which has undergone ion beam enhanced grain growth at 500 °C. As above, a 50 keV Ge^+ beam was used, with a current density of 1.56 x 10^{12} ions/cm^2-sec. The variation of grain size and microstructure is qualitatively very similar to that seen at 600 °C. The grain size increase and development of columnar structure is similar over the same range of ion doses. This suggests that ion beam enhanced grain growth is only very weakly temperature dependent.

Figure 3.15 shows cross-sectional electron micrographs of 500 Å thick Ge films on 1000 Å of thermally grown SiO_2 after IBEGG at 600 °C with a 50 keV Ge^+ beam at doses of 5 x 10^{13}/cm^2 and 5 x 10^{15}/cm^2. The micrograph in 3.15(a) confirms the noncolumnar microstructure of the film at the initial stages of normal grain growth. The micrograph in 3.15(b) indicates that the film has developed a columnar structure and that deep grooves exist in the film. These grooves certainly influence the driving force for growth and may be responsible for the slowing down of grain growth as the grain size approaches the film thickness[9]. This issue is discussed in the model for ion beam enhanced grain growth.

Also notable is the observation that the density of dislocations within grains is dramatically reduced as the ion dose increases. Figure 3.16 is a high-resolution electron micrograph of the film shown at lower magnifica-

tion in Fig. 3.12(c). The micrograph illustrates the 3.2 Å lattice fringes which correspond to satisfaction of a two-beam condition for (111) planes in Ge. The Moiré interference fringes which cross the lattice fringes indicate a low angle grain boundary viewed at near normal incidence. Visible also are lattice fringes in the adjacent grain. The absence of dislocations is an indication of a high degree of crystalline perfection within grains.

IBEGG Time Dependence

The dependence of grain size on ion dose for a variety of Ge films deposited in amorphous and polycrystalline form is shown in Fig. 3.17. Results are shown for both unsupported films and films on thermal SiO_2 substrates. The change of grain size with ion dose, $(d - d_o)$, is similar for all substrates and deposition conditions, suggesting that the basic mechanism of IBEGG is invariant in these various experiments. The time dependence varies from $r(t) \propto t^{0.25}$ for the polycrystalline as-deposited films to $r(t) \propto t^{0.31}$ for amorphous as-deposited freestanding films. These growth exponents fall within the range of experimentally observed growth exponents in other systems[99,100,101,102]. The difference in growth exponents may be related to the microstructural differences in the various films. For example, the as-deposited polycrystalline films, which have the smallest growth exponent, presumably have a smaller driving force than the as-deposited amorphous films, owing to their approximately columnar microstructure before grain growth(see Fig. 3.4). The greatly reduced grain boundary curvature normal to the plane of the film results in a lower driving force at
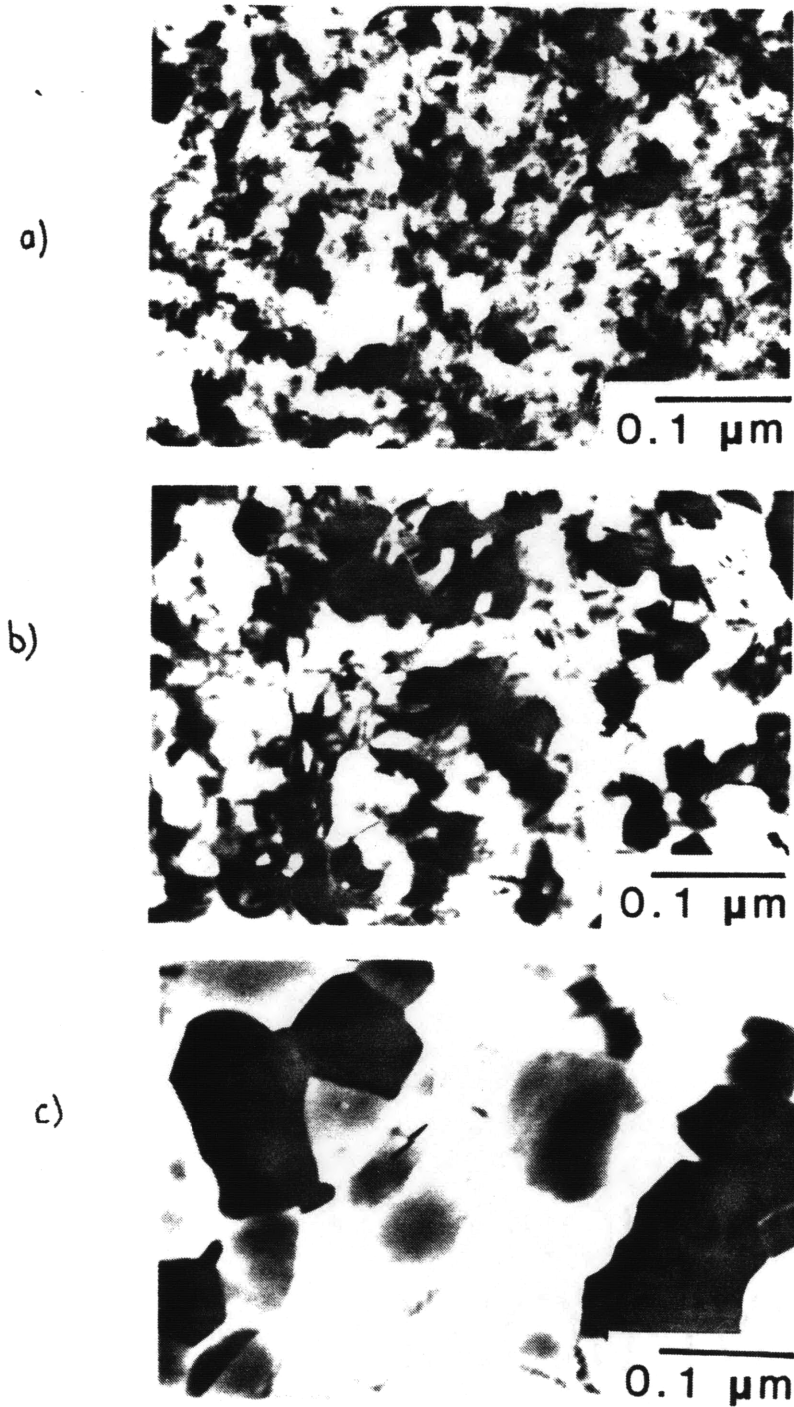
Figure 3.12: Transmission electron micrographs of a freestanding 500 Å thick Ge film at 600 °C implanted with 50 keV Ge$^+$ at a dose of (a) 5 x 10^{13}/cm^2 (b) 5 x 10^{14}/cm^2 (c) 5 x 10^{15}/cm^2.
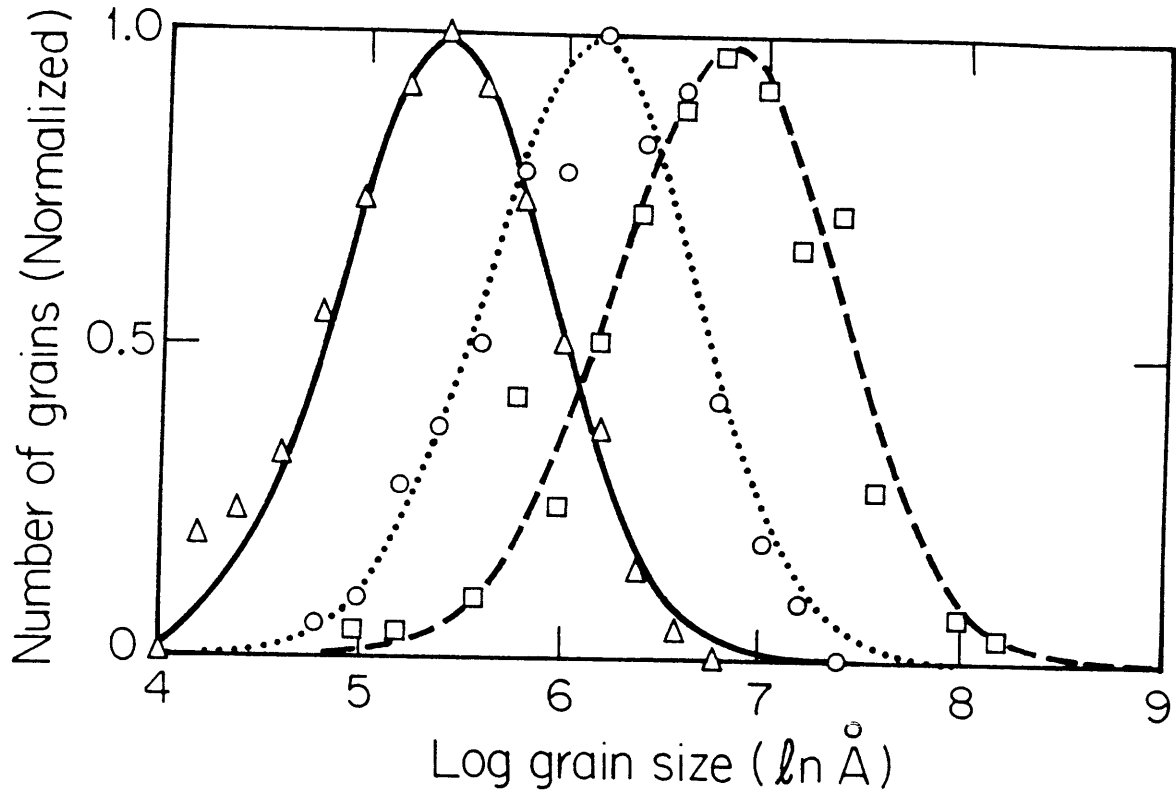
Figure 3.13: Lognormal grain size distributions for IBEGG with 50 keV Ge^+ at doses of $5 \times 10^{13}/cm^2$, $5 \times 10^{14}/cm^2$ and $5 \times 10^{15}/cm^2$.
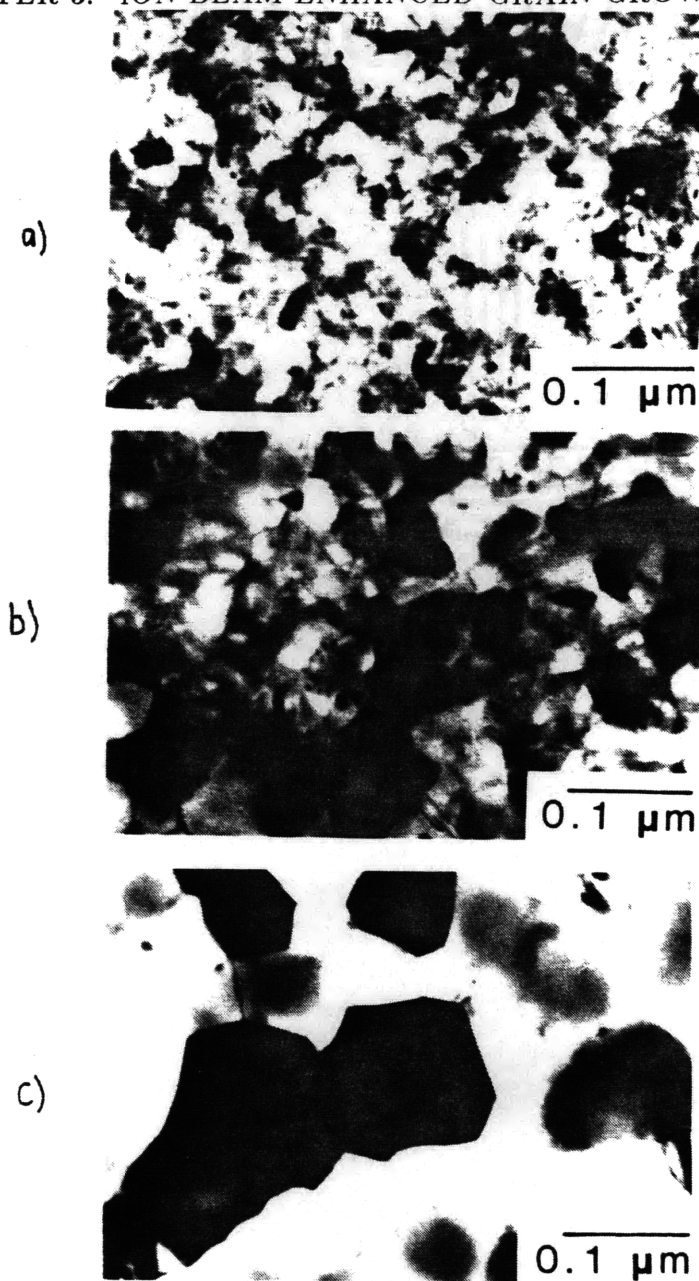
Figure 3.14: Transmission electron micrographs of a freestanding 500 Å thick Ge film at 500 °C implanted with 50 keV Ge$^+$ at a dose of (a) 5 x 10^{13}/cm^2 (b) 5 x 10^{14}/cm^2 (c) 5 x 10^{15}/cm^2.
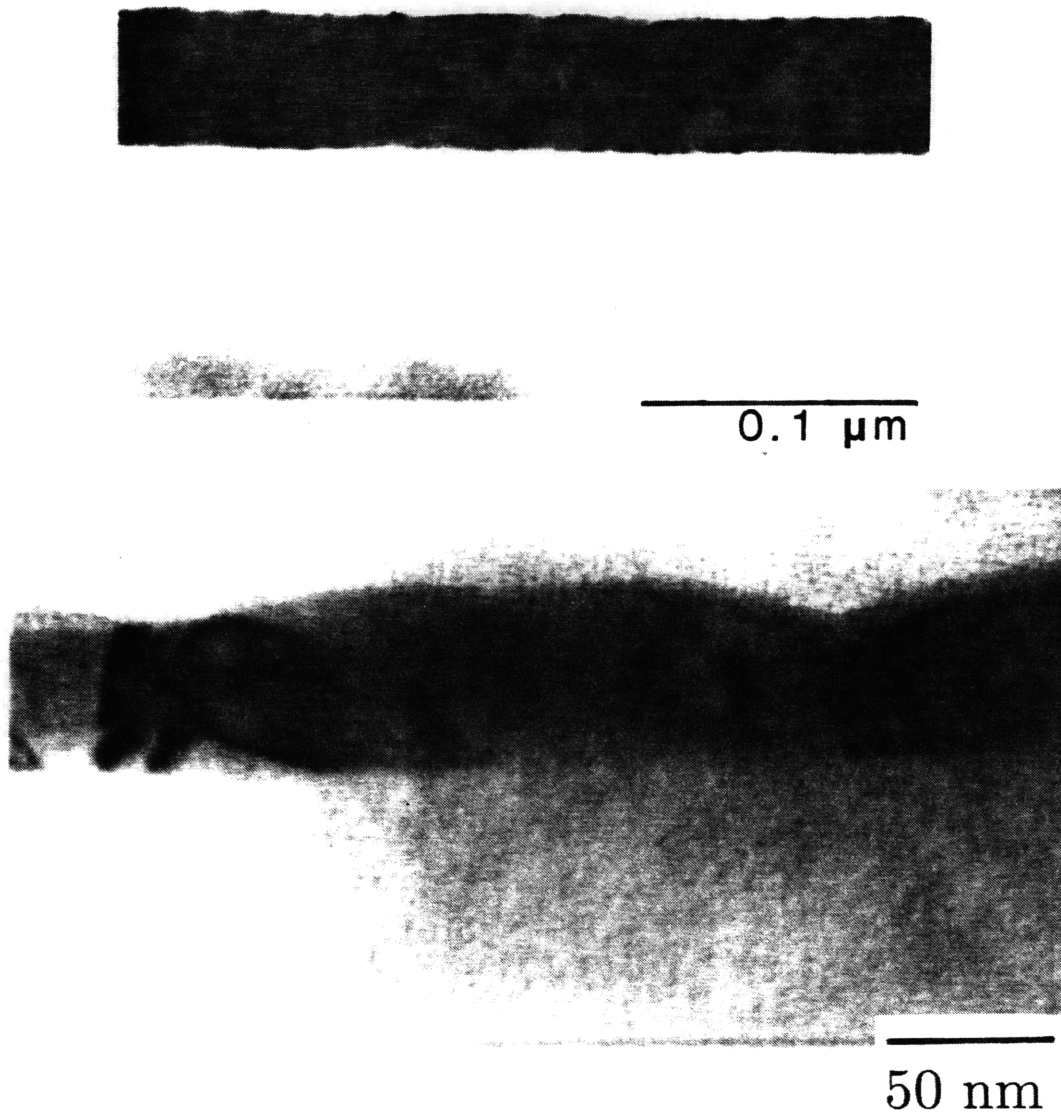
Figure 3.15: Cross-sectional electron micrograph of 500 Å thick Ge film after IBEGG at 600 °C with a 50 keV Ge$^+$ beam at a dose of (a) 5 x 10^{13}/cm^2 and (b) 5 x 10^{15}/cm^2. Note the grain boundary grooves in (b).

60 Å
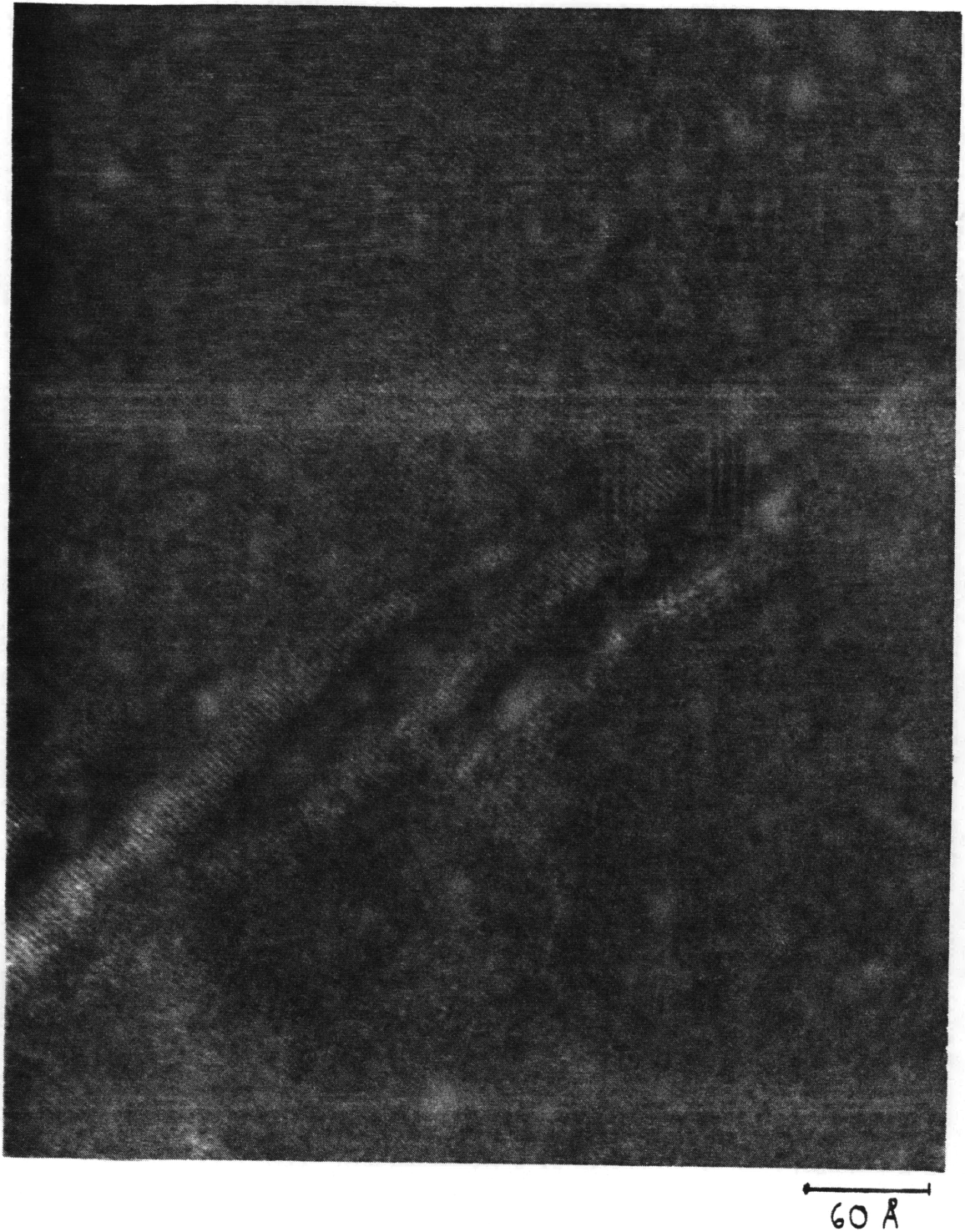
Figure 3.16: High resolution electron micrograph of a 500 Å thick Ge film implanted with 50 keV Ge$^+$ at a dose of 5 x 10^{15}/cm^2. Visible are the 3.2 Å (111) lattice fringes and a grain boundary which crosses the micrograph.

a given grain size.

In general, the variation of IBEGG with time is similar to the observed time dependence of thermal grain growth, which may indicate that kinetic processes which occur at grain boundaries are rate-limiting in both cases. An argument for this assertion is made in the section on the model for IBEGG.

IBEGG Temperature Dependence

The temperature dependence of grain growth in 500 Å thick amorphous as-deposited Ge films which have undergone ion beam enhanced grain growth during bombardment with 50 keV Ge$^+$ between 450 °C and 700 °C is shown in Fig. 3.18. This to be is compared with the temperature dependence of a similar, thermally annealed film. As previously mentioned, the thermal data indicate an activation energy for grain boundary motion of approximately 2.7 eV. Unlike thermal annealing, IBEGG is characterized by a very weak temperature dependence. The measured activation energy of 0.15 eV for the IBEGG process is lower than measured energies for point defect migration in Ge [52]. This suggests that thermal migration of defects generated within grains are not responsible for grain growth. Therefore, based on the observed time and temperature dependence of IBEGG, we propose that Frenkel defects created at or very near grain boundaries are responsible for the observed grain boundary mobility enhancement.

Various 500 Å Ge Films		
Symbol	T (C)	Film Config.
●	600	Poly-dep, /SiO₂
○	500	Poly-dep, /SiO₂
△	600	Am-dep, /SiO₂
■	500	Am-dep, /SiO₂
▲	600	Am-dep, Free
□	500	Am-dep, Free
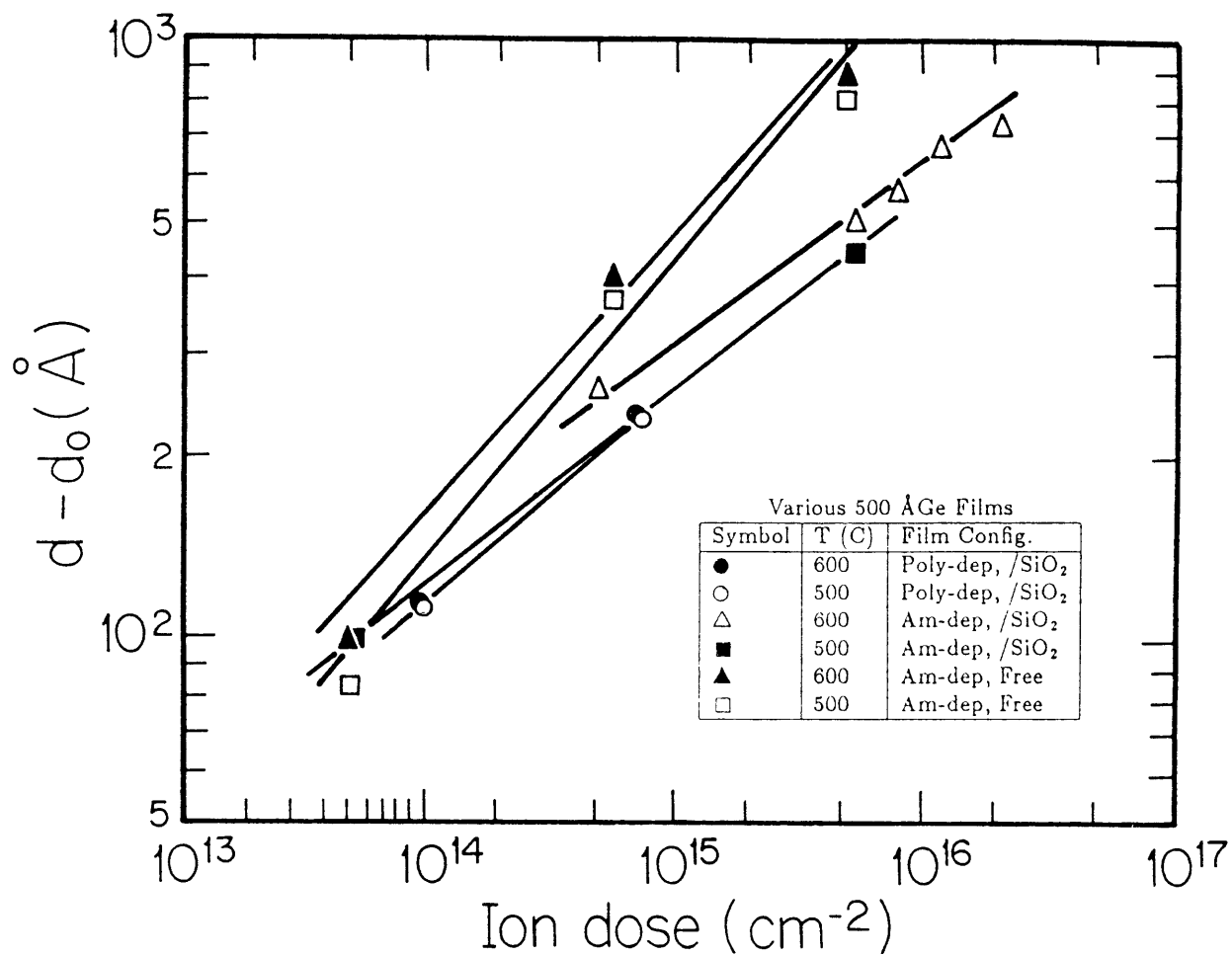
Figure 3.17: Variation of grain size with ion dose for various 500 Å Ge films bombarded by 50 keV Ge^+. Films were either polycrystalline as-deposited or amorphous as-deposited, and were either unsupported or on SiO_2 substrates.
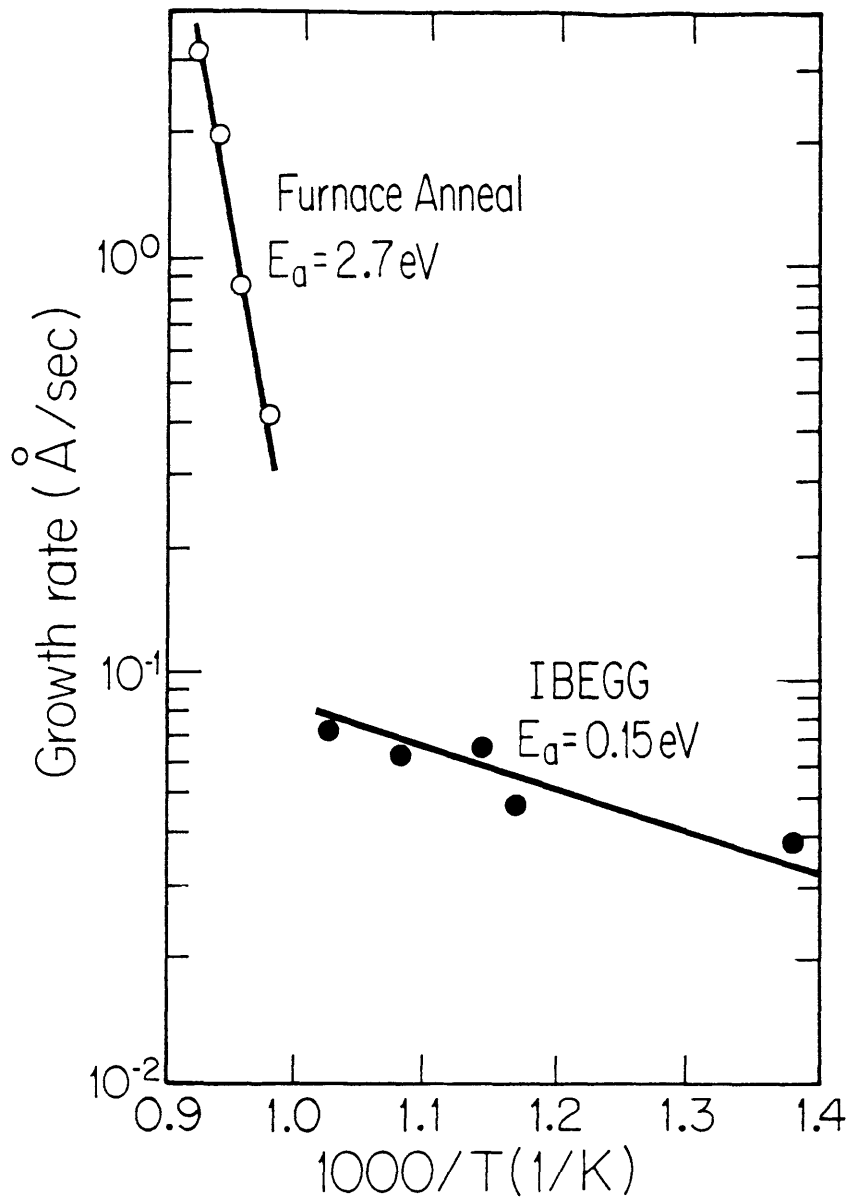
Figure 3.18: Arrhenius plot of growth rate of Ge for thermal annealing and ion beam enhanced grain growth at a constant flux of 1.5 x 10^{12}ions/cm^2-sec.

Ion Mass Dependence

Ion beam enhanced grain growth in Ge has also been studied using various projectile ion species. Figure 3.19 depicts the variation of grain size with ion dose for 50 keV Ar^+, 50 keV Kr^+, 50 keV Ge^+, and 100 keV Xe^+ incident on 500 Å amorphous as-deposited Ge films at 600 °C. Similar grain growth behavior is exhibited for all projectile ions. However, the grain size for a given ion dose increases with increasing projectile ion mass. Figure 3.20 depicts the variation of grain size in amorphous as-deposited Ge films at 600 °C with incident ion mass, at a constant dose of 5 x $10^{15}/cm^2$. Also shown is the number of vacancy-interstitial pairs per incident ion at the given energy calculated using the TRIM code. A close correlation is seen between the number of vacancy-interstitial pairs produced per incident ion and the increase in grain size. This result suggests that the defects responsible for IBEGG can be described using linear collision cascade theory.

High Doses - Secondary Grain Growth

A key question in the present research is whether ion bombardment promotes surface energy driven secondary grain growth (SEDSGG) as well as normal grain growth in thin films. If the sole effect of ion bombardment is to enhance the mobility of grain boundaries, then secondary grain growth is assumed to be possible during IBEGG. However, if the IBEGG process alters the driving force due to surface energy, or enhances other kinetic processes, such as enhanced grooving and beading, then the possibility of SEDSGG may be questionable.
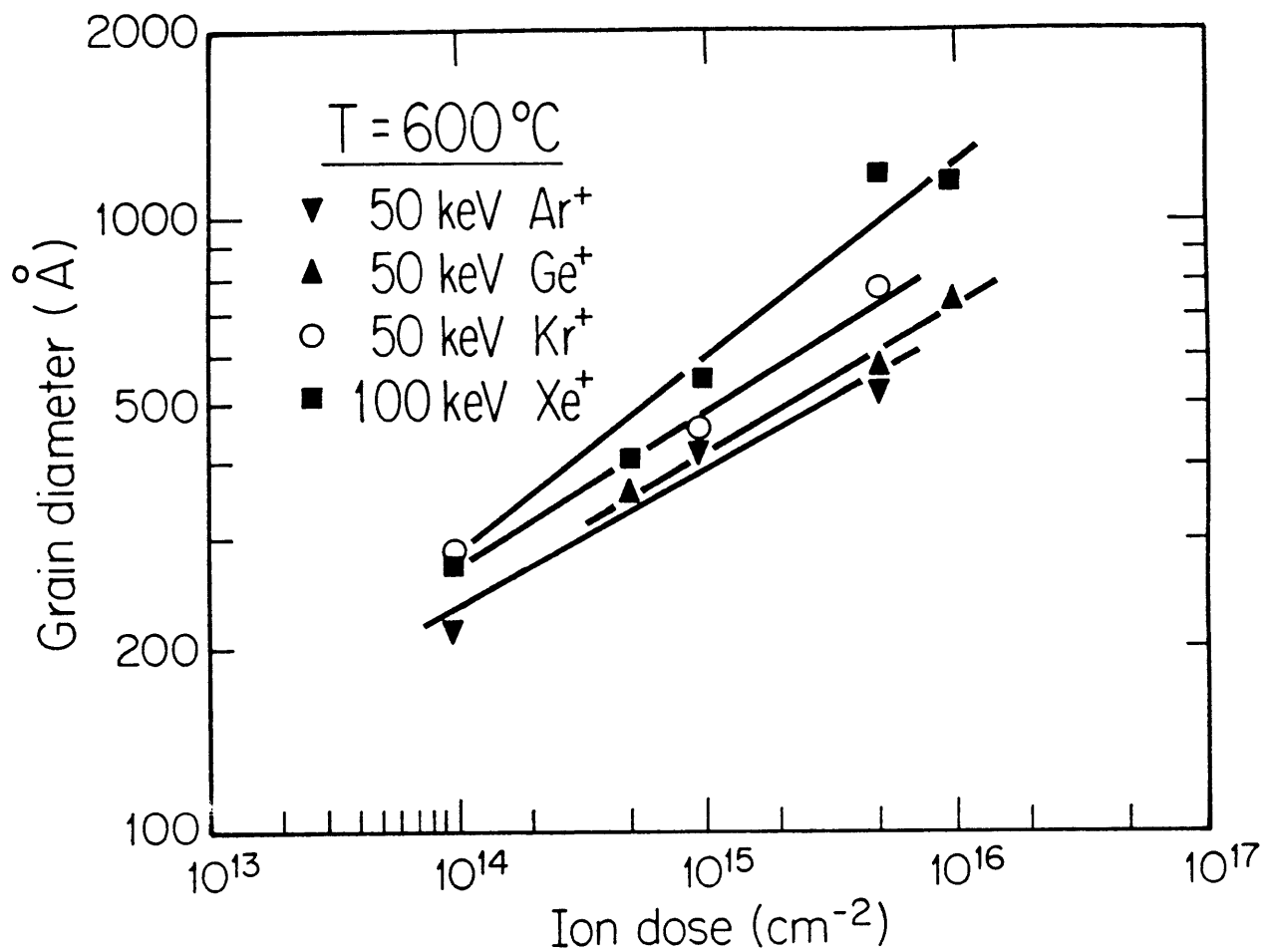
Figure 3.19: Variation of grain size with ion dose for 500 Å thick Ge films on SiO_2 implanted with Ar^+, Ge^+, Kr^+, and Xe^+ ions, all at 600 °C.
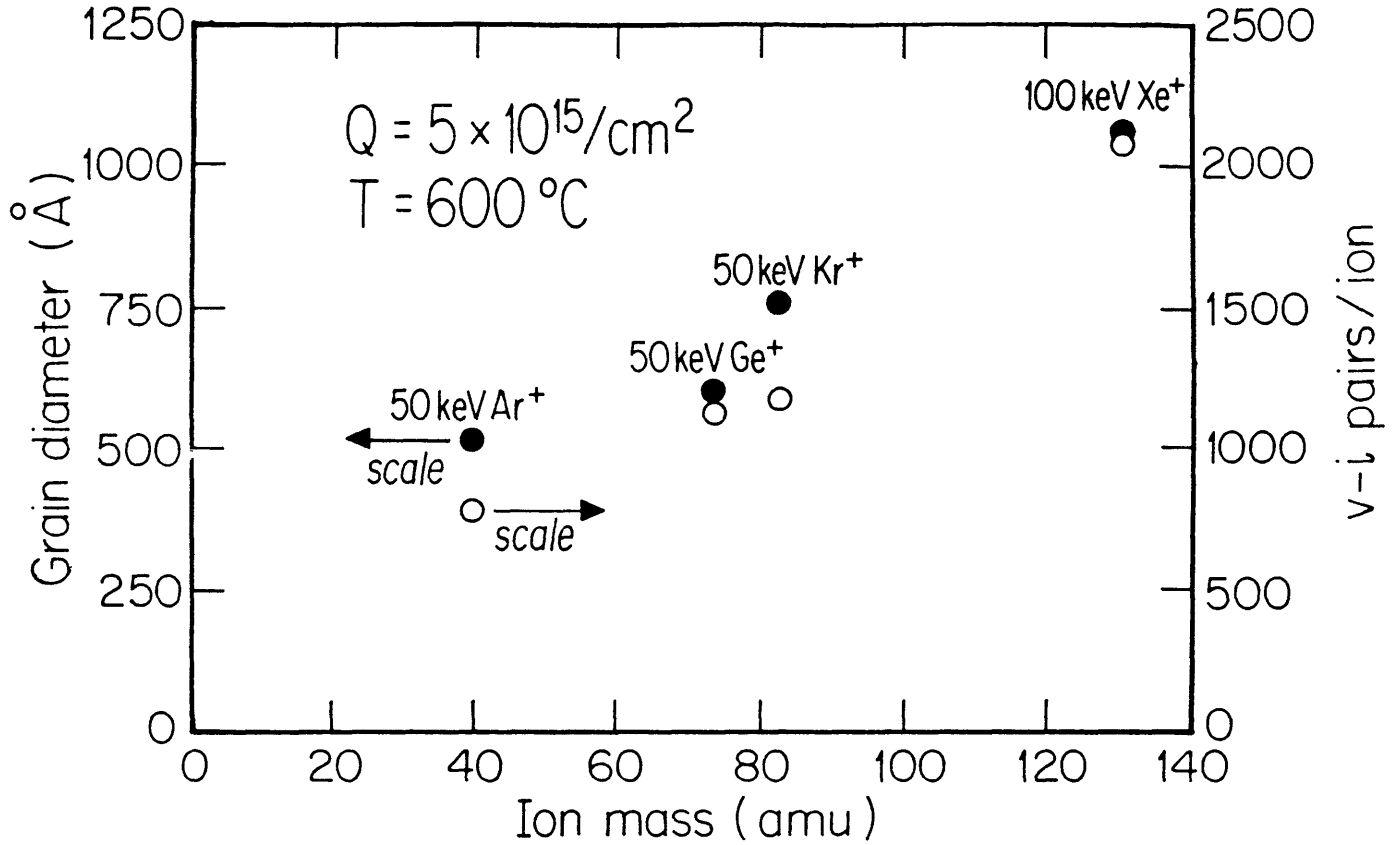
Figure 3.20: Comparison of grain size and the number of defects generated per incident ion with projectile ion mass at 600 °C. The ion dose was 5 x $10^{15}/cm^2$ for all cases.

Previous work on grain growth in Ge has included an extensive investigation of secondary grain growth in thin Ge films[13]. In that work, high temperature thermal anneals were used so that the grain boundary mobility was sufficient to observe grain growth. Also, the films were encapsulated with SiO_2 to avoid beading of the thin film. Thin (300 Å in most cases) films were employed so that the driving force due to surface energy was high enough to permit secondary grain growth. However, unambiguous indications of *surface energy driven* secondary grain growth, such as existence of a uniform crystallographic texture, were lacking.

In the previous work[13], it was found that secondary grain growth only occurred after the development of a columnar normal grain microstructure. The present work has concentrated on normal grain growth, because the range of experimentally accessible ion doses generally promoted normal grain growth. Very high ion doses (i. e. , $\geq 10^{16}/cm^2$) resulted in qualitative indications of secondary growth, as illustrated in Fig. 3.21. The fraction of secondary grains in this film is too small ($< 1\%$) to permit quantitative characterization via the fraction-transformed formalism[98].

Lateral Crystallization during Ion Bombardment

While the majority of the work reported in this thesis concerns the growth of a polycrystalline film during ion bombardment, experiments have also been conducted in which an amorphous film undergoing crystallization was subjected to ion bombardment. The micrograph of Fig. 3.22 is a 500 Å Ge film which has been bombarded by a 50 keV Ge^+ beam with an ion flux

Figure 3.21: Transmission electron micrograph of a secondary grain in a 500 Å Ge film implanted with 50 keV Ge^+ at a dose of 1×10^{16} at 600 °C.

density of 1.5 x $10^{12}/cm^2$ while being heated to 500 °C. The ion beam was turned on at room temperature and implantation continued until a dose of 5 x $10^{15}/cm^2$ was reached. The stage was heated from room temperature to 500 °C in approximately 15 minutes, and the rate of heating was approximately constant. Presumably, at some point during the heating of the film, copious crystallization occurred, since large, branched crystalline regions are observed which are surrounded by amorphous regions. Approximately one half of the film had been crystallized. This morphology is to be compared with the morphology of a 500 Å film which has undergone crystallization during thermal annealing, such as shown in Fig. 3.23. The morphology of Fig. 3.22 and the size of the crystalline regions are consistent with the assumption that the ratio of the lateral crystallization rate to the nucleation rate was increased above the thermal value during IBEGG.

3.2.2 Gold Thin Film Kinetics

IBEGG Film Morpholgy

The morphology of Au films which have undegone IBEGG is shown in Figs. 3.24 and 3.25, for 250 Å and 500 Å films respectively. A 200 keV Xe^+ beam with a current density of 1.5 x $10^{13}/cm^2$-sec was employed, and the substrate temperature was room temperature (23 °C). The 250 Å unimplanted film is characterized by a noncolumnar grain structure with grain sizes smaller than the film thickness. A dose of 5 x $10^{13}/cm^2$ caused a columnar grain structure to develop, as seen in Fig. 3.24b). Higher doses
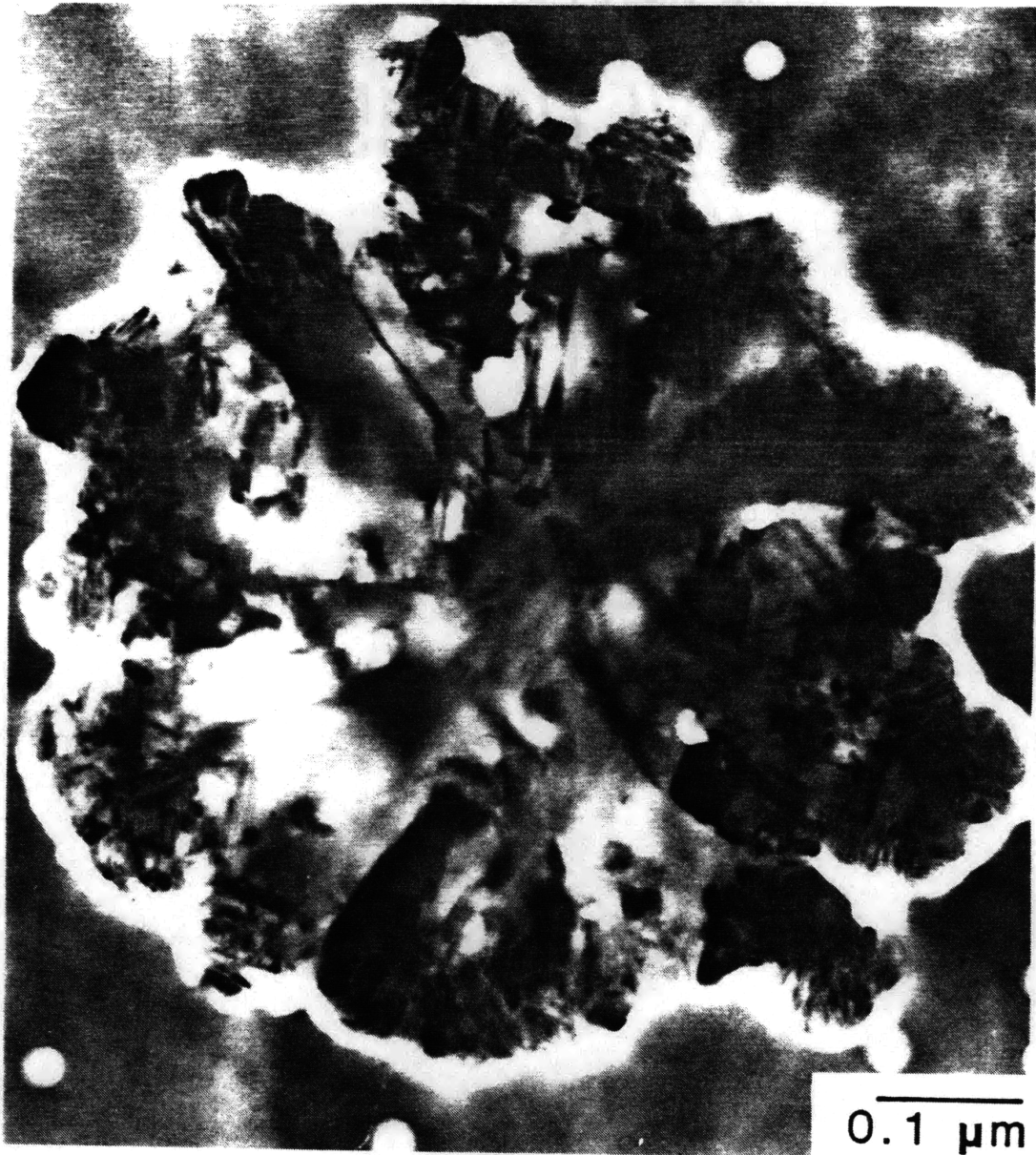
Figure 3.22: Transmission electron micrograph of 500 Å Ge film which has undergone crystallization during IBEGG at 500 °C. The ion current density was $1.5 \times 10^{12}/cm^2$.
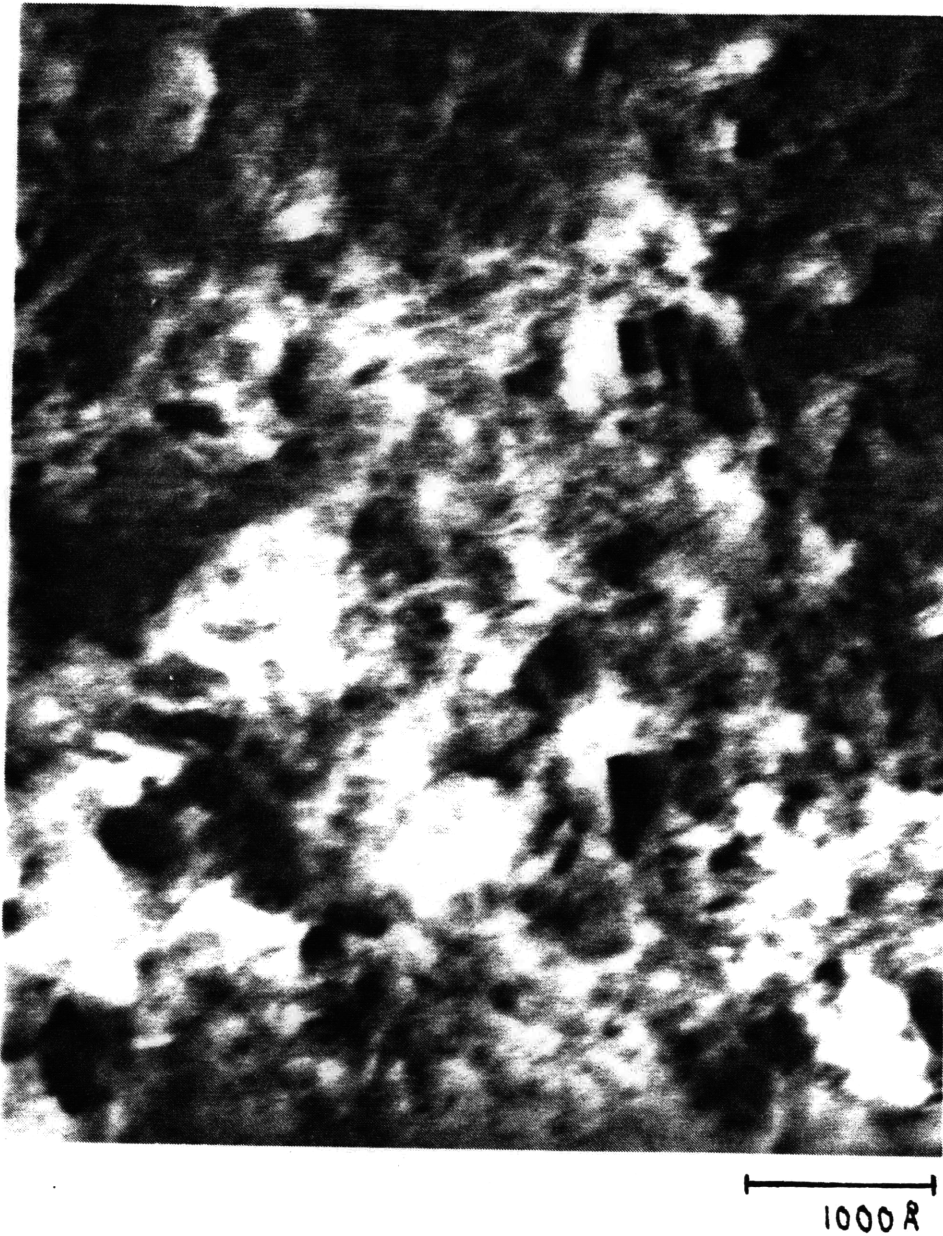
Figure 3.23: Transmission electron micrograph of an amorphous as-deposited 500 ÅGe film which has been thermally annealed at 500 °C for 60 minutes.

(Fig. 3.24c) and d)) result in further grain growth. However, unlike Ge, the density of defects within grains increases with increasing ion dose.

Energy dispersive X-ray analysis in the scanning transmission electron microscope (STEM) did not detect any impurity-related defects in the films. Dark field electron micrscopy indicated that the defects exhibited diffraction contrast when the film was tilted in the microscope. This observation lends support to the idea that the defects are dislocations [104] rather than bubbles of entrapped gas in the film. The observation of dislocations in ion bombarded Au films reported previously are consistent with this interpretation[26]. The 500 Å films exhibit a similar change in morphology as a result of IBEGG. The microstructure of the unimplanted 500 Å film is characterized by small non-columnar grains and a small population of abnormal, or secondary grains.

Secondary or Normal Grain Growth

An important question to consider in the study of IBEGG in gold films is whether the process is one of secondary grain growth or normal grain growth. Surface energy driven secondary grain growth is characterized by evolution of a bimodal grain size distribution and the development of a strong crystallographic texture. Both of these attributes have been found in grain growth in thin Au films which have undergone thermal grain growth at room temperature[16].

The grain size distributions shown in Fig. 3.26 are for a 250 Å Au film during IBEGG. These distributions are for grain growth under the conditions described in the previous section and correspond to the electron
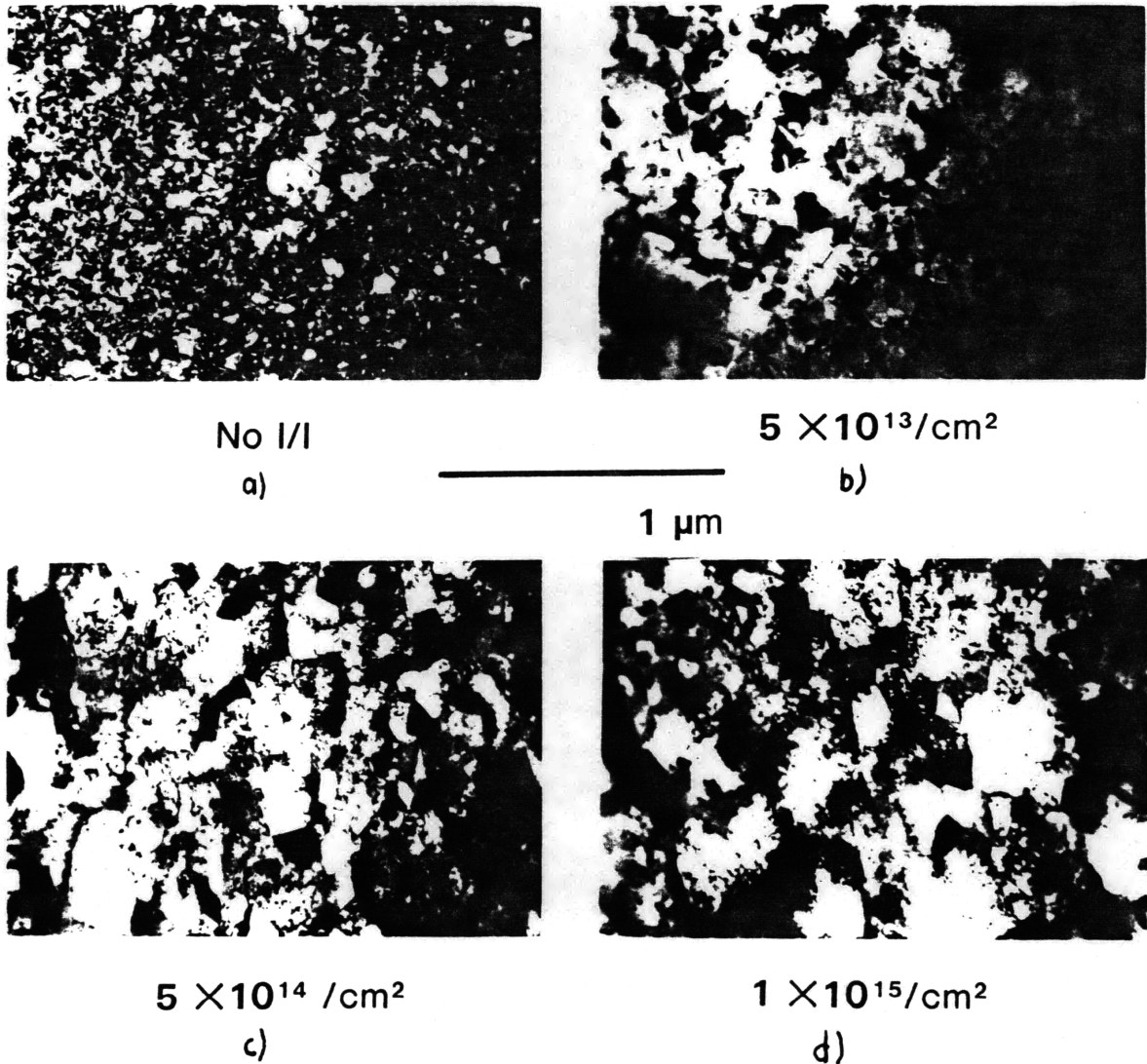
Figure 3.24: Transmission electron micrographs of a 250 Å Au film after IBEGG with a 200 keV Xe^+ beam, with an ion flux density of 1.5 x $10^{13}/cm^2$-sec. In (a), no implant, (b) 5 x $10^{13}/cm^2$, (c) 5 x $10^{14}/cm^2$, (d) 1 x $10^{15}/cm^2$.
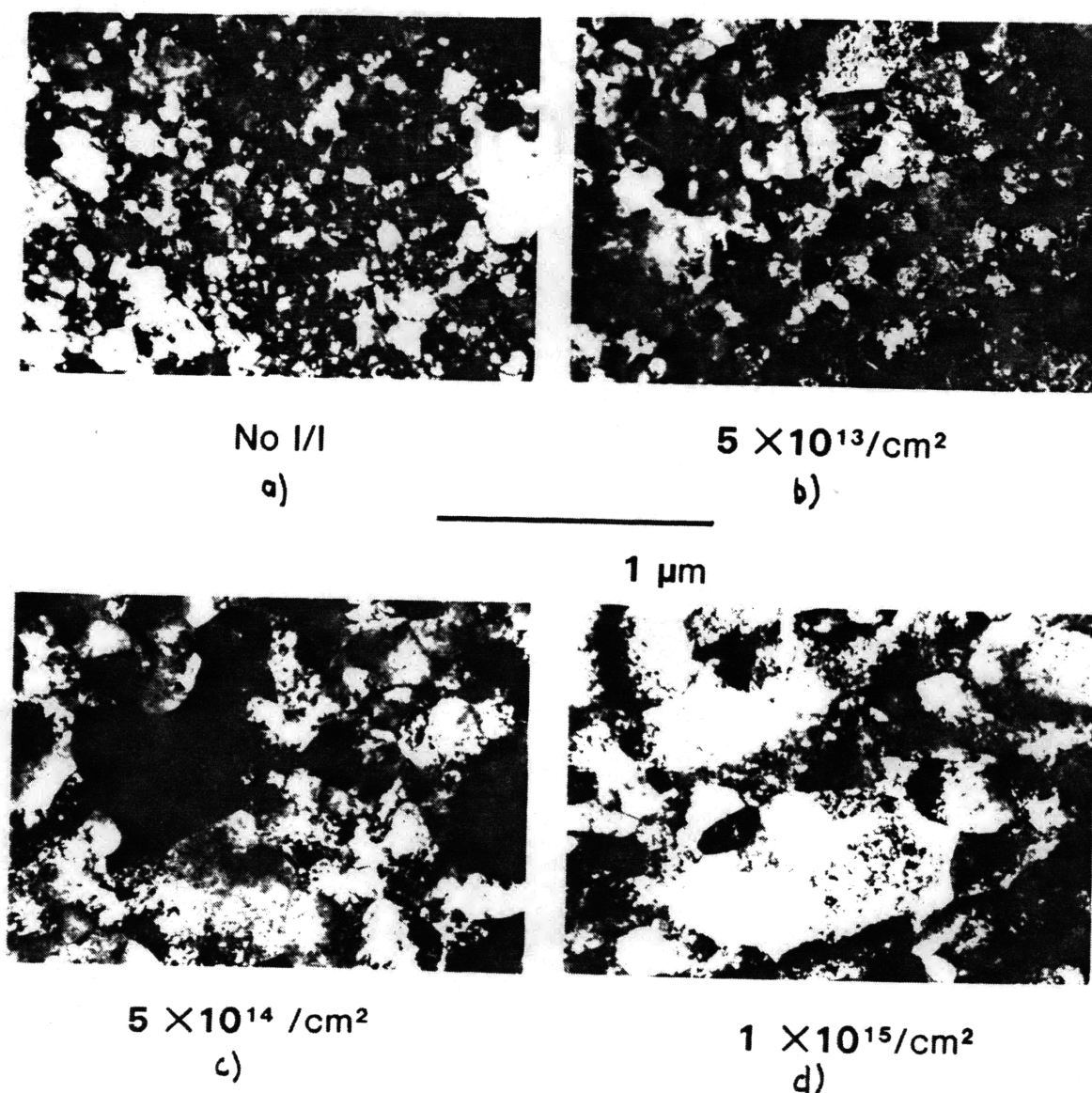
Figure 3.25: Transmission electron micrographs of a 500 Å Au film after IBEGG with a 200 keV Xe^+ beam, with an ion flux density of 1.5 x $10^{13}/cm^2$-sec. In (a), no implant, (b) 5 x $10^{13}/cm^2$, (c) 5 x $10^{14}/cm^2$, (d) 1 x $10^{15}/cm^2$.

micrographs of Fig. 3.24. The distributions are monomodal and approximately lognormal, and during IBEGG the peak of the distributions move to larger grain sizes. The monomodal character of the distributions tends to support a view of IBEGG in 250 Å Au films as being a normal grain growth process. However, it is an unusual normal grain growth process, since the grain size is apparently not limited by the specimen-thickness effect.

Figure 3.27 depicts grain size distributions for 500 Å thick Au films during IBEGG. The micrograph of Fig. 3.25(a) indicates that the film contains secondary grains, but the population of secondary grains is too small to be noticeable in the grain size distributions. These distributions are also monomodal and lognormal, and, as with 250 Å films, the peak of the distributions move to larger grain sizes. Also similar to the 250 Å films, the grain size is not limited by the thickness of the film.

Although the monomodality of the grain size distributions is consistent with normal grain growth, the change of crystallographic texture as a result of IBEGG may indicate that surface energy plays a role in grain growth. The electron diffraction patterns for 250 Å films are shown in Fig. 3.28. Before IBEGG, all diffraction rings allowed by the fcc structure are present. After IBEGG, The {200}, {222} and {111} rings are greatly reduced in intensity. The {220} ring, corresponding to (111) texture, is stronger. Figure 3.29 shows a similar change in diffracted intensity for 500 Å Au films. The development of a strong (111) texture has been reported for thermal anneals of Au films[16]. During IBEGG, (111) texture is preferred, but not as strongly as is the case for thermal annealing. This finding may indicate that IBEGG modifies the driving force for grain growth due to surface
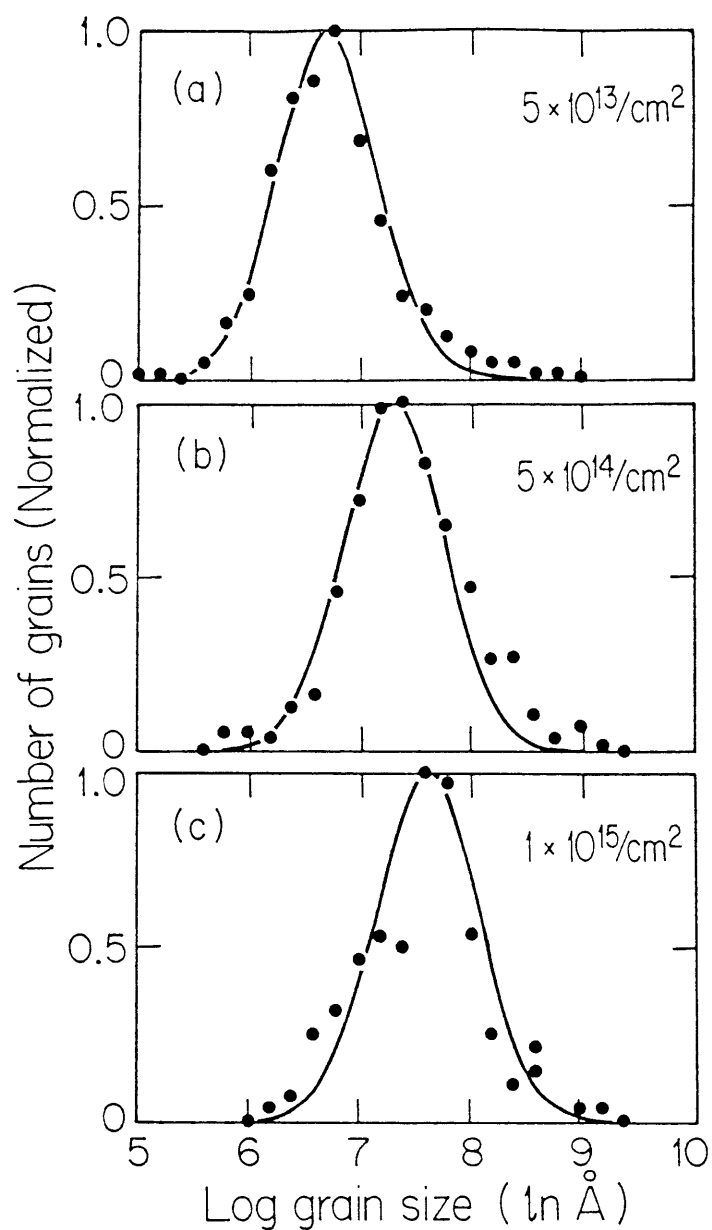
Figure 3.26: Grain size distributions for a 250 Å Au film after IBEGG with a 200 keV Xe^+ beam, with an ion flux density of 1.5 x 10^{13}/cm²-sec. In (a), 5 x 10^{13}/cm², (b) 5 x 10^{14}/cm². (c) 1 x 10^{15}/cm².
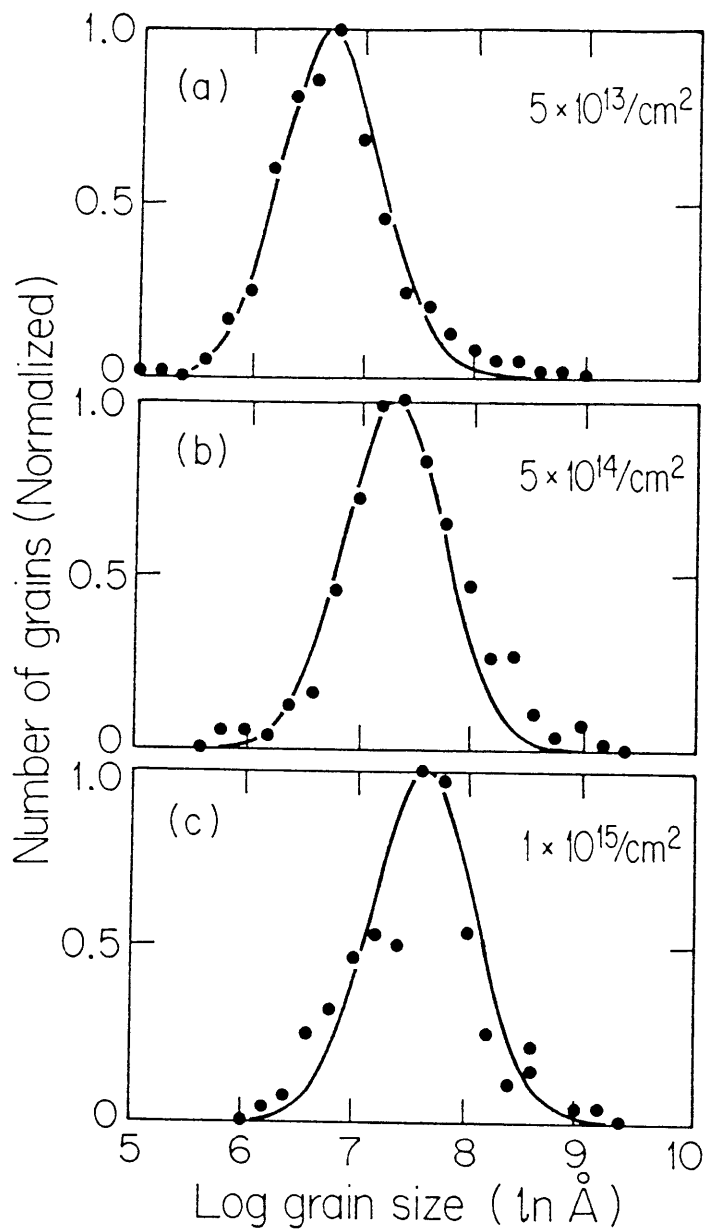
Figure 3.27: Grain size distributions for a 500 Å Au film after IBEGG with a 200 keV Xe^+ beam, with an ion flux density of 1.5 x $10^{13}/cm^2$-sec. In (a) 5 x $10^{13}/cm^2$, (b) 5 x $10^{14}/cm^2$, (c) 1 x $10^{15}/cm^2$.

energy. This is a reasonable assumption, since some sputtering accompanies implantation. Sputtering may alter the structure of the free surface, thereby modifying the surface energy.

Taken together, the observations about the grain size distributions and crystallographic texture in Au films during IBEGG point to a grain growth process in which *both grain boundary energy and surface energy play a role.* The observed monomodal grain size distributions may imply that surface energy is not the predominant driving force, however, the change in crystallographic texture indicates that it is not negligible either.

IBEGG Time Dependence

The time dependence for IBEGG in thin Au films bombarded by 200 keV Xe^+ is shown in Fig. 3.30. Grain size increases with ion dose for both 250 Å and 500 Å films. The time dependence is given by

$$r(t) \propto t^{0.3} \qquad (3.2)$$

for both 250 Å and 500 Å films. This is consistent with the results for Ge and other investigations of normal grain growth.

Ion Flux Dependence

An important consideration in the characterization of IBEGG is to assess the role of heating of the film by the ion beam. If heating of the film by the ion beam leads to grain growth by a spurious thermal anneal, the effect should be detectable by monitoring grain growth for different ion fluxes. Figure 3.31 illustrates the time dependence of grain growth during 200

a)   b)
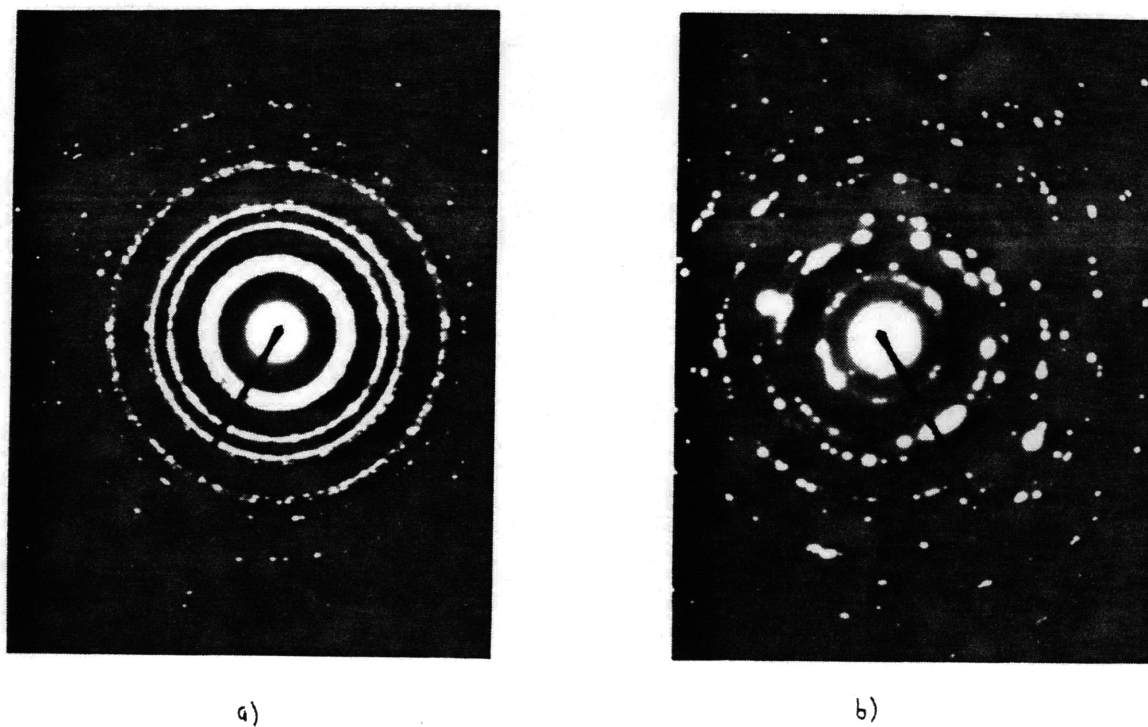
Figure 3.28: Transmission electron diffraction patterns for a 250 Å Au film after IBEGG with a 200 keV Xe^+ beam, with an ion flux density of 1.5 x $10^{13}/cm^2$-sec. In (a), no implant, (b) 1 x $10^{15}/cm^2$.

a)   b)
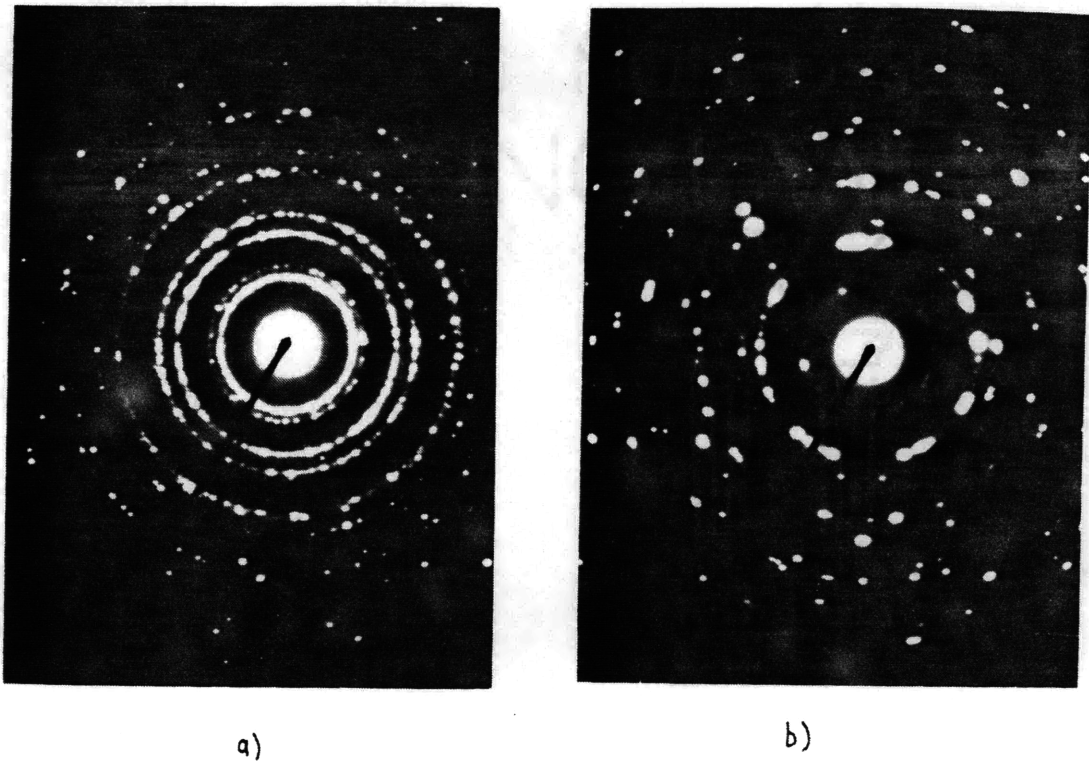
Figure 3.29: Transmission electron diffraction patterns for a 500 Å Au film after IBEGG with a 200 keV Xe^+ beam, with an ion flux density of 1.5 x $10^{13}/cm^2$-sec. In (a), no implant, (b) 5 x $10^{14}/cm^2$.
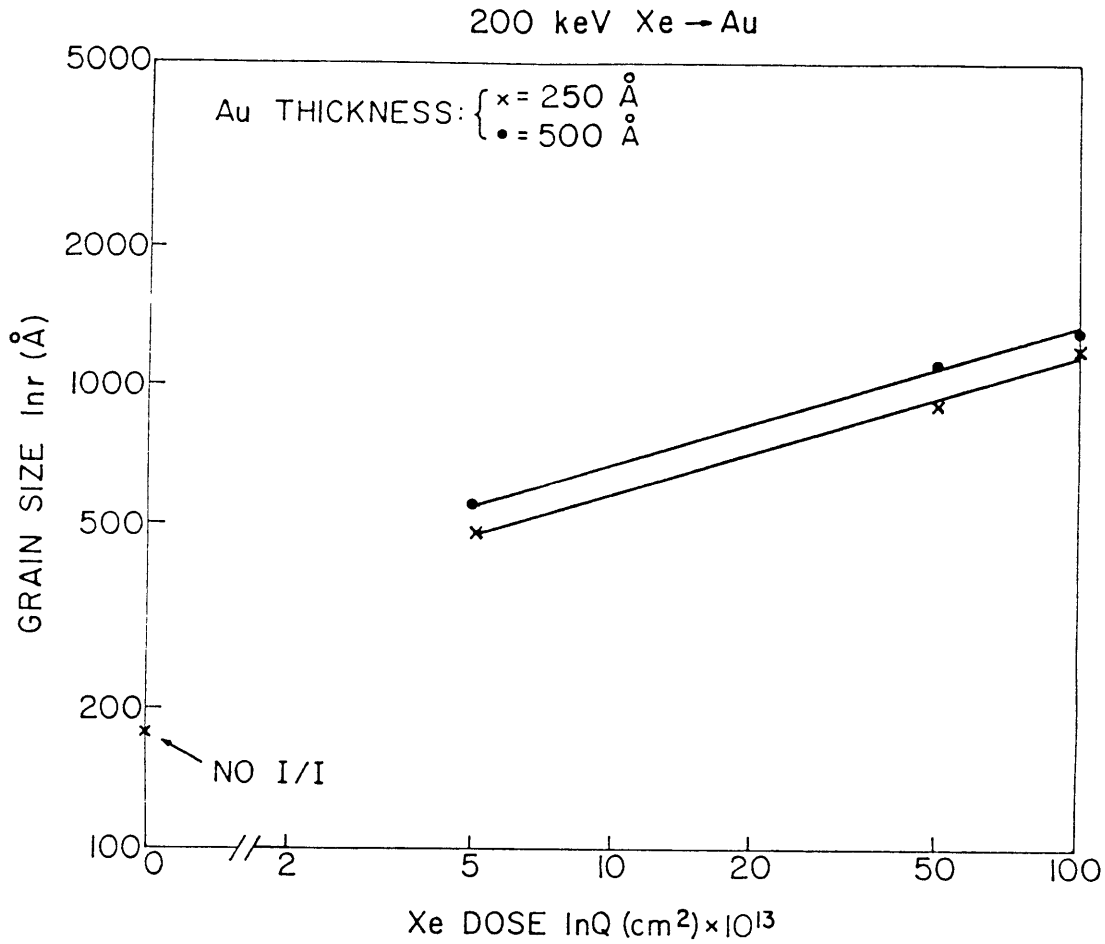
Figure 3.30: Variation of grain size with ion dose in Au films bombarded by 200 keV Xe$^+$ with an ion flux density of 1.5 x 10^{12}/cm^2-sec at 23 °.

keV Xe$^+$ bombardment for two different ion fluxes, 1.5 x 10^{12}ions/cm^2-sec and 1.5 x 10^{13}ions/cm^2-sec. The data indicates that increasing the ion flux by a factor of 10 simply increases the growth rate by a factor of 10 Said another way: the grain size is a function of the ion dose, not the ion flux. This finding is consistent with a view of IBEGG in which thermal annealing of the film is negligible.

Another test for the possibility of ion beam heating was developed. By masking part of the film from the beam, as shown in Fig. 3.32(a), contiguous regions which were either bombarded or not bombarded could be studied. If ion beam heating were to influence grain growth in the bombarded region, presumably the unbombarded region would also experience growth due to heating by conduction. The transmission electron micrograph of Fig. 3.32(b) illustrates the border between a bombarded and an unbombarded region in a 500 Å thick Au film bombarded by 1 x 10^{15}/cm^2 of 200 keV Xe$^+$ with a flux of 1.5 x 10^{13}/cm^2-sec. Small noncolumnar grains are seen in the unbombarded region, and larger grains are seen in the bombardment region. The demarcation between the two regions corresponds approximately to the lateral straggle of the ion beam. This result supports a model of grain growth in which only those regions which experience elastic collisions undergo grain growth. The lack of grain growth in the unbombarded region is interpreted as evidence for a lack of ion beam heating of this area.
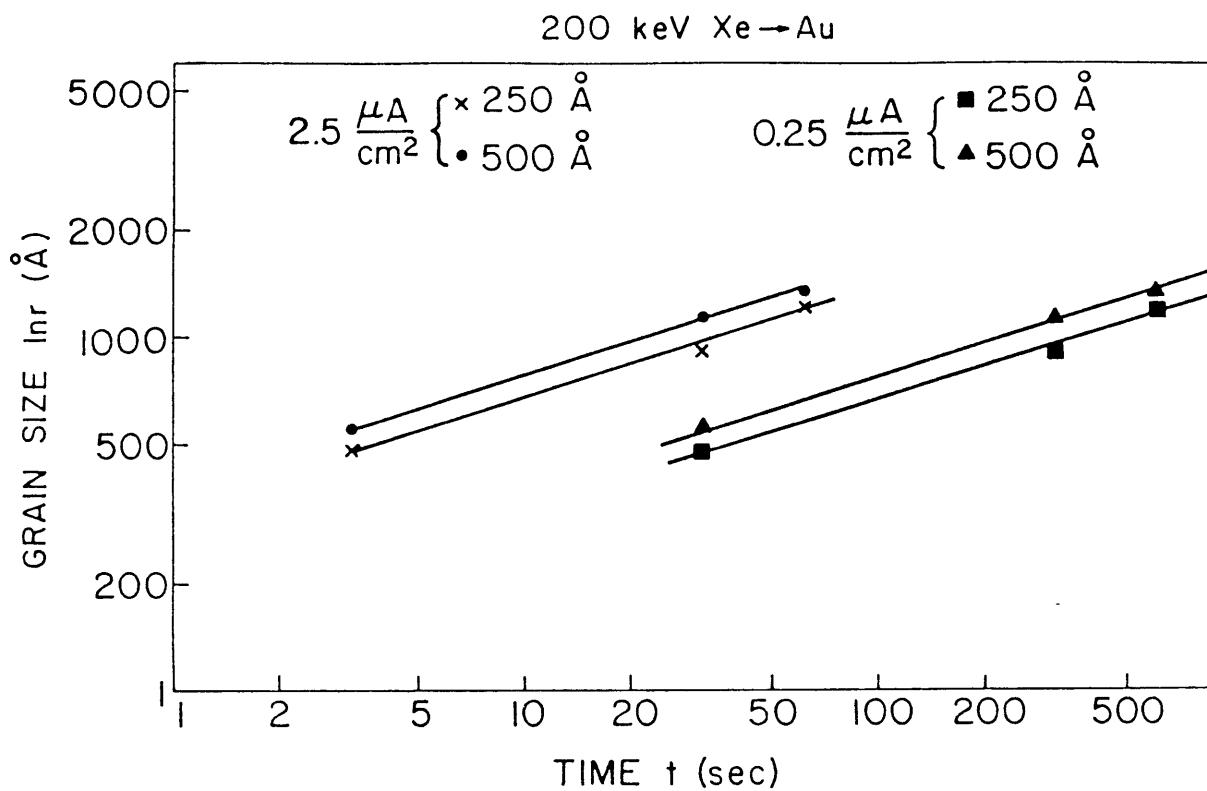
Figure 3.31: Variation of grain size with time for two different ion fluxes.
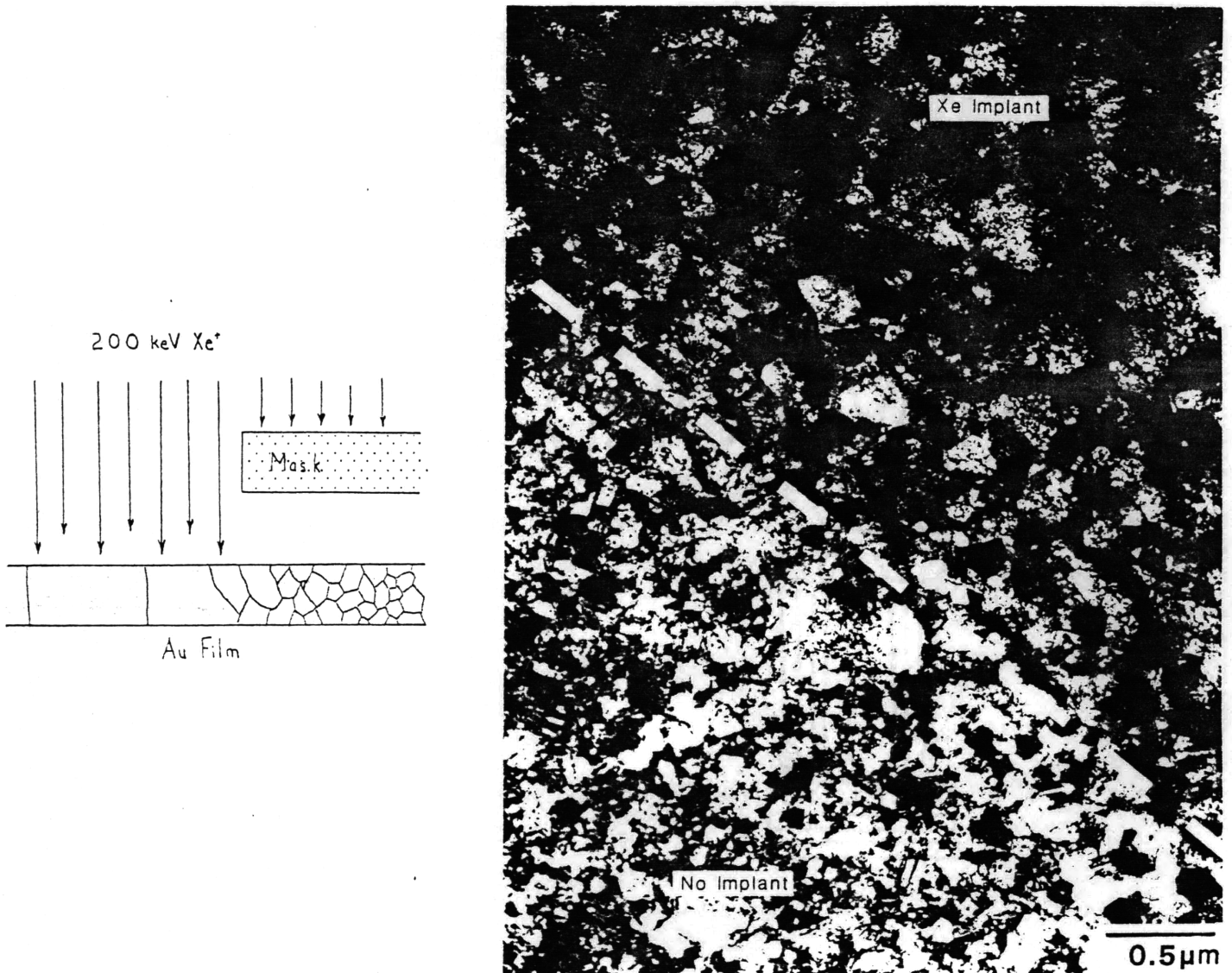
Figure 3.32: A 500 Å Au film which has been partially masked from exposure to a 200 keV Xe$^+$ beam is shown schematically in (a). The transmission electron micrograph of (b) illustrates the sharp delineation between the enhanced growth region which has been bombarded, and the unbombarded region which experience no enhanced grain growth.

Energy Dependence

The variation of grain size with incident ion energy in 250 Å Au films bombarded by 1 x 10^{15}/cm^2 of Kr$^+$ is shown in Fig. 3.33. The grain size increases with increasing ion energy in an approximately linear fashion. Also plotted is the number of defects produced/incident ion, as calculated using the TRIM code. A reasonable correlation is observed between the calculated defect yield and the grain size, a result which is in agreement with the Kinchin Pease model for defect production and the model proposed for IBEGG.

Ion Mass Dependence

The dependence of grain size with time for IBEGG with 80 keV Kr$^+$ and 200 keV Xe$^+$ ions is shown in Fig. 3.34. The time dependence is the same for both species, which is similar to the observations made for Ge films, implying that the grain growth process is similar in both cases. Figure 3.35 depicts the variation of grain size in 250 Å thick Au films with incident ion mass, at a constant dose of 1 x 10^{15}/cm^2. Also shown is the number of vacancy-interstitial pairs per incident ion at the given energy calculated using the TRIM code. A close correlation is seen between the number of vacancy-interstitial pairs produced per incident ion and the increase in grain size. This result, similar to that obtained for Ge films, again suggests that the defects responsible for IBEGG in Au films can be described using linear collision cascade theory and the Kinchin-Pease formalism.

Kr$^+$ ⟶ 250 Å Au

T = 23 °C

Q = 1 × 10^{15}/cm^2

Grain diameter (Å)

v-i pairs/ion

scale ⟵

⟶ scale
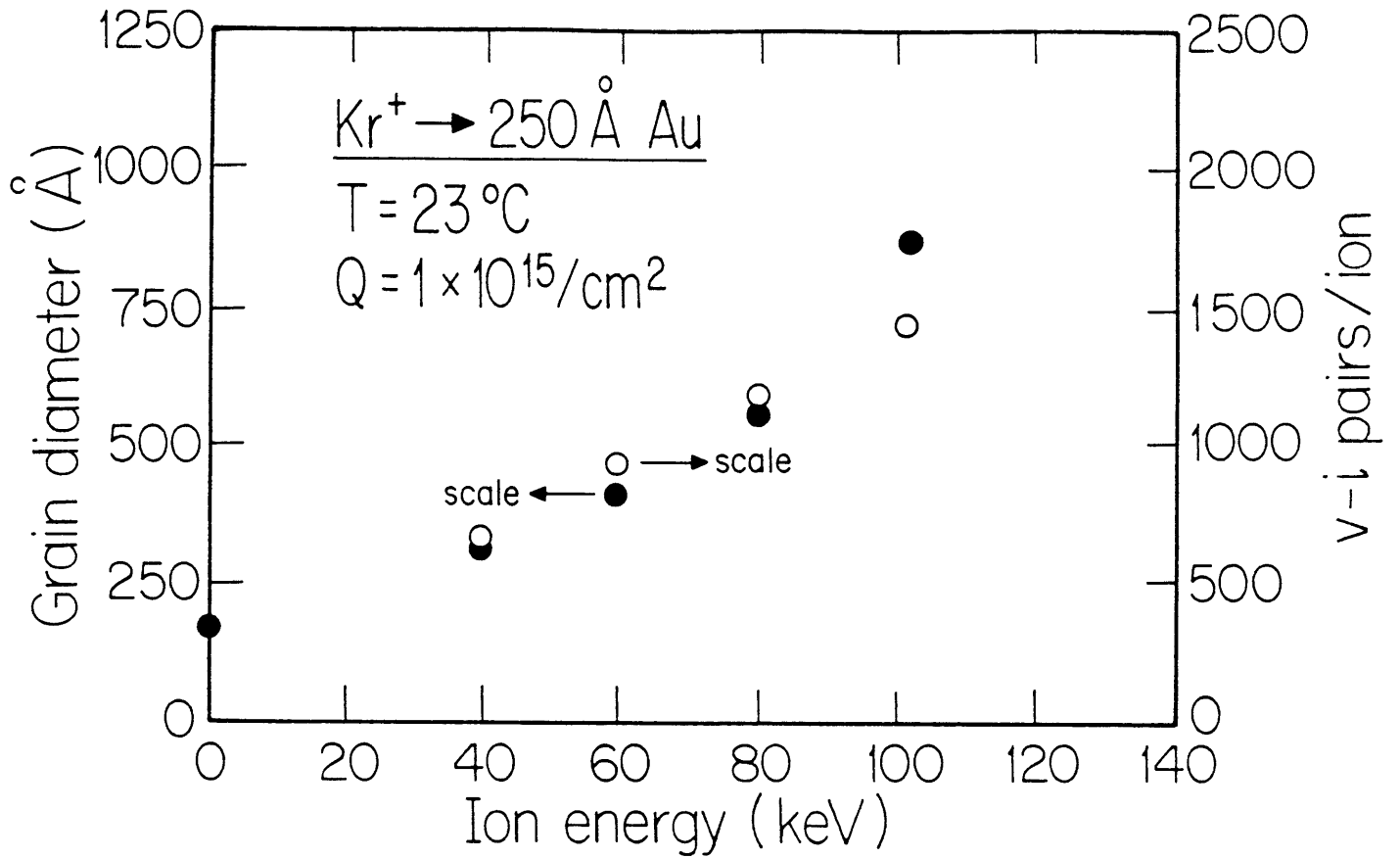
Ion energy (keV)

Figure 3.33: Variation of grain size with ion energy during IBEGG using a flux of 1.5 x 10^{12}/cm^2-sec. The dose was held constant at 1 x 10^{15}/cm^2.
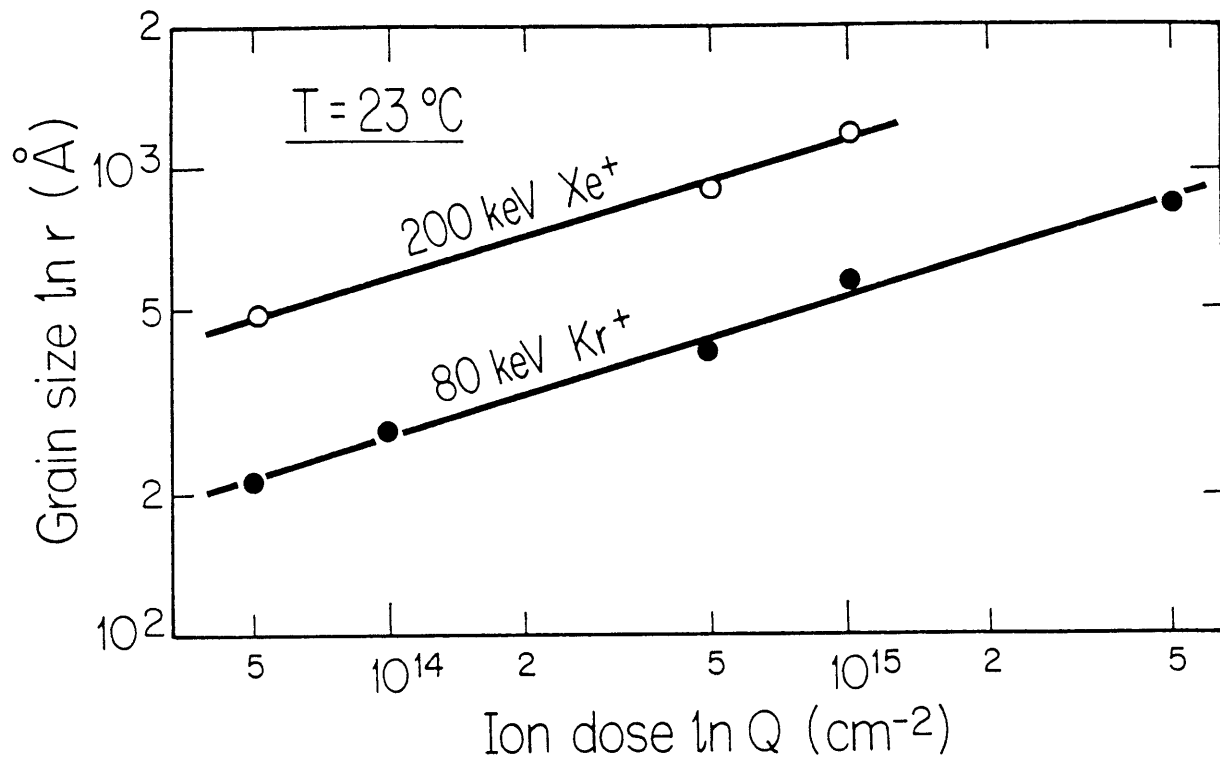
Figure 3.34: Variation of grain size with time for 80 keV Kr^+ and 200 keV Xe^+ ions incident on a 250 Å Au film.
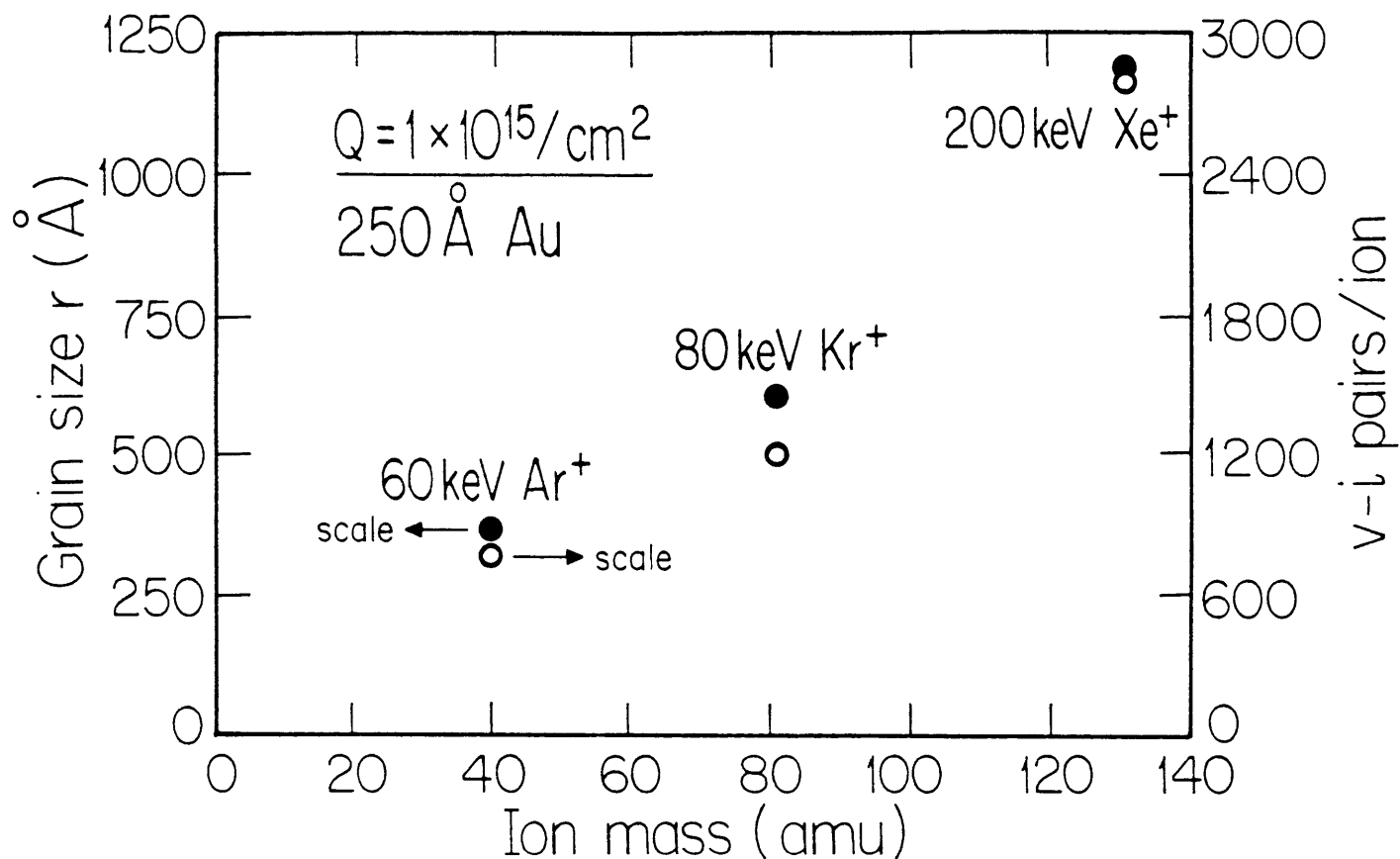
Figure 3.35: Comparison of grain size and the number of defects generated per incident ion with projectile ion mass during IBEGG in 250 Å Au films at room temperature. The ion dose was 1×10^{15} cm^2 for all cases.

3.2.3   Silicon Thin Film Kinetics

IBEGG Film Morphology

The microstructure of a silicon film during IBEGG is shown in Fig. 3.36. A 1000 Å Si film was bombarded with 150 keV Xe^+ with a current density of 1.8 x 10^{12}/cm^2-sec, and the substrate temperature was 850 °C. The substrate holder was inclined at an angle of 45° to the surface normal. In Figs. 3.36(a) and (b), a noncolumnar grain structure is seen for films bombarded with 1 x 10^{14}/cm^2 and 5 x 10^{14}/cm^2, respectively. At a dose of 1 x 10^{15}/cm^2, some grain growth is seen, and a dose of 5 x 10^{15} results in further grain growth as seen in Figs. 3.36(c) and (d).

At the highest dose studied here, the grain structure was not columnar. Cross-sectional TEM revealed that enhanced grain growth took place only within the top two-thirds of the 1000 Å Si film, which is consistent with estimates of the position of the damage profile, as shown in Fig. 3.37(a). The fact that the grain size was not uniform normal to the plane of the film introduced some uncertainty in grain size measurements taken in plan view. However, this finding is striking evidence in support of the IBEGG mechanism proposed here: *enhanced grain growth occurs as a result of elastic collisions at or very near grain boundaries, rather than by migration of defects from their points of generation to grain boundaries.* An unimplanted Si film also annealed at 850 °C is shown in the cross-sectional electron micrograph of Fig. 3.37(b), for comparison.
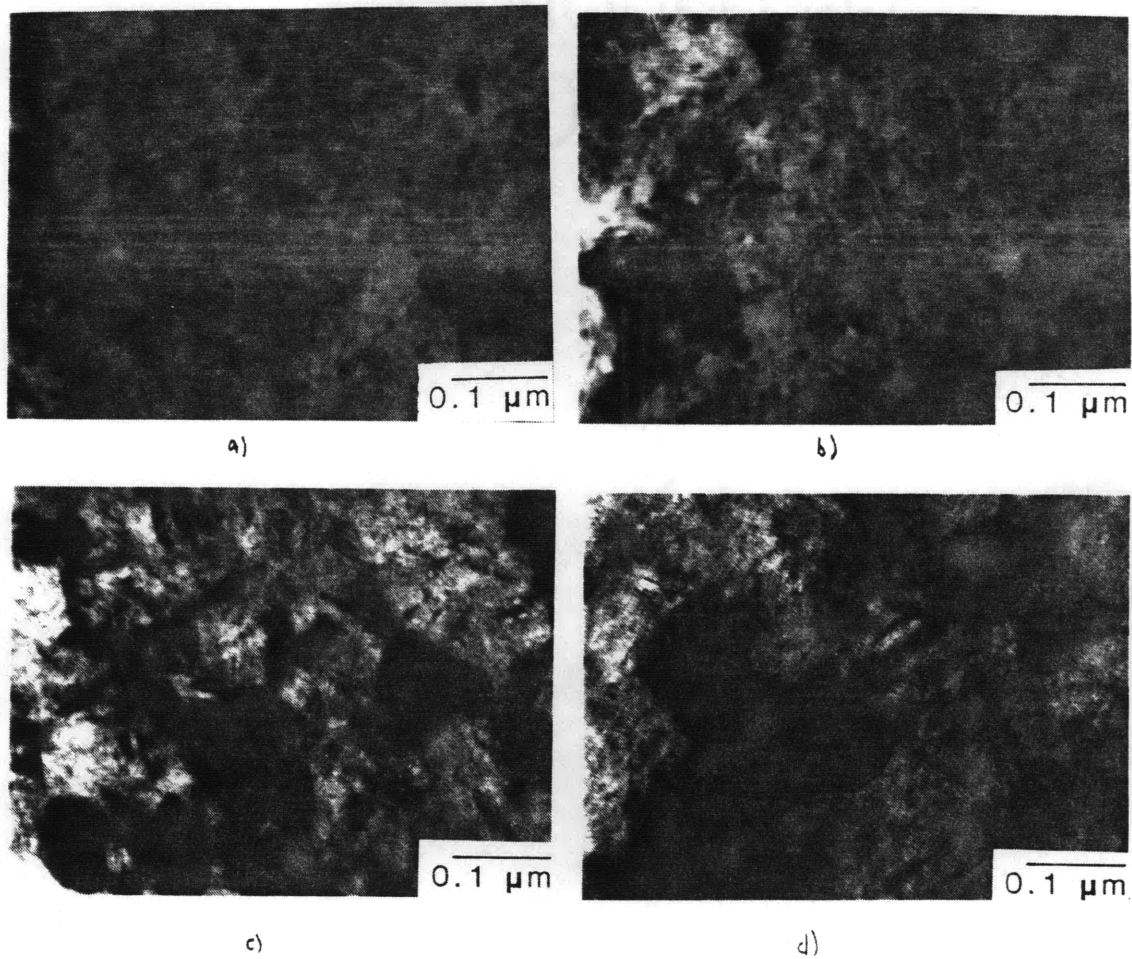
Figure 3.36: Microstructure of a 1000 Å Si thick film after IBEGG at 850 °C with 150 keV Xe^+ for various ion doses. In (a), $1 \times 10^{14}/cm^2$; in (b), $5 \times 10^{14}/cm^2$; in (c), $1 \times 10^{15}/cm^2$; and in (d) $5 \times 10^{15}/cm^2$.

a)

Damage
Profile

Undamaged
Si

b)
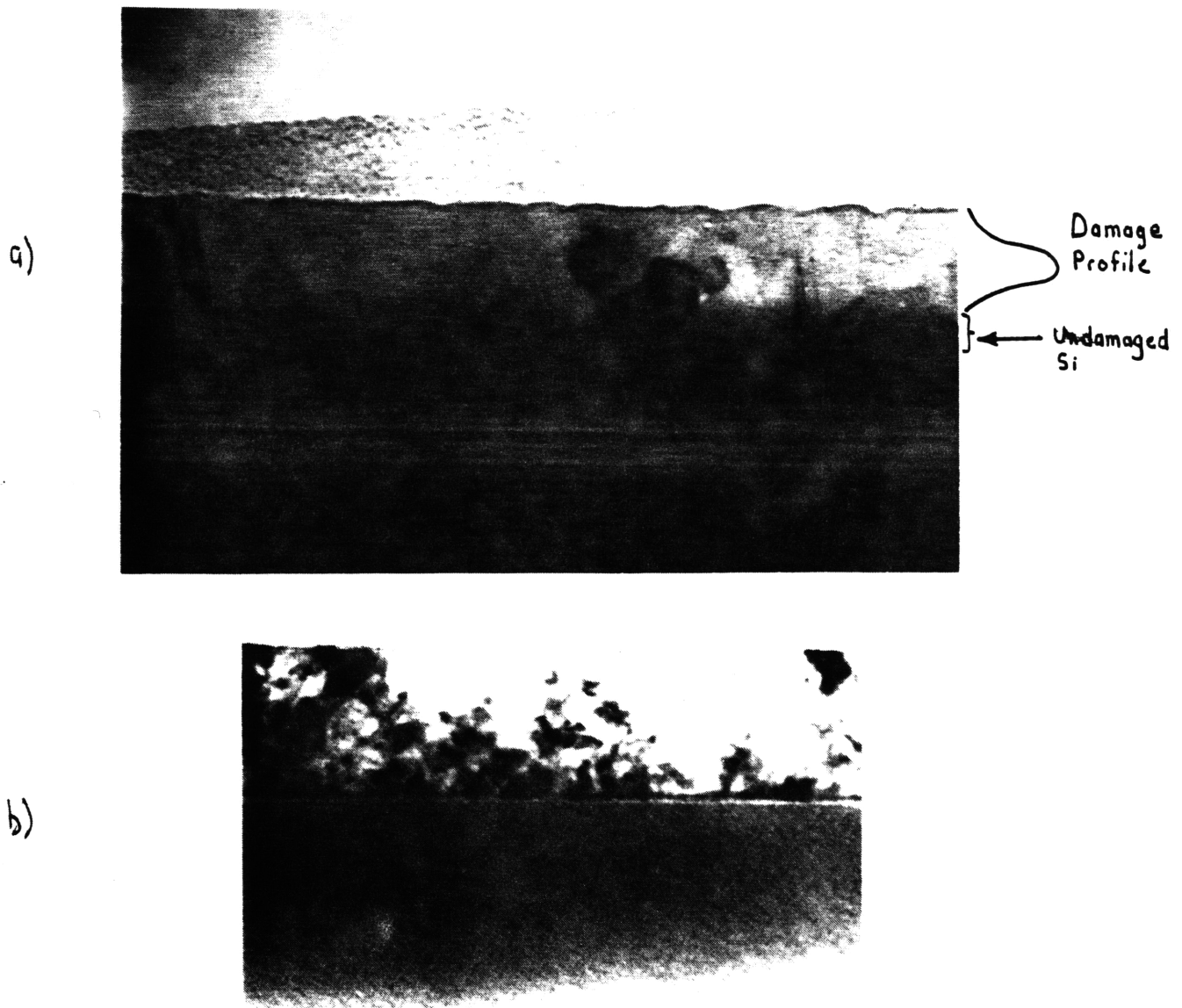
Figure 3.37: In (a), cross-sectional electron micrograph of a 1000 Å Si film after IBEGG at 850 °C with a 150 keV Xe$^+$ beam at a dose of 5 x 10^{15}/cm^2. A similar film which was thermally annealed at 850 °C is shown in (b).

Time Dependence

The time dependence for IBEGG in 1000 Å Si films is shown in Fig. 3.38. Data are shown for IBEGG with 70 keV Si^+ at 1050°C, 100 keV Ge^+ at 800 °C and 150 keV Xe^+ at 850°C. IBEGG is apparent only for ion doses above approximately 1 x 10^{15}/cm^2. This implies that the IBEGG process is less efficient in Si than in Ge or Au films. The slope of the curves indicate that for all cases $r(t) \approx t^{\frac{1}{3}}$, which is consistent with the results for Ge and Au.

Ion Mass Dependence

The rate of grain growth is proportional to the incident ion mass in a way similar to that seen in Ge and Au films, as seen in Fig. 3.38. Fig. 3.39 shows the dependence of grain size on incident ion mass for a 1000 Å Si film bombarded with Si^+, Ge^+ and Xe^+. Also shown is the yield of beam-generated defects/incident ion, which is quite well correlated with grain size.

Temperature Dependence

The dependence of grain growth rate on temperature is shown in Fig. 3.40 for a 1000 Å Si film bombarded with 150 keV Xe^+ with a current density of 0.3 $\mu A/cm^2$ between 750 and 850 °C. The results suggest that the activation energy for the rate-limiting step in grain boundary migration is between 0 and 0.1 eV. This is similar to the activation energy seen in Ge, and is much smaller than the activation energy of 2.4 eV reported for thermal
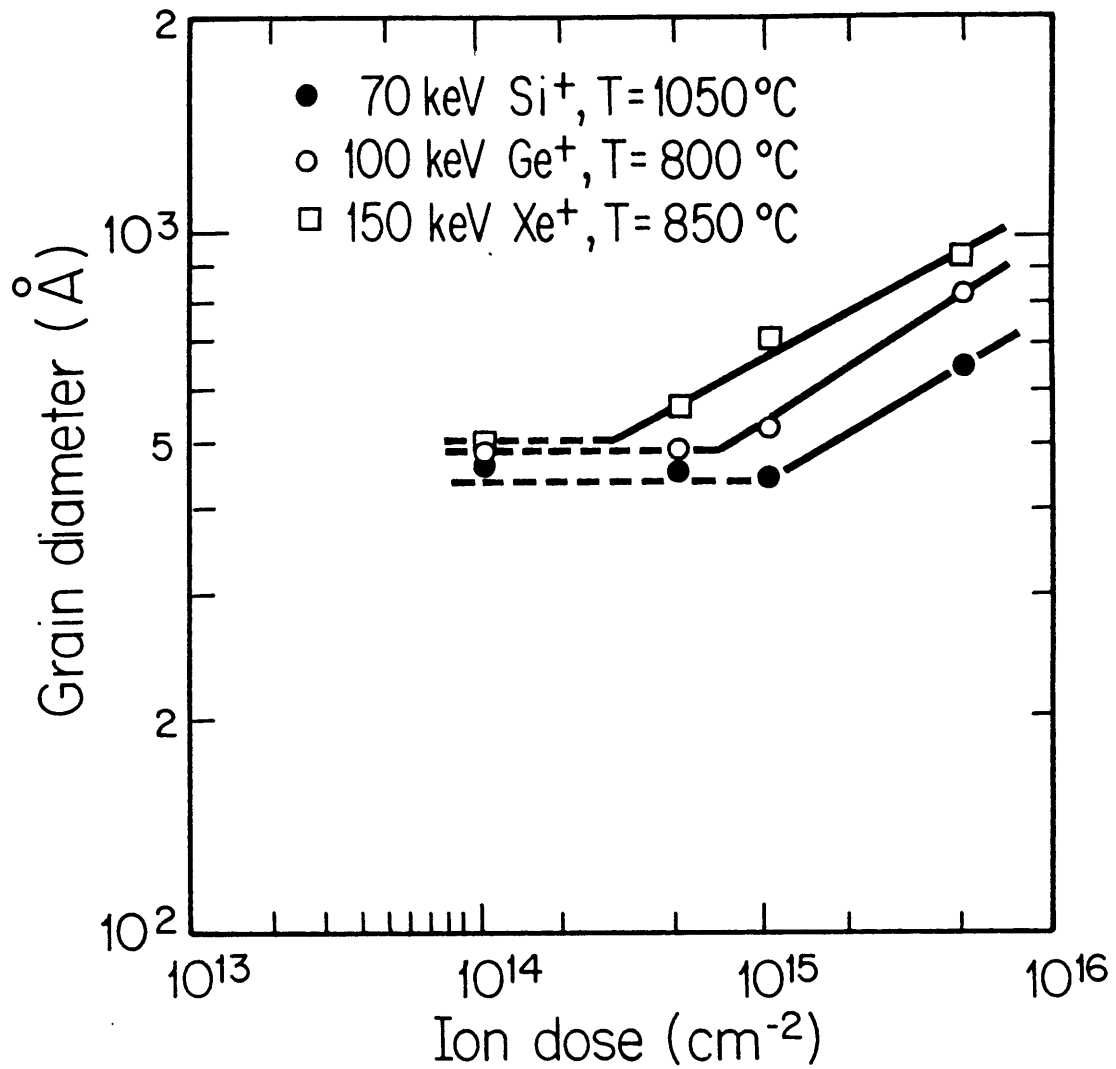
Figure 3.38: Variation of grain size with ion dose for 1000 Å Si films.
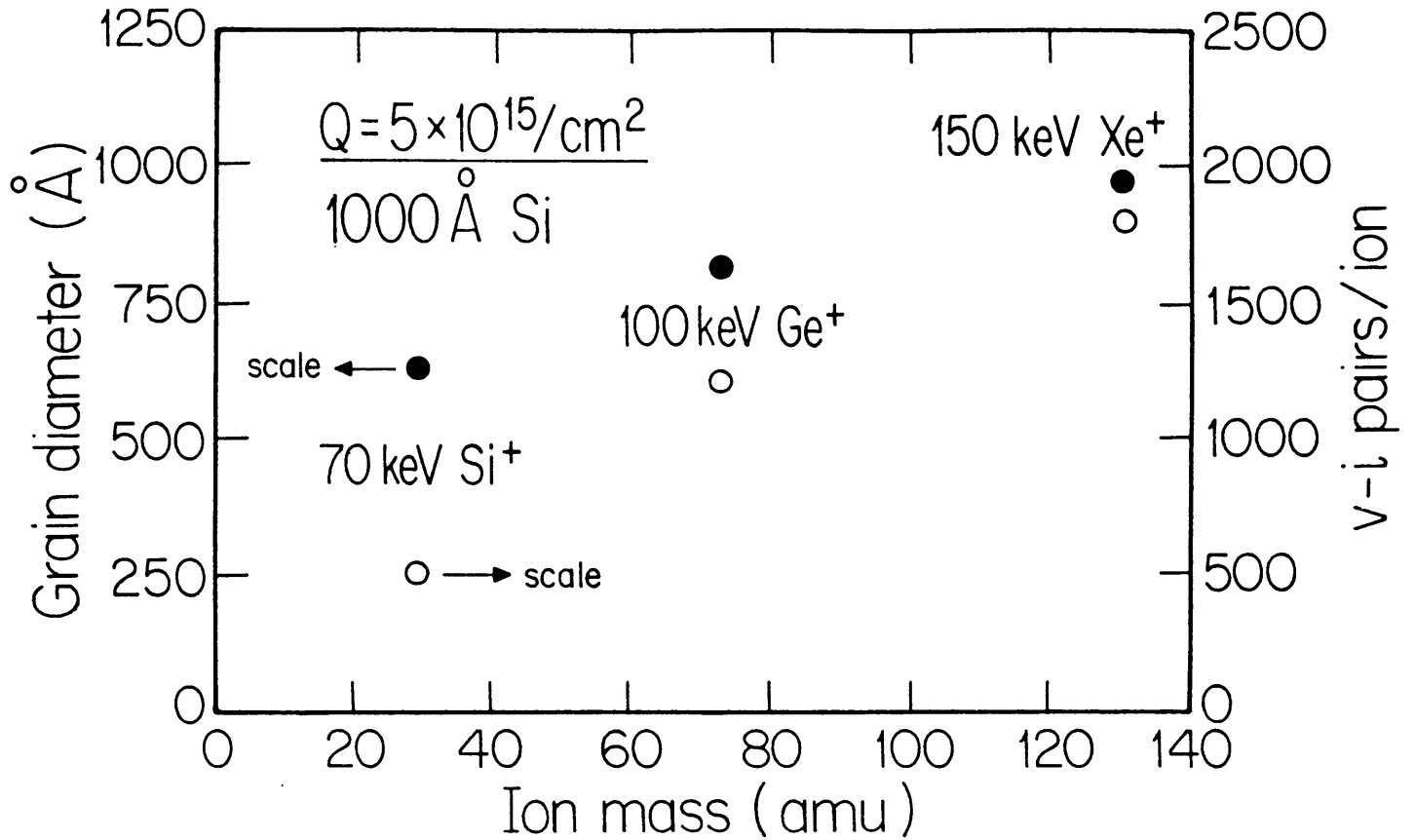
Figure 3.39: Comparison of grain size and the number of defects generated per incident ion with projectile ion mass during IBEGG in 1000 Å Si films at 850 °C. The ion dose was 5 x $10^{15}/cm^2$ for all cases.

grain growth of polycrystalline Si[94]. This energy is also lower than the reported value for vacancy migration in Si of 0.3 eV[52], lending support to the proposed model for grain growth in which bulk defect migration is not responsible for the growth enhancement.

3.3   A Model for Ion Beam Enhanced Grain Growth

3.3.1   Postulates of the Model

Three postulates are made about the IBEGG process which are based on simple assumptions and experimental observations. They are:

Postulate 1:

Only elastic collisions at or very near grain boundaries lead to enhanced grain growth. Defect migration from the interior of a grain to the boundary does not contribute to grain boundary motion.

The assertion of postulate 1) is founded on two experimental observations. These observations concern the temperature dependence and the time dependence for grain growth when IBEGG is compared with thermal annealing.

The observed temperature dependences for IBEGG in thin films indicate an activation energy for grain boundary motion of 0.15 eV for Ge and
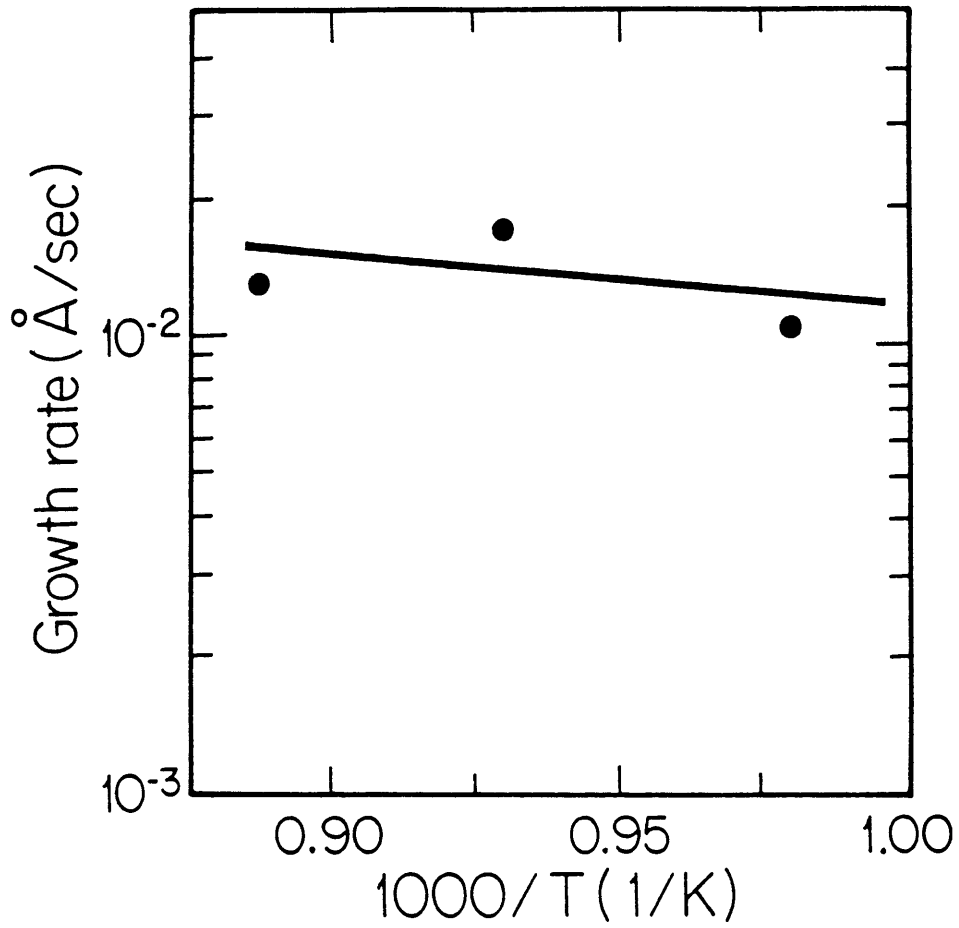
Figure 3.40: Arrhenius plot of growth rate of Si during ion beam enhanced grain growth at a constant current density of 0.3 μA/cm^2.

approximately 0.1 eV for Si. These activation energies are lower than any known energy of point defect formation or migration in Si and Ge, although these are not well known. Therefore it is assumed that a defect migration process is not the rate-limiting step in grain boundary migration during IBEGG. This said, it is nevertheless true that defects are created in the interior of each grain in the film. These defects presumably do migrate along defect concentration gradients. It seems plausible that the defects created within grains are responsible for the migration of dislocations which must occur in order to achieve the observed reduction in dislocation and stacking fault densities. In brief, although point defect creation and migration occur, it is proposed that the defects that participate in IBEGG do not migrate through the bulk of the grain. They are are created at or very near the grain boundary so that defect migration is not the rate-limiting step.

Another argument favoring postulate 1) can be made based upon the observed time dependence of the grain growth kinetics. For the thin films studied here, the time dependence during thermal and ion beam enhanced grain growth is similar; that is, the growth exponents were of the form

$$r(t) \propto t^n \tag{3.3}$$

where $n = 0.25 - 0.35$.

Now we can develop simple models for the kinetics of grain growth for two cases:

1. IBEGG in which only collisions at grain boundaries lead to grain growth.

2. IBEGG in which defects that are created throughout the film (within grains as well as near grain boundaries) contribute to grain growth.

It is assumed that, in the regime where these models apply, the rate of thermal grain growth is negligible.

Case 1: Mobility Enhancement from Elastic Collisions at Grain Boundaries

Assuming a spatially uniform ion flux leads to a grain boundary mobility, M_{IBEGG}, that is independent of grain radius, r. The driving force, ΔF, in normal grain growth is due to the elimination of grain boundary area, and is proportional to the principal radii of curvature of a grain[7]. When the grain's radii of curvature are assumed to be equal to the grain radius, the driving force is

$$\Delta F = 2\frac{\gamma_{gb}}{r} \tag{3.4}$$

The growth rate is

$$\frac{dr}{dt} = -M_{IBEGG}\bar{V}\Delta F \tag{3.5}$$

and

$$r^2(t) - r_o^2 = M_{IBEGG}\bar{V}4\gamma_{gb}t \tag{3.6}$$

This is simply the same expression that is obtained from a simple model of grain growth, except that the mobility is given by M_{IBEGG} rather than the thermal equilibrium mobility. Departures from the idealized $t^{\frac{1}{2}}$ kinetics are not well understood, but are frequently seen experimentally. A sharp reduction in growth rate upon development of a columnar grain structure, termed the specimen thickness effect, is often seen and may account for

the discrepancy. It is possible that thermal grooving is responsible for the specimen thickness effect.

Case 2: Point Defect Migration-Controlled Mobility Enhancement

Now we assume that defects are generated throughout the grain and they migrate to grain boundaries where they affect the mobility of the boundaries. The grains, which are polyhedral in a noncolumnar film, are assumed to be spherical for simplicity. The characteristic defect diffusion length, L_D, is assumed to be large compared to the grain size.

$$L_D = \sqrt{D_d \tau_d} \gg r \tag{3.7}$$

where D_d is the defect diffusivity and τ_d is the defect lifetime. This assumption has been found experimentally to be valid for Ge and Si for the cases of interest here[45]. This assumption implies that defect recombination within grains is negligible.

The number of defects created within a spherical grain with radius r in unit time is N_{vt}

$$N_{vt} = G_d \frac{4}{3} \pi r^3 \tag{3.8}$$

where G_d is the defect generation rate. The area of the grain boundary is

$$A = 4\pi r^2 \tag{3.9}$$

Hence the number of defects arriving at the boundary in unit area and in unit time is

$$\frac{N_{vt}}{A} = \frac{G_d}{3} r \tag{3.10}$$

Since we assumed in this case that the rate-limiting step in boundary motion is the rate of defects arriving at the boundary, the mobility in this case is

$$M_{IBEGG} = \frac{CG_d r}{3} \tag{3.11}$$

where C is constant. Assuming a similar driving force as in the first case, the growth rate is

$$\frac{dr}{dt} = M_{IBEGG}\bar{V}\Delta F = \frac{2CG_d\bar{V}\gamma_{gb}}{3} \tag{3.12}$$

Thus the change of grain size, r, with time is

$$r(t) = \frac{2CG_d\bar{V}\gamma_{gb}t}{3} \tag{3.13}$$

The experimental evidence favors mechanism 1), which leads to $r(t) \propto t^{\frac{1}{2}}$. The IBEGG data departs from this idealized time dependence in a manner similar to that of experimental data for thermal grain growth. Although the reasons for the discrepancy are not known, the data are consistent with other experimental investigations of normal grain growth, as mentioned before. Mechanism 2) leads to $r(t) \propto t$, which is certainly inconsistent with the IBEGG data. Hence, the observed time dependence for IBEGG is consistent with postulate 1).

Postulate 2:

Heating of the film by inelastic collisions, such as those due to electronic stopping and phonon production, are not important to enhanced grain growth.

The neglect of ion beam heating effects made in postulate 2) is based on calculations and experimental observation. The expected rise in temperature from typical ion beam current densities employed in this work is given

in Appendix 3. Direct observation of a lack of beam heating is shown in Fig. 3.31. A 250 Å Au film was partially masked from exposure to a 200 keV Xe^+ beam with a current density of 2.5 $\mu A/cm^2$. The transmission electron micrograph clearly shows enhanced grain growth in the region where the beam was incident on the film. The grain size in the masked region is similar to those in unimplanted films. The transition region between the large-grained bombarded region and the small-grained unbombarded region corresponds to the calculated lateral straggle of the ion beam. Clearly, if grain growth had resulted from a thermal anneal produced by ion beam heating, such a sharp delineation of regions would not be possible.

Postulate 3:

During normal grain growth to a columnar structure, ion bombardment has a negligible influence on the driving force for grain growth. That is, the driving force during IBEGG is similar to the driving force during thermal annealing.

Postulate 3) states that the driving force during normal grain growth to a columnar structure is unaffected by ion bombardment. Since the major component of the driving force is due to grain boundary energy, this implies that the grain boundary energy is assumed to be unperturbed by IBEGG. The results obtained for IBEGG in Au films suggest that the surface energy is modified by ion bombardment. In the absence of ion bombardment, surface-energy-driven secondary grain growth is observed in thin Au film, accompanied by a strong (111) crystallographic texture. During IBEGG, grain growth is characterized by a monomodal grain size distribution which

increases in size. A (111) texture is observed, but is not as strong as that seen during thermal annealing; grains of other textures frequently occur.

Thermal grooving of grain boundaries may also be affected by IBEGG, as illustrated by Fig. 3.15. Grooves can impede grain growth in a columnar film[9] In order to continue grain growth in a grooved film, grain boundaries must either move beyond grooves, which requires an increase in grain boundary energy, or move with the groove, which requires considerable mass transport. However, in a non-columnar film, only a few grain boundaries intersect free surfaces. Hence, only these grain boundaries have thermal grooves associated with them. Thus, if grain boundary energy is unaffected by ion bombardment, the total driving force is thought to be unaffected by the IBEGG process in noncolumnar films. As the film becomes more columnar, surface energy and thermal grooving make more significant contributions to the total driving force and their effects on IBEGG cannot be ignored.

3.3.2   A Transition State Model for IBEGG Kinetics

We now develop a simple expression based on rate theory for normal grain growth kinetics during ion bombardment. A generalized driving force, ΔF, is assumed to be due to reduction of grain boundary energy. The generalized mobility, M, has two terms. The first term, M_{th}, is the thermal equilibrium mobility. A second term, M_{IBEGG}, is due to ion beam enhanced grain growth. The growth rate is then

$$\frac{dr}{dt} = (M_{th} + M_{IBEGG})\bar{V}\Delta F \qquad (3.14)$$

Thermal Mobility

The thermal equilibrium mobility is determined from rate theory considerations in the usual way. Figure 3.41 depicts jumps across an energy barrier with height Q. In Fig. 3.41, the net number of jumps per unit time across a grain boundary in the forward direction, Δk, is

$$\Delta k = k_+ - k_- \tag{3.15}$$

where $k_+ = k_o e^{(-Q/kT)}$ and $k_- = k_o e^{-(Q+\Delta\mu)/kT}$. Hence Δk is related to the chemical potential, $\Delta\mu$, by

$$\Delta k = k_o e^{-(Q/kT)}\left(1 - e^{-\Delta\mu/kT}\right) \tag{3.16}$$

The chemical potential is related to the driving force by

$$\Delta\mu = \frac{\Delta F \bar{V}}{N} \tag{3.17}$$

where N is Avogadro's number and $\bar{V}$ is the atomic volume. The rate of grain boundary motion is then

$$\frac{dr}{dt} = \lambda \Delta k \tag{3.18}$$

where λ is the jump distance. For $\Delta F \bar{V} \ll NkT$,

$$\frac{dr}{dt} = -\frac{\lambda}{RT} k_o e^{-Q/kT}(\bar{V} \Delta F) \tag{3.19}$$

where $R = Nk$. The quantity k_o is related to a diffusivity D_o [106] by

$$k_o = \frac{D_o}{\lambda^2} \tag{3.20}$$
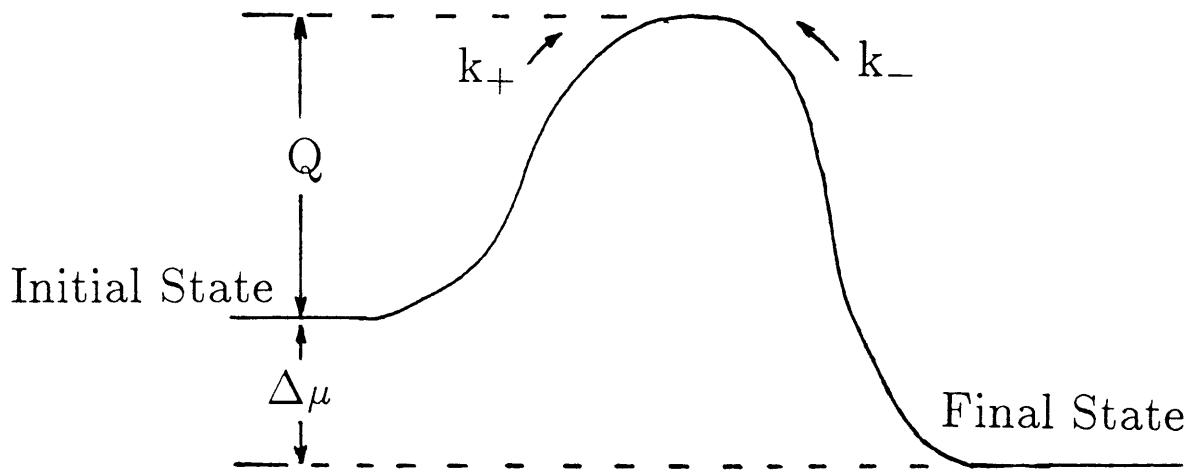
Figure 3.41: Schematic depicting jumps across an energy barrier with energy Q.

so

$$\frac{dr}{dt} = \frac{D_o \bar{V}}{\lambda RT} e^{-Q/kT} \Delta F \tag{3.21}$$

Written in generalized variables, the last expression is

$$\frac{dr}{dt} = -M_{th} \bar{V} \Delta F \tag{3.22}$$

where the thermal mobility is

$$M_{th} = \frac{D_o}{\lambda RT} e^{-Q/kT} \tag{3.23}$$

and the driving force from grain boundary energy is

$$\Delta F = \frac{2\gamma_{gb}}{r} \tag{3.24}$$

IBEGG Mobility

The mobility during ion beam enhanced grain growth is assumed to be of the form

$$M_{IBEGG} = \frac{M_o \frac{\lambda k_o}{RT} e^{-Q'/kT}}{M_o + \frac{\lambda k_o}{RT} e^{-Q'/kT}} \tag{3.25}$$

The energy Q' is the activation energy for the IBEGG process, which is quite different from the thermal activation energy and is in general assumed to be small. The pre-exponential factor M_o is assumed to be proportional to the defect generation rate, G_d.

$$M_o = C G_d \tag{3.26}$$

where C is a constant.

These assumptions can be incorporated into the rate theory picture of ion beam enhanced grain growth shown in Fig. 3.42. Ion beam generatio·
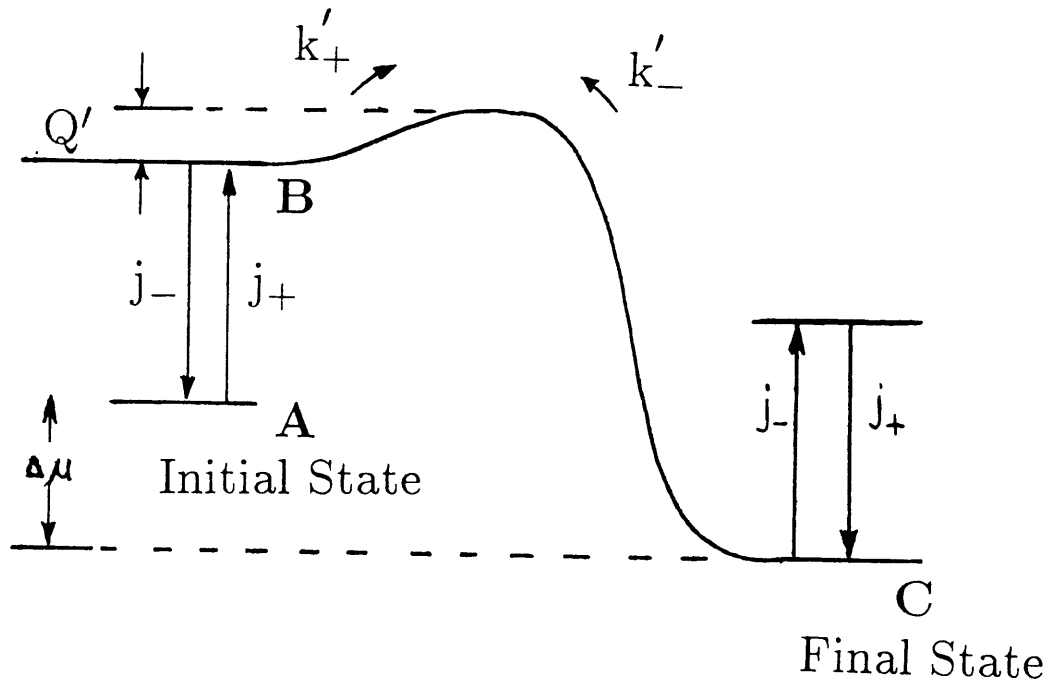
Figure 3.42: Schematic depicting jumps across an energy barrier with energy Q during IBEGG. The IBEGG process has a different rate limiting step with an activation energy of Q'.

of point defects causes boundary atoms to be promoted from state A) to state B). Detailed balance requires that transitions from state B) to state A) also be possible. The transition from state B) to state C) is a thermal process characterized by a new activation energy, Q'. The population of state B) is proportional to the defect generation rate G_d[8]. One can only speculate on the actual physical location of the intermediate state B). However, we presume that its location is within a few lattice constants of the grain boundary, because a bulk defect migration energy is not observed.

Referring again to Fig. 3.42, the net jump rate from state A) to state B) is Δj

$$\Delta j = j_+ - j_- = CG_d \qquad (3.27)$$

The thermal jump process from state B) to state C) is analogous to the previous case:

$$\Delta k' = k'_+ - k'_- = k_o e^{-Q'/kT}\left(1 - e^{-\Delta\mu/kT}\right) \qquad (3.28)$$

If the two steps are in series, the total jump rate from state A) to state C) is Δl, given by

$$\frac{1}{\Delta l} = \frac{1}{\Delta k'} + \frac{1}{\Delta j} \qquad (3.29)$$

$$\Delta l = \frac{\Delta k' \Delta j}{\Delta k' + \Delta j} \qquad (3.30)$$

When $\Delta k' \gg \Delta j$, then $\Delta l \simeq CG_d$. Conversely, when $\Delta j \gg \Delta k'$, then $\Delta l \simeq k_o e^{-Q'/kT}$. It is difficult to say from the experimental data whether $\Delta k'$ or

---

[8]The population of B) is actually proportional to the net rate of defect generation at the boundary and its inverse process, defect recombination. This is accounted for in the constant C.

Δj (or neither) is dominant. The activation energies measured for Ge and Si are so small that small uncertainties could imply that IBEGG is really temperature-independent, corresponding to the case of $\Delta k'$ dominance. On the other hand, the measured activation energies may be equal to the value Q' in the model.

Growth Rate

The grain growth rate for a general process including IBEGG and thermal annealing is given by

$$\frac{dr}{dt} = -(M_{th} + M_{IBEGG})\bar{V}\Delta F \qquad (3.31)$$

Integration yields

$$r^2(t) - r_o^2 = 4\gamma_{gb}\bar{V}(M_{th} + M_{IBEGG})t \qquad (3.32)$$

When the thermally generated defect concentration, n_{te}, dominates the IBEGG defect concentration, n_d, i.e., when $n_{te} \gg n_d$, ordinary thermal grain growth is obtained.

$$r^2 - r_o^2 = \frac{4\gamma_{gb}\bar{V}}{\lambda RT}D_o e^{-Q/kT}t \qquad (3.33)$$

When IBEGG dominates, i.e., when $n_{te} \ll n_d$,

$$r^2 - r_o^2 = 4\gamma_{gb}\bar{V}\frac{M_o\frac{\lambda k_o}{RT}e^{-Q'/kT}}{M_o + \frac{\lambda k_o}{RT}e^{-Q'/kT}}t \qquad (3.34)$$

Defect Generation Rate

The rate of generation of beam-produced point defects can be estimated from known experimental parameters and TRIM calculations. The defect

generation rate per atom, $G(z)$, can be related to the ion beam current density by

$$G(z) = \frac{J\mathcal{R}(z)}{qN_l} \qquad (3.35)$$

where q is electronic charge and N_l is the lattice atomic density of Ge. The quantity $\mathcal{R}(z)$ is the number of beam-generated defects/ion-cm. The z direction denotes distance into the film. The profile of $\mathcal{R}(z)$ is qualitatively similar to the range profile of the implanted ions. (The differences between the range profile and the damage profile are discussed in Chapter 2.) The total defect yield/ion, $\bar{R}$, is the parameter calculated by the TRIM program.

$$\bar{R} = \frac{1}{h}\int_0^h \mathcal{R}(z)dz \qquad (3.36)$$

where h denotes film thickness. If the beam generated defect profile varies slowly through the film thickness, then the defect yield/ion-cm can be approximated as

$$\mathcal{R}(z) \simeq \frac{\bar{R}}{h} \qquad (3.37)$$

Since all the grain size measurements are made from transmission electron micrographs taken in plan view, small variations in $\mathcal{R}$ with depth in the film should not affect grain size measurements severely, so this approximation is reasonable. The defect generation rate becomes G_d, in units of defects/sec,

$$G_d = \frac{J\bar{R}}{qN_l h} \qquad (3.38)$$

IBEGG Jump Rate - An Atomistic View

It is interesting to consider the jump rate at the boundary during IBEGG from a microscopic viewpoint. An idealized one-dimensional grain bound-

ary which spans the film thickness has a velocity $\Delta r / \Delta t$ given by

$$\frac{\Delta r}{\Delta t} = \lambda \Delta k \qquad (3.39)$$

where λ is the jump distance and Δk is the net rate of jumps in the forward direction, as before. The generation rate is

$$\frac{G_d}{h} = \frac{J\bar{R}}{qN_l h} \qquad (3.40)$$

The generation rate is assumed to be related to Δk by

$$\Delta k = C \frac{J\bar{R}}{qN_l h} \Delta F \qquad (3.41)$$

For the moment, the weak IBEGG temperature dependence is ignored. The velocity is then

$$\frac{\Delta r}{\Delta t} = \lambda C \frac{J\bar{R}}{qN_l h} \Delta F \qquad (3.42)$$

The coefficient C is the number of atomic jumps at the boundary per defect generated at the boundary, for a given driving force.

$$C = \frac{\Delta r N_l h}{\lambda Q \bar{R} \Delta F} \qquad (3.43)$$

where the ion dose $Q_d = J\Delta t / q$. The variation of Δr with Q_d has been measured and values for $\bar{R}$ have been calculated with TRIM. The values for C have been computed for various 500 Å Ge films in Table 3.1. The driving force was assumed to be a function only of grain size, not the microstructural topology of the film. In each case, the number if jumps/defect is in the range of 1 - 2.5. It is interesting to note that C is roughly constant, even though $\bar{R}$ varied widely. Also the value $C \approx 1$ is a physically plausible

Projectile Ion	Substrate	Temp.	$\bar{R}$	C
50 keV Ge	500 ÅGe, freestanding, am-dep	600 C	1131	2.5
50 keV Ge	500 ÅGe, freestanding, am-dep	500 C	1131	2.7
50 keV Ge	500 ÅGe/SiO$_2$, am-dep	600 C	1131	1.1
50 keV Ge	500 ÅGe/SiO$_2$, am-dep	500 C	1131	1.3
50 keV Ge	500 ÅGe/SiO$_2$, poly-dep	500 C	1131	1.7
50 keV Ge	500 ÅGe/SiO$_2$, poly-dep	600 C	1131	1.7
50 keV Ar	500 ÅGe/SiO$_2$, am-dep	600 C	762	1.7
50 keV Kr	500 ÅGe/SiO$_2$, am-dep	600 C	983	1.7
100 keV Xe	500 ÅGe/SiO$_2$, am-dep	600 C	2104	1.6

Table 3.1: Values for number of jumps at a grain boundary per defect generated for various 500 Å Ge films.

number in terms of the linear collision cascade model of defect generation, which assumes binary collisions between ions or recoils and target atoms.

Similar data are shown in Table 3.2 for 250 Å Au films under different IBEGG conditions. The grain boundary energies for Au and Ge were assumed to be approximately equal. The value of C is slightly higher for Au, which may be an indication that the grain boundary migration process is slightly different for Au than for Ge. However, the difference in C for Ge and Au may be a result of the assumption about grain boundary energy. Also, the jump distance, which was assumed to have the same value as in Ge, may be different.

In Table 3.3, data are given for C for Si films. As before, the grain boundary energy in Si is assumed to be similar to that in Au and Ge. The values of C are somewhat lower than the corresponding numbers for Ge and Au films. Again, it is difficult to determine whether this reflects a difference

Projectile Ion	Substrate	Temp.	$\bar{R}$	C
40 keV Kr	250 ÅAu, freestanding	23 C	608	4.1
60 keV Kr	250 ÅAu, freestanding	23 C	890	4.0
80 keV Kr	250 ÅAu, freestanding	23 C	1175	5.9
100 keV Kr	250 ÅAu, freestanding	23 C	1421	7.4
60 keV Ar	250 ÅAu, freestanding	23 C	703	7.3
200 keV Xe	250 ÅAu, freestanding	600 C	2681	5.2

Table 3.2: Values for number of jumps at a grain boundary per defect generated for various 250 Å Au films.

Projectile Ion	Substrate	Temp.	$\bar{R}$	C
70 keV Si	1000 ÅSi/SiO$_2$	1050 C	450	1.5
100 keV Ge	1000 ÅSi/SiO$_2$	800 C	1141	1.4
150 keV Xe	1000 ÅSi/SiO$_2$	850 C	1810	1.3

Table 3.3: Values for number of jumps at a grain boundary per defect generated for various 1000 Å thick Si films.

in IBEGG mechanism or is due to the approximation of the driving force and jump distance. Nonetheless, the values of C are quite consistent, even though $\bar{R}$ varied widely.

3.3.3   Comparison of Thermal and IBEGG Defect Concentrations

It is also interesting to compare the concentration of vacancy-interstitial pairs generated during IBEGG with the concentration of defects that exists

at thermal equilibrium at a given temperature. The thermal equilibrium
concentration of vacancies, n_{te} is

$$n_{te} \simeq N_l \exp -\frac{H_{fv}}{kT} \qquad (3.44)$$

where H_{fv} is the enthalpy of vacancy formation. For Ge, H_{fv} is approximately 1.9 eV[53]. The IBEGG defect concentration, n_{IBEGG}, can be approximated as

$$n_{IBEGG} \simeq \frac{J\bar{R}\tau}{2qh} \qquad (3.45)$$

where τ is the vacancy-interstitial pair lifetime.

For the case of the IBEGG data given in Fig. 3.18, $J = 0.25 \ \mu A/cm^2$, $R = 1194$, and τ is estimated to be 0.1 μsec, which is calculated based on the vacancy diffusivity given in [125], and assuming a diffusion length of approximately 600 Å in the Ge thin film. In this case $n_{IBEGG} = 1.9$ x $10^{13}/cm^3$. This is equal to the estimated thermal equilibrium defect concentration at T = 750 °C. Referring again to Fig. 3.18, it is seen that this is close to 710 °C, the temperature at which the measured growth rates for thermal annealing and IBEGG are equal. This may be an indication that the grain growth rate is proportional to the concentration of point defects at or very close to the boundary, regardless of whether they are generated thermally or by an ion beam.

Chapter 4

Strain and Microstructure in Ge Films

4.1 Introduction

Many studies have been undertaken of strain as a function of process-induced and thermal stress. However, very few have related the strain to microstructural changes in the sample under study. Such correlated studies are highly desirable, but are usually difficult to perform. We have done such a study of thin Ge films which have undergone thermal and ion beam enhanced grain growth. First order Raman scattering was used as a probe of the film strain and transmission electron microscopy (TEM) was used to examine the film microstructure. Raman spectroscopy has been

used by several groups as a probe of strain in silicon on sapphire (SOS) [107,108,109,110] and silicon on insulator (SOI) films [111,112], as well as Ge [113] and GaAs films [113,114]. The Raman technique is gaining wide use because of several powerful advantages.

1. The frequency of the zone center ($k \simeq 0$) phonons is strain-dependent. The first order Stokes Raman spectrum peak can be used to identify strain in thin films. Splitting of the Stokes peak can be used to identify anisotropies in the strain of the film. The linewidth of the peak can be affected by the crystalline perfection of the film, and can thus be used as an indication of the degree of crystalline perfection.

2. The area probed by the incident beam can be very small, allowing measurement of strain with high spatial resolution. Also, small samples can be used, simplifying experiments.

3. The use of a resonant or near-resonant probe beam results in a very short optical absorption length. This allows the measurement of strain in very thin samples.

In the present investigation, we exploit all of these advantages. By relating strain to the microstructure of the film, we attempt to answer questions about the kinetics of film growth. Strain can be correlated with such microstructural changes as grain growth, and dislocation density reduction during thermal annealing or ion beam enhanced grain growth. Strain energy can also be a driving force for transformations in materials. Knowledge of the magnitude of the strain energy and its variation with processing

conditions allows the contribution of strain to the driving force to be calculated. Thus, it is possible to compare estimates for the strain energy to values for the other contributions to the driving force.

4.2 Strain-Dependent Raman Frequency in Thin Ge Films

In the presence of strain the dynamical equations which describe phonon modes in the solid have the form[115,116,117]

$$\bar{m}\ddot{u}_i = -\sum_j K_{ij}u_j \tag{4.1}$$

$$\bar{m}\ddot{u}_i = -\left(K^0_{ii}u_i + \sum_{jkl} \frac{\partial K_{ij}}{\partial \epsilon_{kl}} \epsilon_{kl} u_j\right) \tag{4.2}$$

where u_i is the ith component of the relative displacement of the atoms in the unit cell, $\bar{m}$ is the reduced mass of the two atoms, $K^0_{ii} = \bar{m}\omega_o^2$ is the spring constant of the phonon modes in the absence of strain. The double-dotted quantities indicate second derivatives. The quantity

$$\frac{\partial K_{ij}}{\partial \epsilon_{kl}} \epsilon_{kl} = K^1_{ijkl} \epsilon_{kl} \tag{4.3}$$

is the change in the spring constant due to the strain ϵ_{kl}; i, j, k and l denote crystallographic axes. Since Ge is a cubic crystal, there are only three independent K^1 terms in the Raman-strain tensor, which are

$$K^1_{iiii} = \bar{m}p \tag{4.4}$$

$$K^1_{iijj} = \bar{m}q \tag{4.5}$$

$$K^1_{ijij} = \bar{m}r \tag{4.6}$$

The secular equation for the Raman frequency in a cubic crystal with strain is

$$\begin{vmatrix} p\epsilon_{xx} + q(\epsilon_{yy} + \epsilon_{zz}) - \lambda & 2r\epsilon_{xy} & 2r\epsilon_{xz} \\ 2r\epsilon_{xy} & p\epsilon_{yy} + q(\epsilon_{xx} + \epsilon_{zz}) - \lambda & 2r\epsilon_{yz} \\ 2r\epsilon_{xz} & 2r\epsilon_{yz} & p\epsilon_{zz} + q(\epsilon_{xx} + \epsilon_{yy}) - \lambda \end{vmatrix} = 0 \tag{4.7}$$

where the notation has been adopted from other authors [113,116]. The quantity $\lambda = \Omega^2 - \omega_o^2$, where Ω is the strain-dependent frequency of the optical phonons. We can approximate

$$\Omega \approx \omega_o + \frac{\lambda}{2\omega_o} \tag{4.8}$$

The notation is referred to a coordinate system of crystallographic axes in Ge where $x = [100], y = [010]$ and $z = [001]$. In our films, a biaxial stress can be assumed. The film is polycrystalline, so the strain dependence of the Raman frequency and the stress-strain relation for the film is complicated. These quantities have been measured for single crystals [116] of Ge. Hence for the polycrystalline film under consideration here, we will consider these relations to be averages of the corresponding values for (100) and (111) single crystals.

We now consider the relation between Raman frequency, stress and strain for (100) and (111) crystals under biaxial strain by solving the secular equation and developing the stress-strain relations for these orientations. These relations are more fully developed in Appendix B.

Biaxially Strained (100) Crystal

For a (100)-textured crystal under biaxial strain, there are two nonzero components to the stress

$$\sigma = \sigma_{xx} = \sigma_{yy} \qquad (4.9)$$

and three nonzero strain components

$$\epsilon_{xx} = \epsilon_{yy} = (s_{11} + s_{12})\sigma \qquad (4.10)$$

$$\epsilon_{zz} = 2s_{12}\sigma \qquad (4.11)$$

The solution to the secular equation yields a singlet solution $\Omega_s^{(100)}$ and a doublet solution $\Omega_d^{(100)}$ for the Raman frequency (see Appendix B).

$$\Omega_s^{(100)} = \omega_o + \frac{\sigma}{2\omega_o}[2pS_{12} + 2q(S_{11} + S_{12})] \qquad (4.12)$$

$$\Omega_d^{(100)} = \omega_o + \frac{\sigma}{2\omega_o}[p(S_{11} + S_{12}) + q(S_{11} + 3S_{12})] \qquad (4.13)$$

where σ is the biaxial in-plane stress in the film.

Biaxially Strained (111) Crystal

For a (111)-textured crystal under biaxial strain, there are nine components of strain

$$\epsilon_{xx} = \epsilon_{yy} = \epsilon_{zz} \qquad (4.14)$$

$$\epsilon_{yz} = \epsilon_{zx} = \epsilon_{xy} = \epsilon_{xz} = \epsilon_{zy} = \epsilon_{yx} \qquad (4.15)$$

and nine components of stress

$$\sigma_{xx} = \sigma_{yy} = \sigma_{zz} \qquad (4.16)$$

$$\sigma_{yz} = \sigma_{zx} = \sigma_{xy} = \sigma_{zy} = \sigma_{xz} = \sigma_{yx} \qquad (4.17)$$

The secular equation has one solution

$$\Omega^{(111)} = \omega_o + \frac{\sigma}{2\omega_o((\frac{5}{2})^{\frac{1}{2}}\cos\theta_1 + \cos\theta_2)}[(p+2q)(S_{11}+2S_{12}) + 2(\frac{5}{2})^{\frac{1}{2}}rS_{44}]$$

$$(4.18)$$

where the angles θ_1 and θ_2 are derived in Appendix B.

Biaxially Strained Polycrystalline Film

As discussed above, the observed biaxial strain will be considered to be an average of the strains in the (100) and (111) directions. The observed Raman shift, $< \Omega >$, is assumed to be an average over these orientations.

$$< \Omega > = \frac{1}{2}\Omega^{(111)} + \frac{1}{4}\Omega_s^{(100)} + \frac{1}{4}\Omega_d^{(100)}$$

$$(4.19)$$

The values for the elastic constants in Ge, which have been determined [118,119] and the coefficients of the Raman strain tensor, which have been measured [116], are given in Table 4.1.

An alternative expression for stress and strain in the polycrystalline film could be developed using the stress-strain relations for an isotropic material. However, since the strain-Raman coefficients have been previously measured for single crystal Ge[117], which is cubic, cubic stress-strain relations were employed.

The average shift in the Raman frequency due to strain, $\Delta\Omega$, is

$$< \Delta\Omega > = < \Omega > -\omega_o$$

$$(4.20)$$

Using the formalism and coefficients given above the equation for the biaxial in-plane stress, σ, for a polycrystalline film is

$$\sigma \quad (dynes/cm^2) = 2.6 \ x \ 10^9 \ < \Delta\Omega > \quad (cm^{-1})$$

$$(4.21)$$

Quantity	Value
S_{11}	9.7×10^{-13} cm^2/dyne
S_{12}	-2.7×10^{-13} cm^2/dyne
S_{44}	1.49×10^{-12} cm^2/dyne
ω_o^2	3.19×10^{27} sec^{-2}
r	-6.5×10^{27} sec^{-2}
q	-6.2×10^{27} sec^{-2}
p	-4.7×10^{27} sec^{-2}

Table 4.1: Parameters for the Raman strain relations for Ge.

The biaxial in-plane strain, ϵ, in the polycrystalline film is

$$\epsilon = 1.9 \ x \ 10^{-3} < \Delta\Omega > \quad (cm^{-1}) \qquad (4.22)$$

4.3 Raman Experimental Arrangement

The experimental apparatus used for Raman measurements is shown in Fig. 4.1. The incident beam was a 514.5 nm line from an Ar$^+$ ion laser. The lens L_1 was used to focus the incident beam on the sample at an oblique angle. The beam spot diameter was approximately 10 μm. The samples were all 500 Å Ge films on 1000 Å of thermally grown SiO$_2$ on Si substrates. The Ge films were grown under different conditions, as described below. The incident laser power was 2 mW. The scattered radiation was focussed by L_2 and spectra were recorded by scanning a Spex 0.85m spectrometer and photon counting. The spectrometer resolution was approximately ± 0.1 cm^{-1}.

One problem with the use of a small laser spot is the control of sample
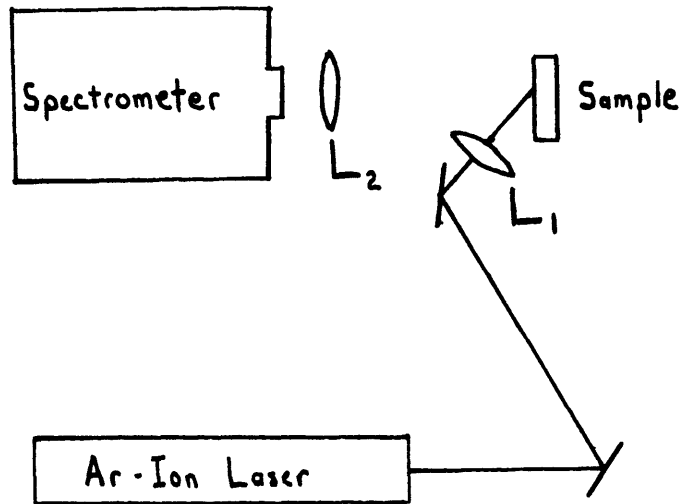
Figure 4.1: Diagram of Raman apparatus.

heating. Since strain is temperature-dependent, the peak frequency of the Raman line in the film is also a function of temperature. To address concerns about sample heating, one sample was measured with incident power levels between 0.1 mW and 5 mW. No change in the Raman spectra was observed as a function of incident power level. This finding was interpreted as evidence that the sample was not heated by the laser beam. The optical absorption coefficient in crystalline Ge at 514.5 nm is approximately 6×10^5 cm^{-1}, corresponding to a characteristic absorption length of approximately 160 Å. Hence the Raman spectra reflect the strain in the top half of the 500 Å thick films.

Samples for Raman spectroscopy were 500 Å Ge films deposited on 1000 Å of thermally grown SiO_2 on Si substrates. Samples were deposited in two forms. Some samples, denoted as amorphous-deposited, were deposited at

room temperature by electron beam evaporation, and were presumably amorphous. These samples were subsequently crystallized when annealed in a furnace or during ion beam enhanced grain growth. Other samples were formed by evaporating Ge onto substrates heated to 400 °C. These films, denoted polycrystalline-deposited, were polycrystalline as-deposited and had an approximately columnar grain structure.

The films denoted as stripes were patterned into 4 μm wide lines by photolithography and wet etching. The films denoted as continuous were not patterned after deposition.

The type of anneal is denoted as either thermal or IBEGG. Thermal anneals were were done in an isothermal furnace in quartz ampules evacuated to approximately 10^{-7} Torr. IBEGG denotes ion beam-enhanced grain growth for the time and temperature indicated. The incident beam was a 50 keV beam of ^{74}Ge^{+} with an ion flux of 1.5 x 10^{12}/cm^2-sec at normal incidence to the samples. The deposition condition, film, annealing condition, and the time and temperature of the anneal are summarized in Table 4.2.

4.4 Strain Measurements

Strain Variation with Thermal Annealing

The first order Raman spectra for amorphous-deposited films which have undergone thermal annealing are shown in Fig. 4.2. The spectrum of a bulk (111) Ge sample is shown for comparison. The shift of the spectra of the amorphous-deposited films to lower wavenumbers clearly indicates

Sample	Deposition	Film	Temperature T (°C)	Time t (min)	Anneal	Ion Dose Q (cm^{-2})
GE001	Polycrystalline	Continuous	600	60	IBEGG	5×10^{14}
GE002	Polycrystalline	Continuous	600	60	IBEGG	5×10^{15}
GE003	Polycrystalline	Continuous	600	60	IBEGG	1×10^{16}
GE007	Amorphous	Continuous	600	60	Thermal	—
GE016	Amorphous	Continuous	600	60	IBEGG	5×10^{15}
GE017	Amorphous	Continuous	600	60	IBEGG	8×10^{15}
GE018	Amorphous	Continuous	600	60	IBEGG	1×10^{16}
GE004	Amorphous	Continuous	600	60	IBEGG	2.5×10^{16}
GE006	Amorphous	Stripes	600	60	IBEGG	2.5×10^{16}
GE009	Amorphous	Continuous	750	60	Thermal	—
GE008	Amorphous	Continuous	750	60	IBEGG	5×10^{15}
GE014	Amorphous	Continuous	500	60	Thermal	—
GE015	Polycrystalline	Continuous	400	10	Thermal	—
GE011	Polycrystalline	Continuous	910	60	Thermal	—
GE012	Amorphous	Continuous	910	60	Thermal	—
GE013	(111) Bulk		—	–	—	—

Table 4.2: Samples prepared for Raman spectroscopy.

that the films are under tensile strain. Thermal annealing at 750 °C and 910 °C for one hour causes the tensile strain to be partially relieved. In general, strain in crystalline germanium causes the three-fold degenerate zone-center optical phonon to shift and split. Although shifts are seen, no splitting was observed in these or any other spectra. This may indicate either that information about splitting is lost because the measured signal is an areal average over grains of many orientations, or that only the hydrostatic component of the strain is observable.

Strain Variation with Film Deposition Conditions

In Fig. 4.3 , the first order Raman spectra of amorphous-deposited and polycrystalline-deposited 500 ÅGe films are compared. The spectrum of a bulk (111) Ge sample is shown for comparison. Both the amorphous-deposited and polycrystalline-deposited films are under tensile strain, but the strain in the amorphous-deposited film is clearly larger.

Strain Variation with Ion Bombardment

Figure 4.4 shows the Raman spectra for continuous amorphous-deposited films which have undergone ion beam enhanced grain growth at 600 °C. As with the above, the films are all under tensile strain. The strain is clearly a function of ion dose, with reduced stress occurring as the dose increases. Similar spectra are shown in Figure 4.5 for polycrystalline-deposited films. As with the amorphous-deposited films, the tensile strain decreases as the ion dose increases. As above, the spectrum of a bulk (111) Ge sample is
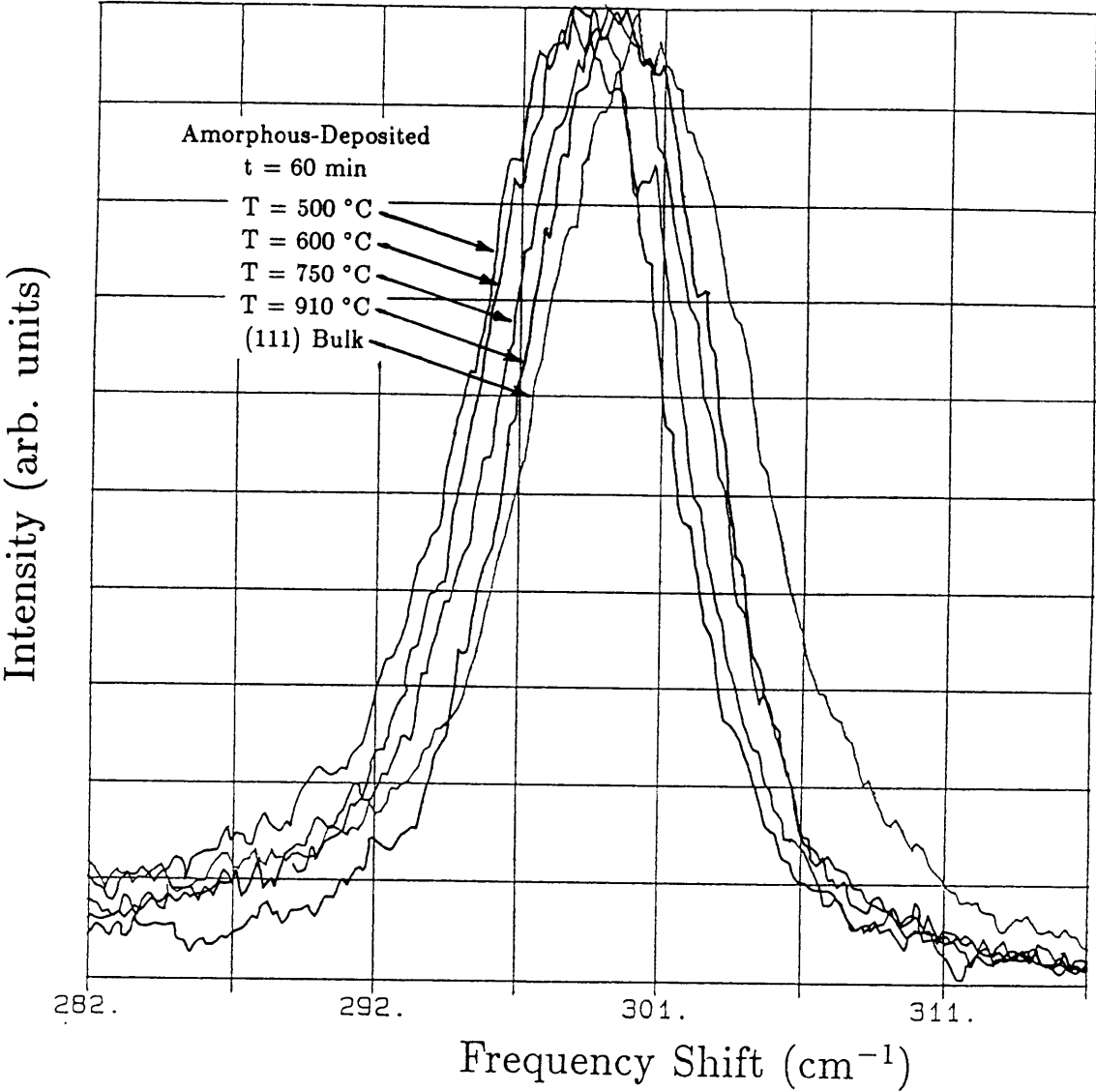
Figure 4.2: Raman spectra of amorphous-deposited, thermally annealed films
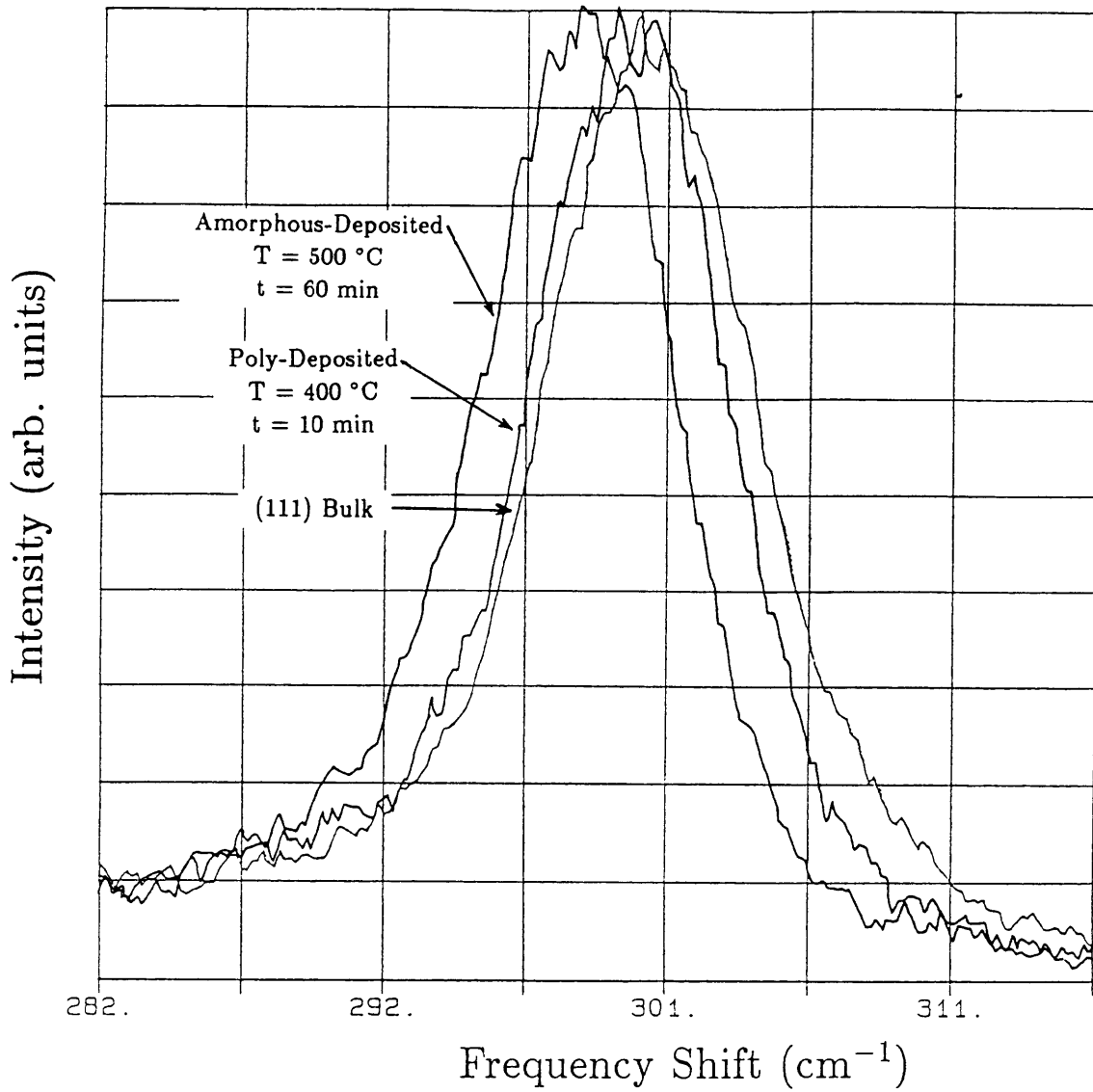
Figure 4.3: Raman spectra of amorphous-deposited and polycrystalline-deposited films.

shown for comparison.

Strain Variation with Film Patterning

Figure 4.6 shows the Raman spectra for patterned amorphous-deposited films which have undergone ion beam enhanced grain growth at 600 °C. Spectra are shown for 4 μm stripes and a continuous film. Both received an ion dose of 2.5 x $10^{16}/cm^2$. A spectrum from a continuous film is shown for comparison. There is no observable difference in the Raman peak frequency between continuous films and those patterned into stripes. This is understandable, when the aspect ratio of the stripes is considered. A 4 μm-wide stripe in a 500 Å-thick film has an aspect ratio of 80:1. Hence, it is reasonable to assume that relief of the tensile strain occurs only near the edges of the stripes, and the majority of the signal comes from areas of the film which are under a strain comparable to that in a continuous film.

4.5 Relation of Strain to Microstructure and Processing

The information contained in the Raman spectra of Figs. 4.2 - 4.6 is summarized in Table 4.3. The in-plane biaxial stress and strain are calculated following the procedure outlined above. The negative signs indicate tensile strain and stress.

It is important to make a distinction between the strain measured at
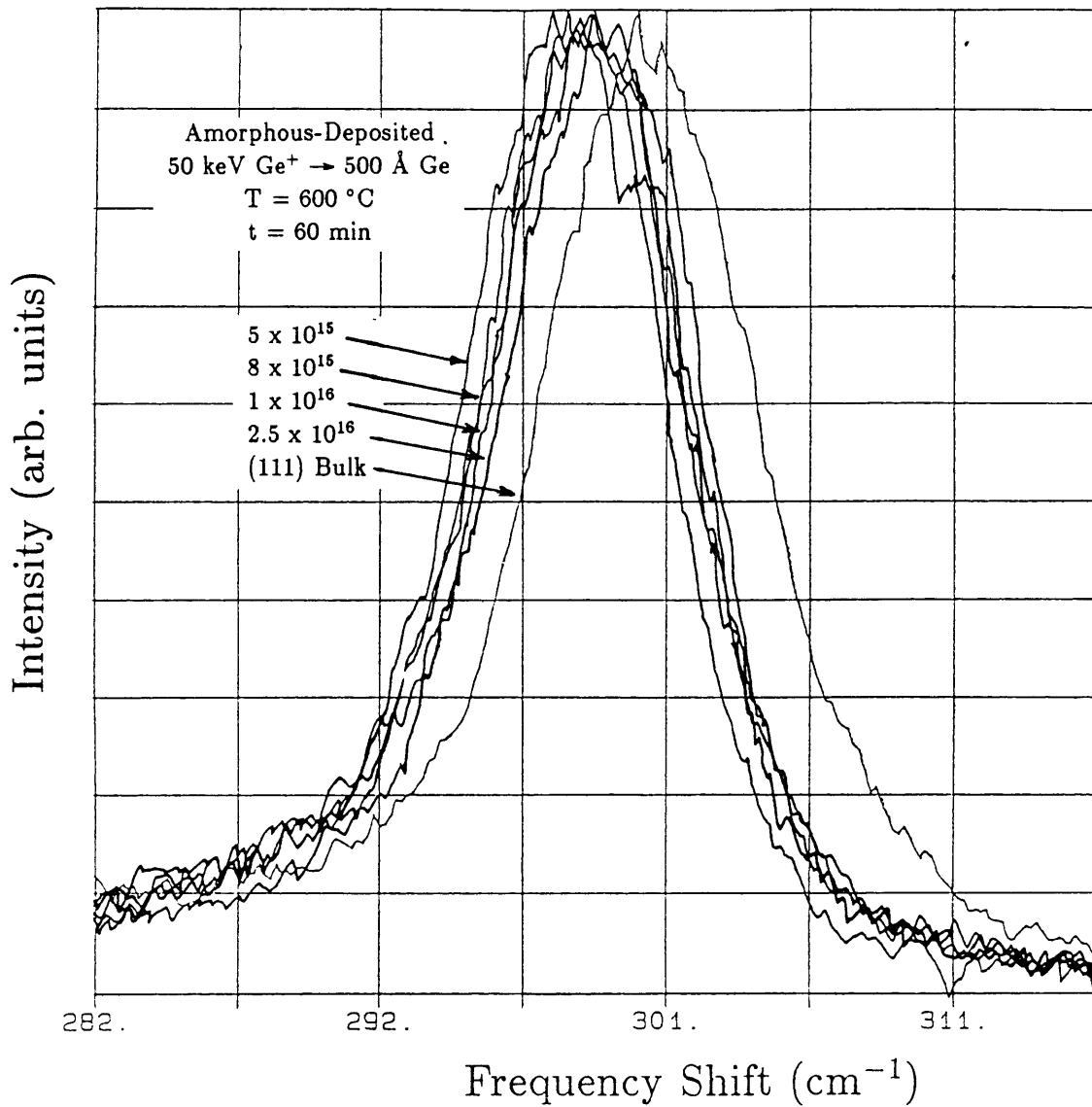
Figure 4.4: Raman spectra of continuous, amorphous-deposited films after ion beam enhanced grain growth at 600 °C
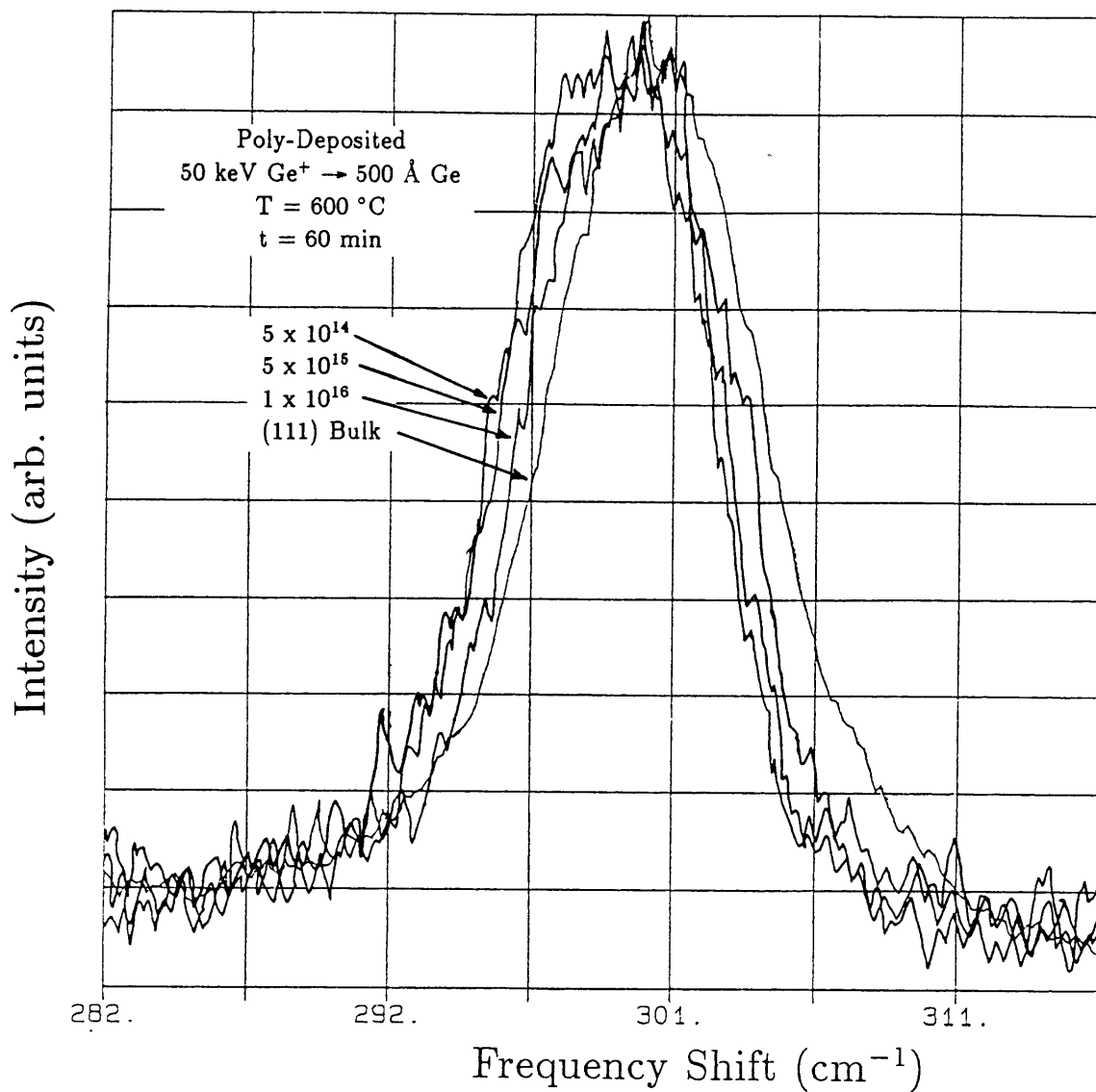
Figure 4.5: Raman spectra of polycrystalline-deposited films after ion beam enhanced grain growth at 600 °C
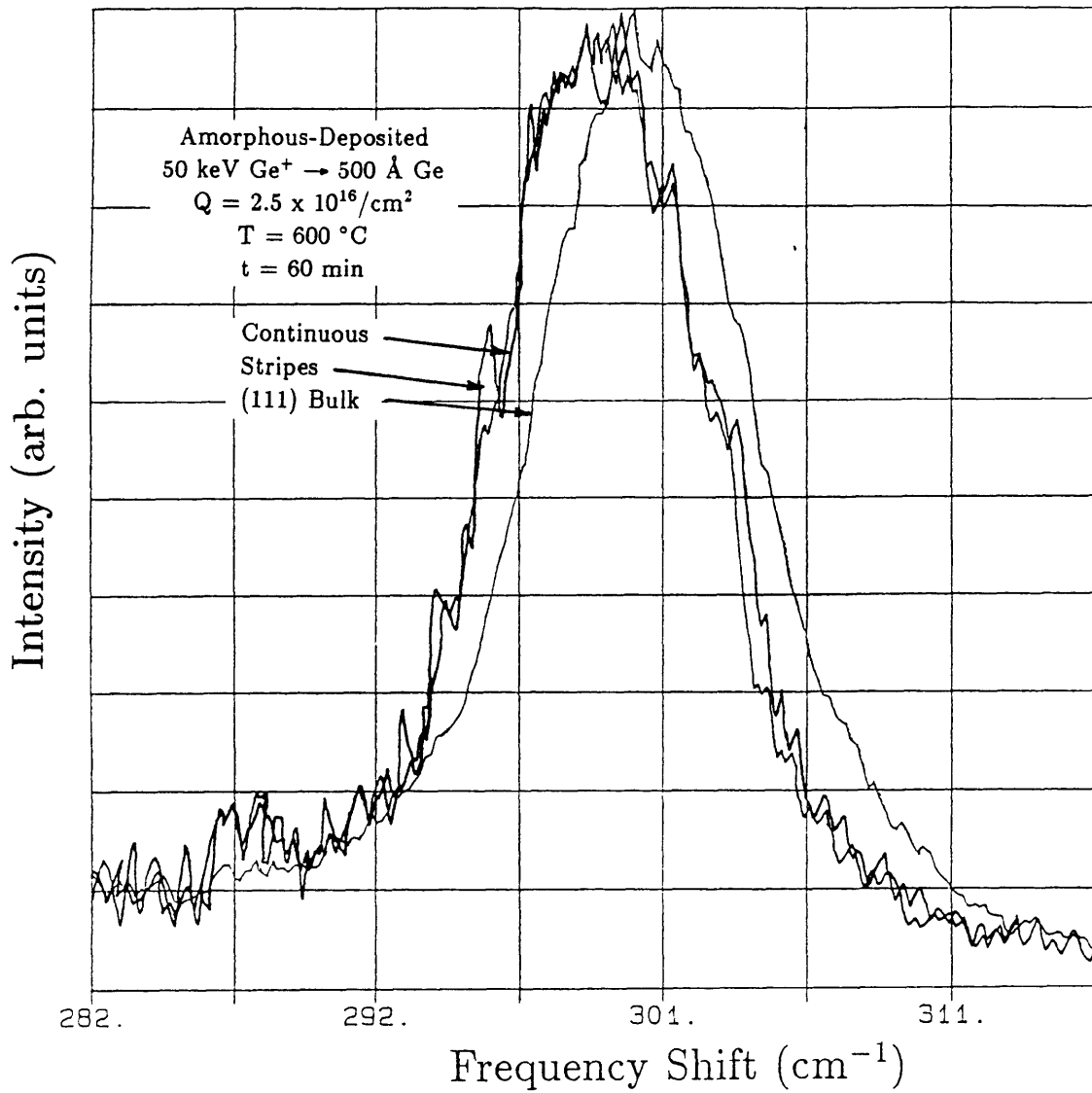
Figure 4.6: Raman spectra of patterned, amorphous-deposited films after ion beam enhanced grain growth at 600 °C

Sample	Raman Shift $< \Delta\Omega >$(cm^{-1})	Strain ϵ (10^{-3})	Stress σ (10^9 dynes/cm^2)
GE001	-1.7	-3.2	-4.4
GE002	-1.5	-2.9	-3.9
GE003	-0.6	-1.2	-1.7
GE007	-3.0	-5.7	-7.8
GE016	-2.2	-4.2	-5.7
GE017	-2.2	-4.2	-5.7
GE018	-1.9	-3.6	-4.9
GE004	-1.6	-3.0	-4.2
GE014	-2.8	-5.3	-7.3
GE015	-0.7	-1.3	-1.8
GE006	-1.6	-3.0	-4.2
GE009	-1.6	-3.0	-4.2
GE012	-1.5	-2.9	-3.9
GE008	-1.5	-2.7	-3.6
GE013	0	0	0

Table 4.3: Biaxial in-plane strain and stress for various 500 Å Ge films at room temperature

room temperature by Raman spectroscopy, ϵ, and the strain present in the film at the temperature for deposition, crystallization or grain growth, ϵ', where

$$\epsilon' = \epsilon - \epsilon_{te} \qquad (4.23)$$

The strain due to differential thermal expansion is

$$\epsilon_{te} = \alpha_{te}\Delta T \qquad (4.24)$$

where α_{te} is the difference in coefficients of thermal expansion between Si and Ge, and ΔT is the difference in temperature between the annealing temperature and the temperature of the Raman measurement. The values of strain, ϵ', and the corresponding stress at the annealing temperature, σ', are summarized in Table 4.5. The negative signs indicate tensile strain and stress, while the positive sign indicates compressive strain and stress.

Film Deposition Conditions

The results of Table 4.5 clearly indicate that films which are amorphous when deposited and subsequently crystallized are under greater tensile strain than films which are deposited in the polycrystalline form. In fact, the measured strain in the polycrystalline film at room temperature can be accounted for entirely by differential thermal expansion between the Ge film and the Si substrate. If the strain in the as-deposited amorphous film is assumed to be hydrostatic, this corresponds to a fractional volume change of 6×10^{-3}. This volume change presumably accompanied crystallization of the amorphous film.

Sample	Raman Shift $< \Delta \Omega >$ (cm^{-1})	Strain ϵ' 10^{-3}	Stress σ' (10^9 dynes/cm^2)
GE001	-1.7	-1.4	-1.9
GE002	-1.5	-1.1	-1.5
GE003	-0.6	+0.6	+0.8
GE007	-3.0	-3.9	-5.3
GE016	-2.2	-2.4	-3.3
GE017	-2.2	-2.4	-3.3
GE018	-1.9	-1.8	-2.5
GE004	-1.6	-1.2	-1.7
GE014	-2.8	-3.8	-5.2
GE015	-0.7	-0.1	-0.1
GE006	-1.6	-1.2	-1.7
GE009	-1.6	-0.7	-1.0
GE012	-1.5	-0.1	-0.1
GE008	-1.4	-0.4	-0.5

Table 4.4: Biaxial in-plane strain and stress for various 500 Å Ge films at the annealing temperature

Thermal Annealing

Thermal annealing results in an overall reduction in the stress present in thin Ge films. No significant change in stress is seen between samples annealed at 500 °C and 600 °C, for isochronal anneals. Between 600-750 °C and 750-910 °C, film stress decreases monotonically. Stress reduction presumably results from a thermally activated kinetic process. It is interesting to note that grain growth takes place over the same regime of temperature and time. Figure 4.7 is a plot of the change in average grain size, $r - r_o$, against the change in stress at the various annealing temperatures. Grain growth and reduction in film stress seem to be well correlated. This suggests that the mechanism for grain growth may be similar to the mechanism for reduction of film stress.

Ion Bombardment

The data of Table 4.5 indicate that film stress reduction accompanies ion beam enhanced grain growth as well as thermal grain growth. Figure 4.8 is a plot of stress variation with ion dose for amorphous-deposited and polycrystalline-deposited films during ion beam enhanced grain. It is seen, as noted above, that polycrystalline-deposited films are under smaller stress than the amorphous-deposited films. Amorphous-deposited films exhibit a monotonic decrease in stress with increasing ion dose. Polycrystalline-deposited films are at almost zero stress before ion bombardment. A small ion dose causes a tensile stress in the film. Further bombardment reduces the tensile stress, and eventually the stress goes from tensile to compressive.
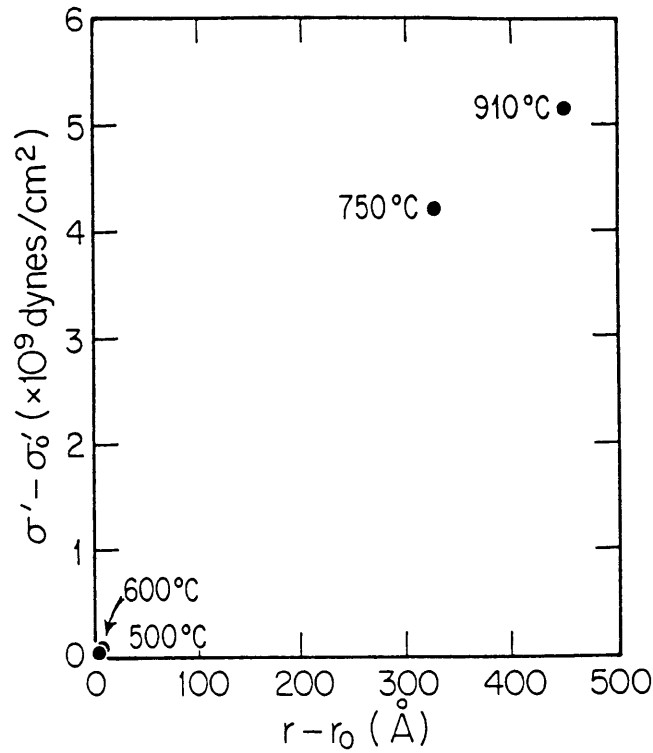
Figure 4.7: Change in stress at annealing temperature with change in grain size during thermal annealing

During ion beam enhanced grain growth, the grain size is a function of ion dose. Figure 4.9 depicts the change in stress with change in grain size for a amorphous-deposited film during ion beam enhanced grain growth. Comparison of Figs. 4.9 and 4.7 reveals that both thermal and ion beam enhanced grain growth are correlated with a reduction in stress. These results suggest that stress reduction is correlated with grain growth or a process which occurs simultaneously with grain growth.
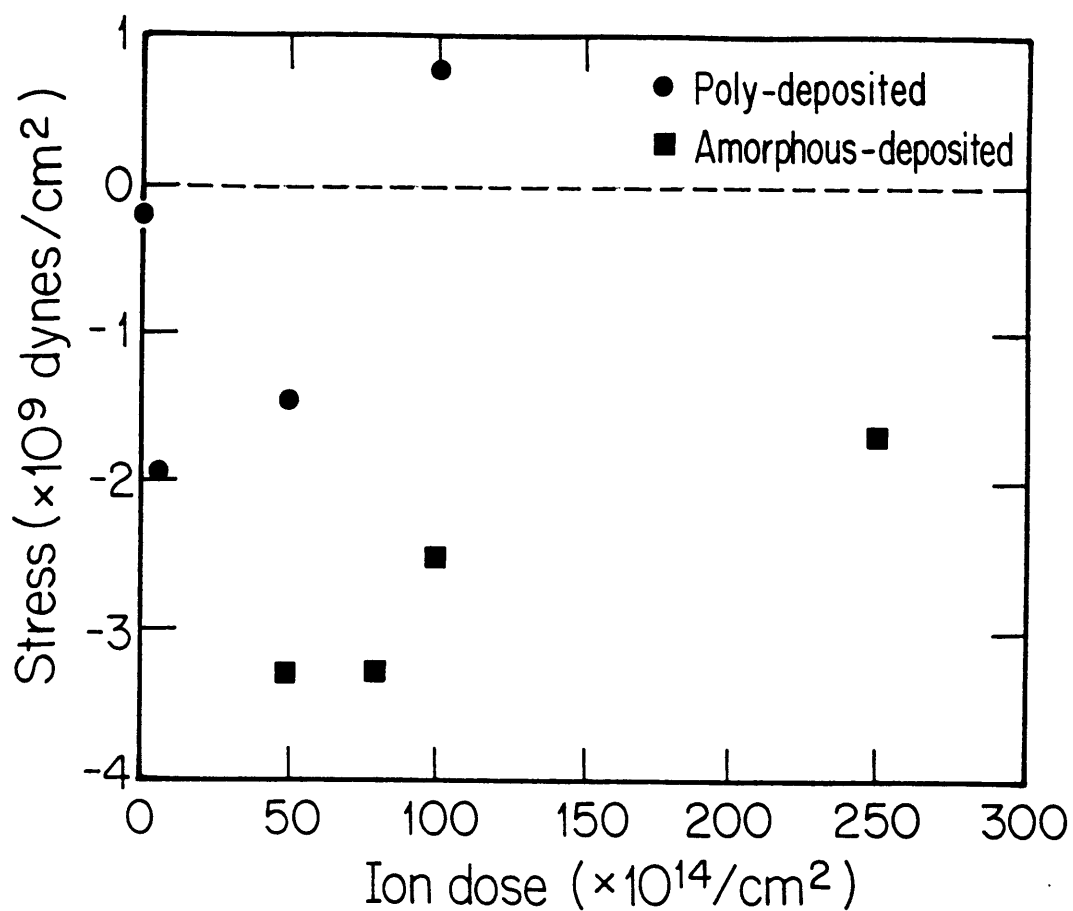
Figure 4.8: Variation in stress at 600 °C with ion dose during ion beam enhanced grain growth
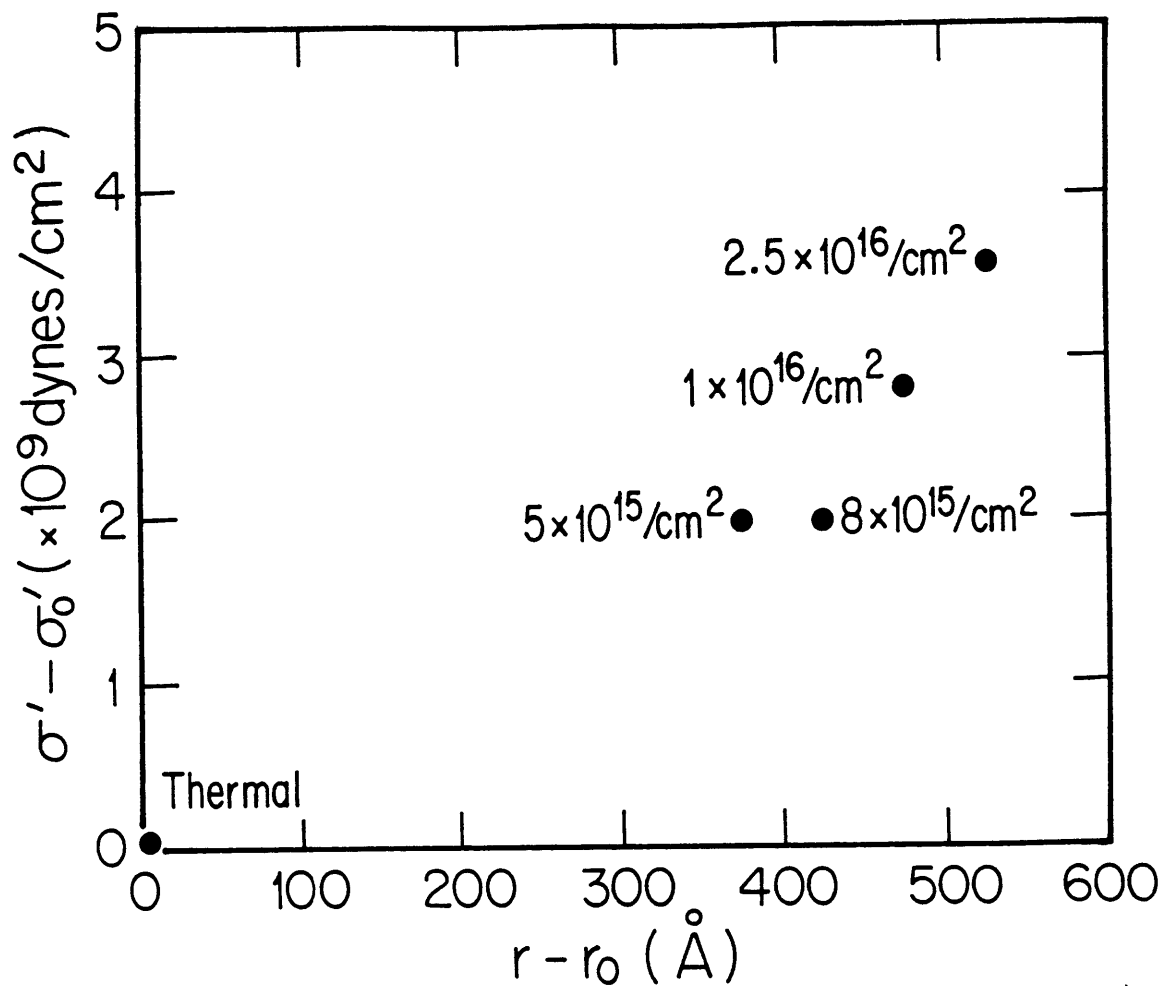
Figure 4.9: Change in stress with change in grain size during ion beam enhanced grain growth

4.6 Elastic Energy Density in Thin Films

Knowledge of the strain in the film allows the energy density due to strain to be calculated. Here the strain energy density will be assumed to equal the energy density of a homogeneous, elastically strained crystalline film. Implied in this assumption is the further assumption that all the stress in the polycrystalline films under consideration here is accommodated in elastic strain of the crystalline material within grains, and not strain at the grain boundaries. This assumption is made to simplify calculations and because the elastic constants of grain boundaries are not known.

The elastic energy density for a cubic crystal is [120]

$$U = \frac{1}{2}C_{11}[\epsilon_{xx}^2 + \epsilon_{yy}^2 + \epsilon_{zz}^2] + \frac{1}{2}C_{12}[\epsilon_{yy}\epsilon_{zz} + \epsilon_{xx}\epsilon_{zz} + \epsilon_{yy}\epsilon_{xx}] + \frac{1}{2}C_{44}[\epsilon_{yz}^2 + \epsilon_{zx}^2 + \epsilon_{xy}^2]$$

$$(4.25)$$

As before, we will assume that the polycrystalline film represents an average of (100) and (111) orientations, so

$$< U >= \frac{1}{2}U^{(100)} + \frac{1}{2}U^{(111)} \tag{4.26}$$

The expressions for $U^{(100)}$ and $U^{(111)}$ derived in Appendix B are

$$U^{(100)} = \frac{1}{S_{11} + S_{12}}\epsilon^2 \tag{4.27}$$

and

$$U^{(111)} = \frac{3}{2}[\frac{1}{S_{11} + 2S_{12}} + \frac{5}{8}\frac{1}{S_{44}}][(\frac{5}{2})^{\frac{1}{2}}\cos\theta_1 + \cos\theta_2]^{-2}\epsilon^2 \tag{4.28}$$

Substituting the appropriate values yields, for example, a strain energy density of $< U > = 1.78 \times 10^7$ ergs/cm^3 for sample GE007, the sample with the largest strain.

Now we can compare the driving force due to strain with estimates for the grain boundary energy and the surface energy. Consider a volume element of the 500 Å Ge film which spans the film thickness. Values for the surface energy, and grain boundary energy of Ge are not known, but they will be assumed to resemble typical values for metals [121]. If we assume a surface energy anisotropy (which is approximately 10 % of the surface energy) of 100 erg/cm^2, then the driving force due to surface energy is approximately 2×10^7 ergs/cm^3. The grain boundary energy is proportional to the grain size, or more properly, its curvature. If we assume a grain boundary energy of 500 erg/cm^2 [121], then for grain sizes of 100 - 1000 Å, estimates for grain boundary energy range from approximately 1×10^8 - 1×10^9 ergs/cm^3.

From these calculations, it appears that strain energy is comparable to the surface energy in our experiments, but that the grain boundary energy is 5 - 50 times larger. This would imply that grain boundary energy is the major driving force for transformation, and that strain reduction is a result rather than a significant cause of grain growth. The observation of random crystallographic texture in the films considered here is consistent with this conclusion, since surface energy and strain energy are orientation-dependent but grain boundary energy is assumed not to be orientation-dependent. Nonetheless, strain reduction is well correlated with grain growth, as seen above. These conclusions should be approached cautiously because the grain boundary energy of Ge is not known. If it is lower than typical values for metals, then strain energy, surface energy and grain boundary energy might be comparable.

Chapter 5

Discussion and Conclusions

5.1 Summary of Ion Beam Enhanced Grain Growth

This thesis research has introduced the phenomenon of ion beam enhanced grain growth. An experimental program was designed to test IBEGG by varying important physical parameters and assessing their effects on grain growth. A phenomenological theory of IBEGG was developed based on a transition state model for atomic motion at grain boundaries during ion bombardment. The model agrees with the experimental findings in the regime of observation.

5.1.1 Experiments

The major experimental findings about IBEGG are summarized:

1. The microstructure of thin films of Ge, Au and Si was monitored during IBEGG. Qualitatively, grain sizes increase as the ion doses are increased, and the films develop a columnar microstructure.

2. The density of dislocations is reduced in Ge and Si as a result of IBEGG, but in Au, the dislocation density is increased. It is believed that the difference in annealing temperatures accounts for the difference in dislocation densities.

3. Deep grooves form at grain boundaries in Ge films which have been bombarded with high ion doses (i.e., $\geq 1 \times 10^{16}/\text{cm}^2$). Grooving may retard grain growth in this regime.

4. For the three materials considered here, the distribution of grain sizes was approximately lognormal in all cases during IBEGG. As the ion dose is increased, the peaks of the lognormal distributions shift to larger grain size. This is consistent with previous experimental investigation of normal grain growth.

5. The variation of grain size with time was characterized for Ge, Au and Si films. The time dependence during IBEGG is similar for all three materials, and is consistent with previous studies of normal grain growth, but is inconsistent with existing models for normal grain growth.

6. The variation of grain size with temperature was measured for Ge and Si thin films during IBEGG. The activation energy for the rate-limiting step in grain boundary migration during IBEGG was approximately 0.15 eV for Ge and approximately 0.1 eV for Si. In both systems, the measured activation energy for the rate-limiting step during IBEGG is very low compared to the activation energy for thermal grain boundary migration, and is lower than measured or calculated values for point defect migration.

7. The variation of grain size with incident ion mass and energy has been studied for Ge, Au and Si films, using ions ranging from Ar^+ to Xe^+. The grain size is well correlated with calculations of the defect yield per incident ion performed with the TRIM code using a Kinchin-Pease algorithm.

8. Qualitative indications of the beginning of secondary grain growth were seen in Ge films implanted with high ion doses. In Au films, which exhibit surface energy-driven secondary grain growth during thermal annealing, normal grain growth appeared to continue to grain sizes much larger than the film thickness. The growth of Au films was characterized by monomodal grain size distributions and crystallographic texture which was weaker than that observed in thermally annealed Au films.

9. IBEGG was studied in Au films at different ion fluxes. The experiments indicate that IBEGG is a function of the incident ion dose and is independent of the ion flux. This and other direct evidence

indicated that the role of ion beam heating in grain growth was negligible.

5.1.2 The Model

1. The model developed for the IBEGG process is based on three postulates:

   (a) Only elastic collisions at or very near grain boundaries lead to enhanced grain growth. Defect migration from the interior of a grain to the boundary does not contribute to grain boundary motion.

   (b) Heating of the film by inelastic collisions, such as those due to electronic stopping and phonon production, are not important to enhanced grain growth.

   (c) During normal grain growth to a columnar structure, ion bombardment has a negligible influence on the driving force for grain growth. That is, the driving force during IBEGG is similar to the driving force during thermal annealing.

2. A transition state model for IBEGG was developed based on the postulates enumerated above. The model accounts for the dependence of IBEGG on temperature, ion dose, ion energy, ion mass and ion flux.

3. A atomistic picture of the jump rate at grain boundaries was developed. The number of atomic jumps at the grain boundary per defect

generated at the boundary for a given driving force was found to be approximately constant for each material. The results suggest that linear collision cascade theory can be used to describe ion bombardment in these experiments.

4. The IBEGG and thermal growth rates were related to their respective vacancy concentrations. It was noted that the grain growth rate was similar for both IBEGG and thermal growth when the vacancy concentrations were equal. It was proposed that grain growth is proportional to the point defect concentration at the grain boundary, regardless of whether the defects are generated thermally or by an ion beam.

5.2 Comparison with Other Ion Beam Enhanced Kinetic Processes

It is interesting to note the characteristics of other ion beam enhanced kinetic processes, such as diffusion and crystallization. A comparison of IBEGG with these other processes reveals some general traits common to solid-state kinetic phenomena during ion bombardment.

5.2.1   Ion Beam Enhanced Diffusion

Work on ion beam enhanced diffusion in semiconductors was undertaken well before studies of beam enhanced crystallization or grain growth[123,124,125]. Enhanced diffusion in metals has also been studied, during research on the development of nuclear reactor structural materials[126]. Some experiments focused on enhanced diffusion during thermal annealing following radiation damage by ion beams at room temperature[124,128]. Other studies were done of enhanced diffusion during concurrent ion bombardment at modest annealing temperatures(e.g., 600°C)[123,125,129]. Recently, enhanced diffusion has also been studied in Ge[127].

During typical ion beam enhanced diffusion (IBED) experiments, a shallow impurity profile was produced by thermal diffusion or ion implantation of B, P or As into Si[125,129]. This step was followed by light ion (e.g. H^+) implantation during thermal annealing at 600 °C. Enhanced impurity diffusion was observed in the region bombarded by light ions. The interesting features of the IBED process are summarized below:

1. Ion beam-generated point defects, which migrate along defect concentration gradients, are responsible for the observed diffusion enhancement.

2. More specifically, the diffusion coefficient of the substitutional impurity is proportional to the concentration of beam-generated point defects. A continuity equation can be written for the point defect concentration and the defect concentration profile can be calculated. The result of this analysis is a spatially varying diffusion coefficient

for the impurity. The measured impurity profiles matched well the profiles calculated using the proposed model for IBED[129,125].

3. Characteristic diffusion lengths were calculated for vacancies in Ge and Si at 600 °C[125,129].

4. The assertion was made that, in the regime where thermal annealing is negligible, IBED is limited only by the concentration of beam-generated point defects[125,129]. Unfortunately, the temperature dependence of IBED was not studied; if the activation energy of IBED had been measured, it could have been compared with point defect migration energies in Si to lend support to the proposed model.

5.2.2 Ion Beam Induced Crystallization

The ion beam induced crystallization (IBIC) of thin layers of amorphous semiconductors on crystalline substrates has been a topic of intensive research for the last decade. Early IBIC experiments were done using Ge substrates [130,131], followed by the demonstration of IBIC in Si[132]. Recently, intensive study of the IBIC process in Si has been carried out by two groups, one at Bell Labs and RMIT in Australia[133,134,135,136,137], and the other at Chalmers Institute of Technology in Sweden[138,139,140,141]. Typical experiments involve creating an amorphous layer approximately 1000 Å thick by ion implantation of Si^+ at low temperature, followed by annealing at 200-500 °C during ion bombardment with a noble gas ion beam. Analysis of the thickness of the regrowing amorphous layer is done

by channeling spectra in Rutherford backscattering spectrometry(RBS). The principal characteristic features of IBIC which have emerged are summarized:

1. The regrown layer thickness is proportional to the ion dose in the temperature range T = 200-400 °C. Above 400 °C, competing thermal effects complicate the characterization of regrowth.

2. More precisely, the regrown layer thickness is proportional to the energy deposited in nuclear collisions at, or very close to the amorphous-crystalline interface. The Bell group tested this idea with a experiment which varied the ion beam energy[135]. As the incident ion beam energy was increased, for a constant temperature and ion flux density, the regrowth rate decreased. This corresponds to an increased fraction of electronic energy deposition and a decreased fraction of nuclear energy deposition at the amorphous-crystalline interface, which is consistent with a regrowth rate proportional to the nuclear energy deposition.

3. The IBIC process is marked by a very weak temperature dependence. The activation energy for thermally-induced solid phase epitaxial regrowth of amorphous Si is known to be 2.7 eV[142]. By contrast, the activation energy for IBIC is ≈0.3 eV in the temperature range between 200-400 °C[135,139]. Above 400 °C, there appears to be a second IBIC regime characterized by an activation energy of 0.5 eV[135].

4. The detailed mechanism of beam-induced interfacial rearrangement is still unknown, and remains controversial. The Bell Labs group proposed that the rate-limiting step in interfacial motion is the generation of nucleation sites for crystallization at the interface[135]. This conclusion was based on experiments which showed a lack of dependence of the growth rate channeled or random beam alignment. Since a channeled beam results in nuclear energy deposition well beyond the region of the amorphous-crystalline interface under the conditions used, this implies that point defect migration from the crystalline bulk to the interface is not the limiting factor in IBIC. Also, unlike thermal epitaxial regrowth, there is no dependence of regrowth rate on the crystallographic orientation of the substrate. This was interpreted as evidence for beam generation of island nucleation sites at the amorphous-crystalline interface.

   To the contrary, the Chalmers group *did* find a dependence of the regrowth rate on beam channeling conditions, and thus proposed that point defects created in the crystalline region migrated to the amorphous-crystalline interface to enhance crystallization[139]. The IBIC activation energy of $\approx$ 0.3 eV was associated with the migration energy of a vacancy in Si. However, a defect diffusion length of $\approx$ 40 Å was calculated, which indeed implies that only defects created *very close* to the amorphous-crystalline interface contribute to IBIC.

5. The measured growth rate and the calculated defect yield using the Kinchin-Pease formula were used to estimate that the ratio of atomic

Characteristic	IBED	IBIC	IBEGG
Prop. to energy dep. in elastic collisions?	YES	YES	YES
Defect migration limiting kinetics?	YES	MAYBE	NO
Process weakly temp. dependent?	?	YES	YES
Process dependent on ion flux?	?	NO	NO

Table 5.1: Comparison of the characteristics of ion beam enhanced diffusion, ion beam enhanced crystallization, and ion beam enhanced grain growth.

jumps at the interface to the number of defects generated at the interface was $\approx$ 10 [135].

5.2.3 Common Aspects of Ion Beam Enhanced Kinetic Processes

Comparable characteristics of the three ion beam processes discussed here are summarized in Table summary. All three processes are functions of the energy density deposited in the form of elastic collisions. In ion beam enhanced diffusion, defect migration plays a role in determining the kinetic enhancement on a local scale. For IBIC, the results are ambiguous on the role of defect migration, and in IBEGG defect migration is apparently not important to the enhanced kinetics. Both IBIC and IBEGG have weak temperature dependences, and their thermal analogs are strongly temperature-dependent. Finally, both IBIC and IBEGG are independent of the ion flux, in appropriate temperature regimes.

5.3 Summary of Correlated Strain and Microstructural Observations

Raman spectroscopy was employed to measure the biaxial strain in thin Ge films. Strain was studied as a function of film deposition conditions, thermal annealing conditions, and IBEGG. The major results of this work are:

1. Strain (and hence stress) reduction is correlated with grain growth or with processes occurring simultaneously with grain growth for both thermal annealing and IBEGG.

2. Amorphous as-deposited films undergo a monotonic reduction in stress during IBEGG.

3. Polycrystalline as-deposited films are at nearly zero stress following deposition. When IBEGG begins, these films initially experience a tensile stress. As the ion dose is increased during IBEGG, the tensile stress diminishes, and at high doses, turns to compressive stress.

4. The energy due to strain in thin Ge films was calculated and compared to estimates of the surface energy and grain boundary energy in the films. The strain energy was found to be comparable to the surface energy in the grain size regime under study, but both were found to be much smaller than the grain boundary energy.

5.3.1 Future Work

The work described here represents a beginning of the study of ion beam enhanced grain growth. Many important scientific and technological questions remain.

Perhaps most intriguing is the question of whether the activation energies measured for IBEGG in Ge and Si are characteristic of the small energy barrier designated Q' in the model. The energy and ion mass dependences of IBEGG would seem to indicate that the rate of beam generation of defects, Δj, limits the overall jump rate, Δl. If this is true, then a question arises about the source of the activation energy, since in that case, the activation energy may not be associated with the small energy barrier Q'. Study of the dependence of IBEGG on ion flux may provide some insight.

Another important issue is the systematic assessment of the effects of grooving on grain growth. Recently, it has been suggested that grooving may act as an overall dragging force in grain growth, but may enhance the selection of a specific crystallographic texture[143]. In this work, grooving was observed in Ge films implanted with high ion doses. However, the fraction of the film composed of secondary grains at the highest doses used was too small to confirm or fail to confirm a preferred crystallographic texture. In Au films, surface energy driven secondary grain growth was *not* seen during IBEGG, but *is* seen during thermal annealing. This could be due to a texture selection via grooving during thermal anneals, which is absent during IBEGG because the film is not grooved. Study of grooving could be done in principle using XTEM, but would be difficult in practical

terms since the Au films are unsupported.

This work has shown that grain boundary mobilities are greatly en-
hanced above their respective thermal equilibrium values as a result of
IBEGG. However, no attempt was made in these experiments to maximize
the driving force for grain growth. It is clear that the driving force for
secondary grain growth due to surface energy anisotropy is maximized by
making the film as thin as possible. Therefore, studying IBEGG in thinner
films, using lower energy ion beams, represents an important direction for
future research. As the ion energy is lowered, however, the defect yield per
incident ion is lowered and the sputtering yield increases. Therefore, it may
be necessary to simultaneously deposit new material to compensate for that
lost due to sputtering during bombardment. One advantage of low energy
bombardment is that the reduced spatial extent of the damage profile leads
to better control of the location of ion beam energy deposition. When all
the the energy is deposited in the near surface region, it may be possible
to grow layers with very sharp compositional profiles, e.g., superlattices.
Finally, as the ion energy is lowered to values comparable to or less than
the diplacement energy, very interesting questions arise concerning what
effect a collision actually has on the kinetics in the thin film. In short,
this represents a very fruitful area for both future basic investigation and
development of low temperature growth processes for crystalline films.

In this work, it was shown that the grain boundary mobility is en-
hanced at or very near the point of defect generation. This finding presents
the intriguing possibility of *producing grain size distributions which depart
markedly from the naturally occurring lognormal distribution* by selective

ion bombardment of different parts of a film. A lithographically defined pattern could be devised to enhance grain growth in certain areas of the film and not in others. If these areas are comparable to the grain size, it may be possible to drastically alter the shape of grain size distributions.

Even more interesting are the possibilities presented by a focused ion beam tool. If the ion beam can be focused so as to bombard only a part of a given grain boundary, it may be possible to *"tailor" the shape of an individual grain boundary*, providing a suitable driving force for grain boundary motion exists. If the shapes of individual grain boundaries can be controlled by focused ion beam enhanced grain growth, many exciting kinetic and electronic experiments can be anticipated.

Appendix A

Cross-Sectional TEM

Preparation

Cross-sectional TEM specimen preparation was carried out using the facilities available at MIT. The linchpin of successful XTEM specimen preparation is dimpling, a technique which is used to mechanically polish a crater in the center of the specimen. Dimpling confers two principal benefits:

- There is a controllable, gradual variation in the thickness of the sample. Hence if a hole is created in the thinnest portion of the sample, the region immediately surrounding the hole provides ample area which is thin enough for electron transmission.

- The thick annular portion on the outer edge of the sample forms a sturdy support, which prevents breakage during sample handling.

A good review of cross-sectional TEM specimen preparation is found in Ref. [144] The procedure used to prepare samples at MIT is briefly outlined as follows:

1. Scribe and break the samples, which are on Si substrates, into 2 x 2 mm squares. This is done at MIT using the Tempress wafer scriber in 13-3028.

2. Cement two of the squares together face-to-face (so that the thin film regions of interest are contiguous) using epoxy. Immediately cement these into the slotted molybdenum holders[1] shown in Fig. A.1. Cement the copper sleeve onto the moly holder. Allow to dry for 24 hours.

3. Cut the rod into 1 mm thick disks using a low speed saw.

4. Glue the disks to a Gatan dimple grinder specimen mount using a low melting point wax. The wax supplied by Gatan can be easily melted on a hotplate and is soluble in acetone. Insert the mount into the Gatan Model 623 Disc Grinder. Polish the disks using No. 400 emery paper which has been wetted with water, polishing both sides and continuing until the sample thickness is 100-150 μm.

5. Remove the mount from the disk grinder, leaving the sample attached to the mount. Dimple the sample using the Gatan dimple grinder lo-

---

[1] These holder are machined from Mo rods. The diameter is approximately 2.6 mm and the slot is 1 mm wide. The copper tubing has an inside diameter of 2.6 mm and a 0.4 mm wall.

cated in Room 13-5147. Begin dimpling using the dimpling wheel and the 2.4 μm diamond paste polish. Dimple the first side until approximately one-third of the initial thickness is removed from the center of the sample. Dimple the other side until the sample is approximately 30 μm thick. Then dimple the sample to approximately 20 μm using 0-1 μm diamond paste polish. Remove the specimen from the specimen holder.

6. Ion mill the sample using the Gatan Dual Ion Mill in 13-1028 at a ion beam incidence angle of 15°. Continue ion milling until the sample is optically transparent in the region of interest, as viewed in an optical microscope. Ion mill just a bit more until a small hole is formed in the center of the sample. View the sample in the TEM, and continue ion milling as necessary.
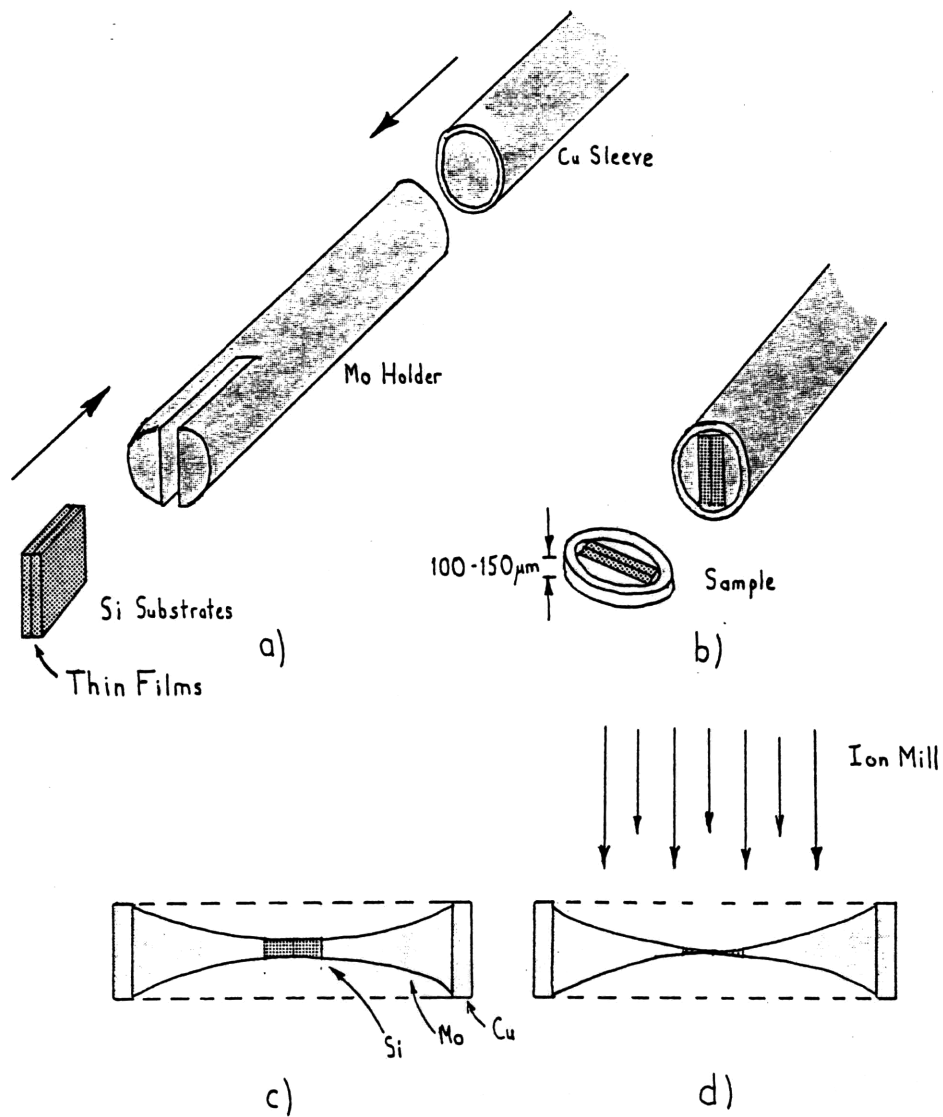
Figure A.1: Steps in cross-sectional TEM specimen preparation. In a) the samples is cemented into the holder; in b) it is cut and polished; in c) the sample is cemented to the holder; in d) dimpling is performed; in e) final thinning is done by ion milling.

Appendix B

Ion Beam Heating

The energy dissipated by the ion beam which does not contribute to damage through elastic collisions results in heating of the film. In principal, the rise in temperature from ion beam heating could result in annealing of the film[145]. We now calculate the temperature rise in a typical film employed in the present experiments. The film is 500 Å of Ge on 1000 Å of SiO_2 all on a 300 μm thick Si wafer which is in thermal contact with the stage. The ion beam is assumed to be a 50 keV Ge^+ beam with a current density of 0.25 $\mu A/cm^2$. We will assume a "worst case" in which all of the power of the ion beam contributes to heating of the film, although TRIM calculations indicate that only a fraction of the beam power results in heating. The thermal conductivities of Ge, SiO_2, and Si are 0.6 W/cm-K, 0.014 W/cm-K and 1.5 W/cm-K, respectively[146]. The heat flux

density, Φ, is considered to be equal to the ion beam power density

$$\Phi = EJ \tag{B.1}$$

where E is the ion beam energy and J is the beam current density. The flux density is related to the temperature gradient in one dimension by

$$\Phi = k\frac{dT}{dz} \tag{B.2}$$

where k is the thermal conductivity. For uniform media, this can be rewritten as

$$\Delta T = \frac{\Phi}{k}\Delta z \tag{B.3}$$

The total temperature drop from the Ge film to the stage is then

$$\Delta T = EJ\left(\frac{\Delta z_{Si}}{k_{Si}} + \frac{\Delta z_{SiO_2}}{k_{SiO_2}}\right) \tag{B.4}$$

Using the numbers given above results in a temperature rise of ΔT = 2.4 x 10^{-4} °C.

Appendix C

Strain Dependent Raman

Frequency

C.1   Biaxial Stress-Strain Relations

The generalization of Hooke's law to relate an arbitrary strain to an arbitrary stress is

$$
\begin{pmatrix} \sigma_{xx} \\ \sigma_{yy} \\ \sigma_{zz} \\ \sigma_{yz} \\ \sigma_{zx} \\ \sigma_{xy} \end{pmatrix} = \begin{pmatrix} C_{11} & C_{12} & C_{13} & C_{14} & C_{15} & C_{16} \\ C_{21} & C_{22} & C_{23} & C_{24} & C_{25} & C_{26} \\ C_{31} & C_{32} & C_{33} & C_{34} & C_{35} & C_{36} \\ C_{41} & C_{42} & C_{43} & C_{44} & C_{45} & C_{46} \\ C_{51} & C_{52} & C_{53} & C_{54} & C_{55} & C_{56} \\ C_{61} & C_{62} & C_{63} & C_{64} & C_{65} & C_{66} \end{pmatrix} \begin{pmatrix} \epsilon_{xx} \\ \epsilon_{yy} \\ \epsilon_{zz} \\ \epsilon_{yz} \\ \epsilon_{zx} \\ \epsilon_{xy} \end{pmatrix}
\tag{C.1}
$$

For cubic crystals symmetry reduces this tensor to

$$
\begin{pmatrix} \sigma_{xx} \\ \sigma_{yy} \\ \sigma_{zz} \\ \sigma_{yz} \\ \sigma_{zx} \\ \sigma_{xy} \end{pmatrix} = \begin{pmatrix} C_{11} & C_{12} & C_{12} & 0 & 0 & 0 \\ C_{12} & C_{11} & C_{12} & 0 & 0 & 0 \\ C_{12} & C_{12} & C_{11} & 0 & 0 & 0 \\ 0 & 0 & 0 & C_{44} & 0 & 0 \\ 0 & 0 & 0 & 0 & C_{44} & 0 \\ 0 & 0 & 0 & 0 & 0 & C_{44} \end{pmatrix} \begin{pmatrix} \epsilon_{xx} \\ \epsilon_{yy} \\ \epsilon_{zz} \\ \epsilon_{yz} \\ \epsilon_{zx} \\ \epsilon_{xy} \end{pmatrix}
\tag{C.2}
$$

C.1.1   Biaxial Stress-Strain Relations for (100) Crystals

In a (100) crystal, the film is not restrained in the z direction [1], so

$$
\sigma_{zz} = 0
\tag{C.3}
$$

Since this film is under biaxial strain, the in-plane components are equal

$$
\sigma_{xx} = \sigma_{yy} = \sigma
\tag{C.4}
$$

---

[1] Here x,y, and z are referred to the {100} crystallographic directions

$$\epsilon_{xx} = \epsilon_{yy} = \epsilon \qquad \text{(C.5)}$$

Also, for biaxial strain there are no shear components of strain, so

$$\epsilon_{yz} = \epsilon_{zz} = \epsilon_{xy} = 0 \qquad \text{(C.6)}$$

Therefore, the stress-strain relations reduce to

$$\sigma_{xx} = C_{11}\epsilon_{xx} + C_{12}\epsilon_{xx} + C_{12}\epsilon_{zz} \qquad \text{(C.7)}$$

$$0 = C_{12}\epsilon_{xx} + C_{12}\epsilon_{xx} + C_{11}\epsilon_{zz} \qquad \text{(C.8)}$$

Combining gives

$$\epsilon_{zz} = -\frac{2C_{12}}{C_{11}}\epsilon_{xx} \qquad \text{(C.9)}$$

The tetragonal distortion ϵ_T is

$$\epsilon_T = \epsilon_{zz} - \epsilon_{xx} = -[\frac{2C_{12}}{C_{11}} + 1]\epsilon_{xx} = -[\frac{1+\nu}{1-\nu}]\epsilon_{xx} \qquad \text{(C.10)}$$

where ν is Poisson's ratio. From above,

$$\sigma = [C_{11} + C_{12} - 2\frac{C_{12}^2}{C_{11}}]\epsilon_{xx} \qquad \text{(C.11)}$$

$$\epsilon_{xx} = \frac{C_{11}}{C_{11}^2 + C_{12}C_{11} - 2C_{12}^2}\sigma = \frac{C_{11}}{(C_{11} + 2C_{12})(C_{11} - C_{12})}\sigma \qquad \text{(C.12)}$$

$$\epsilon_{xx} = \frac{1}{C_{11}(1 + \frac{2C_{12}}{C_{11}})(1 - \frac{C_{12}}{C_{11}})}\sigma \qquad \text{(C.13)}$$

The elastic compliances, S_{ij}, are related to the elastic stiffness constants in a cubic system by [122]

$$C_{11} = \frac{S_{11} + S_{12}}{(S_{11} - S_{12})(S_{11} + 2S_{12})} \qquad \text{(C.14)}$$

$$C_{12} = \frac{-S_{12}}{(S_{11} - S_{12})(S_{11} + 2S_{12})} \qquad \text{(C.15)}$$

$$C_{44} = \frac{1}{S_{44}} \qquad\qquad (C.16)$$

so the in-plane strain is then

$$\epsilon_{xx} = \frac{(S_{11} - S_{12})(S_{11} + 2S_{12})}{S_{11} + S_{12}} \frac{\sigma}{(1 - \frac{2S_{12}}{S_{11}+S_{12}})(1 + \frac{S_{12}}{S_{11}+S_{12}})} \qquad (C.17)$$

$$\epsilon_{xx} = \frac{(S_{11} - S_{12})(S_{11} + 2S_{12})(S_{11} + S_{12})^2}{(S_{11} + S_{12})(S_{11} - S_{12})(S_{11} + 2S_{12})}\sigma \qquad (C.18)$$

$$\epsilon_{xx} = (S_{12} + S_{12})\sigma \qquad\qquad (C.19)$$

and

$$\epsilon_{zz} = 2S_{12}\sigma \qquad\qquad (C.20)$$

C.1.2 Biaxial Stress-Strain Relations for (111) Crystals

For a (111)-textured crystalline thin film, biaxial strain requires

$$\epsilon_{xx} = \epsilon_{yy} = \epsilon_{zz} \qquad\qquad (C.21)$$

and the requirement of no net torque yields

$$\epsilon_{xz} = \epsilon_{zx} = \epsilon_{xy} = \epsilon_{yx} = \epsilon_{yz} = \epsilon_{zy} \qquad (C.22)$$

Similarly,

$$\sigma_{xx} = \sigma_{yy} = \sigma_{zz} \qquad\qquad (C.23)$$

The stress-strain relations reduce to

$$\sigma_{xx} = (C_{11} + 2C_{12})\epsilon_{xx} \qquad\qquad (C.24)$$

$$\sigma_{yz} = C_{44}\epsilon_{yz} \tag{C.25}$$

or

$$\epsilon_{xx} = (S_{11} + 2S_{12})\sigma_{xx} \tag{C.26}$$

$$\epsilon_{yz} = S_{44}\sigma_{yz} \tag{C.27}$$

C.2 Raman-Strain Relations

In cubic crystals, the Raman-strain relations reduce to the secular equation[117]

$$
\begin{vmatrix}
p\epsilon_{xx} + q(\epsilon_{yy} + \epsilon_{zz}) - \lambda & 2r\epsilon_{xy} & 2r\epsilon_{xz} \\
2r\epsilon_{xy} & p\epsilon_{yy} + q(\epsilon_{xx} + \epsilon_{zz}) - \lambda & 2r\epsilon_{yz} \\
2r\epsilon_{xz} & 2r\epsilon_{yz} & p\epsilon_{zz} + q(\epsilon_{xx} + \epsilon_{yy}) - \lambda
\end{vmatrix} = 0 \tag{C.28}
$$

where

$$\lambda = \Omega^2 - \omega_o^2 \tag{C.29}$$

The parameter Ω is the strain-dependent Raman frequency and ω_o is the frequency in the absence of strain. The above can be approximated as

$$\Omega \approx \omega_o + \frac{\lambda}{2\omega_o} \tag{C.30}$$

C.2.1   Strain-Raman Relations for a (100) Crystal

Since the shear components of strain vanish and the in-plane components are equal, the secular equation reduces to

$$[(p+q)\epsilon_{xx} + q\epsilon_{zz} - \lambda][(p+q)\epsilon_{xx} + q\epsilon_{zz} - \lambda][p\epsilon_{zz} + 2q\epsilon_{xx} - \lambda] = 0 \quad (C.31)$$

Hence there are two solutions. The singlet solution is

$$\lambda_s^{(100)} = p\epsilon_{zz} + 2q\epsilon_{xx} = 2pS_{12}\sigma + 2q(S_{11} + S_{12})\sigma \quad (C.32)$$

so

$$\Omega_s^{(100)} = \omega_o + \frac{\sigma}{2\omega_o}[2pS_{12} + 2q(S_{11} + S_{12})] \quad (C.33)$$

The doublet solution is

$$\lambda_d^{(100)} = (p+q)\epsilon_{xx} + q\epsilon_{zz} = (p+q)(S_{11} + S_{12})\sigma + 2qS_{12}\sigma \quad (C.34)$$

$$\Omega_d^{(100)} = \omega_o + \frac{\sigma}{2\omega_o}[p(S_{11} + S_{12}) + q(S_{11} + 3S_{12})] \quad (C.35)$$

C.2.2   Strain-Raman Relations for a (111) Crystal

In a (111) textured film, the secular equation becomes

$$\begin{vmatrix} (p+2q)\epsilon_{xx} - \lambda & 2r\epsilon_{yz} & 2r\epsilon_{yz} \\ 2r\epsilon_{yz} & (p+2q)\epsilon_{xx} - \lambda & 2r\epsilon_{yz} \\ 2r\epsilon_{yz} & 2r\epsilon_{yz} & (p+2q)\epsilon_{xx} \end{vmatrix} = 0 \quad (C.36)$$

which reduces to

$$\lambda^{(111)} = (p + 2q)\epsilon_{zz} + 4r\epsilon_{yz} \qquad (C.37)$$

or, in terms of the stress,

$$\lambda^{(111)} = (p + 2q)(S_{11} + 2S_{12})\sigma_{zz} + 4rS_{44}\sigma_{yz} \qquad (C.38)$$

Consider the rotated coordinate system of Fig. A.1 [2]. The condition of no net stress normal to the plane of the film requires

$$\sigma_{zz}\sin\theta_1 = 2\sigma_{xy}\sin\theta_2 \qquad (C.39)$$

where θ_1 is the angle between the direction of ϵ_{zz} and the plane, and θ_2 is the angle between the direction of ϵ_{xy} and the plane. Geometrical considerations can be used to show that

$$\frac{\sigma_{zz}}{\sigma_{xy}} = 2(\frac{2}{5})^{\frac{1}{2}} \qquad (C.40)$$

and that the angles are $\theta_1 = 35.2°$ and $\theta_2 = 65.9°$. The in-plane stress, σ, is

$$\sigma = 2\sigma_{xy}\cos\theta_2 + \sigma_{zz}\cos\theta_1 \qquad (C.41)$$

$$\sigma = [(\frac{5}{2})^{\frac{1}{2}}\cos\theta_2 + \cos\theta_1]\sigma_{zz} \qquad (C.42)$$

Hence, combining these relations yields

$$\lambda^{(111)} = [(p + 2q)(S_{11} + 2S_{12}) + 4rS_{44}\frac{1}{2}(\frac{5}{2})^{\frac{1}{2}}]\sigma_{zz} \qquad (C.43)$$

---

[2]The coordinates x, y, and z are still referred to {100} directions, but since (111) planes are parallel to the film, the coordinate system is rotated with respect to the film.
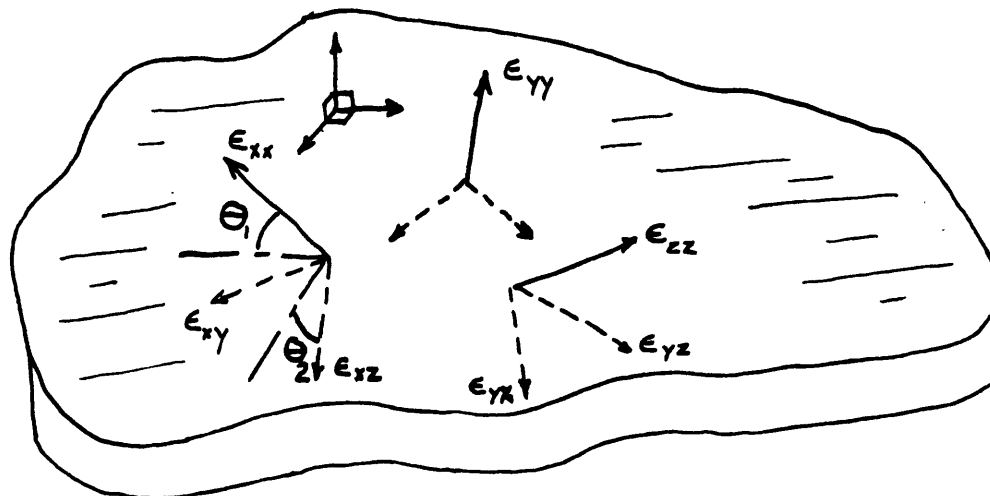
Figure C.1: Components of strain in a (111) textured film. The coordinate system is referred to the {100} directions.

$$\lambda^{(111)} = \frac{1}{[(\frac{5}{2})^{\frac{1}{2}} \cos\theta_2 + \cos\theta_1]}[(p + 2q)(S_{11} + 2S_{12}) + 2rS_{44}(\frac{5}{2})^{\frac{1}{2}}]\sigma$$

$$(C.44)$$

Finally,

$$\Omega^{(111)} = \omega_o + \frac{1}{2\omega_o[(\frac{5}{2})^{\frac{1}{2}} \cos\theta_2 + \cos\theta_1]}[(p+2q)(S_{11}+2S_{12})+2rS_{44}(\frac{5}{2})^{\frac{1}{2}}]\sigma$$

$$(C.45)$$

C.3   Strain Energy Density

The elastic energy density, U, for a cubic crystal is [120]

$$U = \frac{1}{2}C_{11}(\epsilon_{xx}^2+\epsilon_{yy}^2+\epsilon_{zz}^2)+C_{12}(\epsilon_{yy}\epsilon_{zz}+\epsilon_{zz}\epsilon_{xx}+\epsilon_{xx}\epsilon_{yy})+\frac{1}{2}C_{44}(\epsilon_{yz}^2+\epsilon_{zx}^2+\epsilon_{xy}^2)$$

$$(C.46)$$

C.3.1   (100) Crystal

Since the shear components vanish in a (100) crystal, and $\epsilon_{xx} = \epsilon_{yy}$, the elastic energy density reduces to

$$U^{(100)} = \frac{1}{2}C_{11}(2\epsilon_{xx}^2 + \epsilon_{zz}^2) + C_{12}(2\epsilon_{xx}\epsilon_{zz} + \epsilon_{xx}^2) \qquad (C.47)$$

$$U^{(100)} = (C_{11} + C_{12})\epsilon_{xx}^2 + \frac{1}{2}C_{11}\epsilon_{zz}^2 + 2C_{12}\epsilon_{xx}\epsilon_{zz} \qquad (C.48)$$

recalling that $\epsilon_{zz} = -\frac{C_{12}}{C_{11}}\epsilon_{xx}$, we obtain

$$U^{(100)} = (C_{11} + C_{12})\epsilon_{xx}^2 + \frac{1}{2}C_{11}[\frac{4C_{12}^2}{C_{11}^2}]\epsilon_{xx}^2 - [\frac{4C_{12}^2}{C_{11}}]\epsilon_{xx}^2 \qquad (C.49)$$

$$U^{(100)} = [C_{11} + C_{12} - \frac{2C_{12}}{C_{11}}]\epsilon_{xx}^2 \qquad (C.50)$$

In terms of elastic compliances, this is

$$U^{(100)} = \frac{1}{S_{11} + S_{12}}\epsilon_{xx}^2 \qquad (C.51)$$

C.3.2   (111) Crystal

$$U^{(111)} = \frac{3}{2}C_{11}\epsilon_{xx}^2 + 3C_{12}\epsilon_{xx}^2 + \frac{3}{2}C_{44}\epsilon_{xy}^2 \qquad (C.52)$$

$$\frac{3}{2}[(C_{11} + 2C_{12})\epsilon_{xx}^2 + C_{44}\epsilon_{xy}^2] \qquad (C.53)$$

$$\frac{3}{2}[\frac{1}{(S_{11} + 2S_{12})}\epsilon_{xx}^2 + \frac{1}{S_{44}}\epsilon_{xy}^2] \qquad (C.54)$$

The strain parallel to the substrate, ϵ, is

$$\epsilon = [(\frac{5}{2})^{\frac{1}{2}}\cos\theta_1 + \cos\theta_2]\epsilon_{xx} \qquad (C.55)$$

From geometry, as before,

$$\frac{\epsilon_{xx}}{\epsilon_{xy}} = 2(\frac{2}{5})^{\frac{1}{2}} \qquad (C.56)$$

so the energy density is

$$U^{(111)} = \frac{3}{2}[\frac{1}{S_{11} + 2S_{12}} + \frac{5}{8}\frac{1}{S_{44}}]\epsilon_{xx}^2 \qquad (C.57)$$

$$U^{(111)} = \frac{3}{2}[\frac{1}{S_{11} + 2S_{12}} + \frac{5}{8}\frac{1}{S_{44}}][(\frac{5}{2})^{\frac{1}{2}}\cos\theta_1 + \cos\theta_2]^{-2}\epsilon^2 \qquad (C.58)$$

Bibliography

[1] H.A. Atwater, H.I. Smith and C.V. Thompson, in "Energy Beam-Solid Interactions and Phase Transformations", Symposium A, MRS Fall Meeting, 1985.

[2] H.A. Atwater, C.V. Thompson and H.I. Smith, in "Beam-Solid Interactions and Phase Transformations", Symposium A, MRS Fall Meeting, 1986.

[3] This thesis work.

[4] P. Wang, D.A. Thompson and W.W. Smeltzer, Nucl. Instrum. Meth., B16, 288 (1986).

[5] J.C. Liu and J.W. Mayer, Nucl. Instrum. Meth., B19, 538 (1987).

[6] P. Feltham, Acta. Metall., 5, 97 (1957).

[7] M. Hillert, Acta. Metall., 13, 227 (1965).

[8] N.P. Louat, Acta. Metall., 22, 721 (1974).

[9] W.W. Mullins, J. Appl. Phys., 28, 333 (1957).

[10] J.L. Walter and C.G. Dunn, Trans. A.I.M.E., **215**, 465 (1959).

[11] W.A. Miller and W.M. Williams, J. Inst. Metals, **93**, 123 (1964).

[12] A. Gangulee and F.M. D'Heurle, Thin Solid Films, **12**, 399 (1972).

[13] J.E. Palmer, S.M. Thesis, MIT, 1985.

[14] C.V. Thompson and H.I. Smith, Appl. Phys. Lett., **44**, 603 (1984).

[15] H-J. Kim and C.V. Thompson, Appl. Phys. Lett., **48**, 399 (1986).

[16] C.C. Wong, Ph.D. Thesis, MIT, 1986.

[17] C.V. Thompson, J. Appl. Phys., **58**, 763 (1985).

[18] C.V. Thompson, H.J. Frost and F. Spaepen, Acta Metall., to be published.

[19] G.E. Thomas, L.J. Beckers, J.J. Vrakking and B.R. De Koning, J. Crystal Growth, **56**, 557 (1975).

[20] N. Herbots, B.R. Appleton, T.S. Noggle, R.A. Zuhr and S.J. Pennycook, Nucl. Instrum. Meth., **B13**, 250 (1986).

[21] N. Herbots, B.R. Appleton, S.J. Pennycook, T.S. Noggle and R.A. Zuhr, Mat. Res. Soc. Symp. Proc., **51**, 369 (1986).

[22] J.M.E. Harper, J.J. Cuomo, R.J. Gambino and Harold R. Kaufman, Chapter 4 in **Ion Bombardment Modification of Surfaces: Fundamentals and Applications**, Elsevier, Amsterdam, 1981.

[23] J.F. Ziegler, J.P. Biersack, and U. Littmark, **The Stopping and Range of Ions in Solids**, Pergamon Press, New York, 1986.

[24] G. Carter and W.A. Grant, **Ion Implantation of Semiconductors**, Edward Arnold, London, 1976.

[25] J.W. Mayer, L. Eriksson and J.A. Davies, **Ion Implantation of Semiconductors**, Stanford University Press, 1970.

[26] D.A. Thompson, Rad. Effects, **56**, 105 (1981).

[27] J.A. Davies, in "Ion Implantation an Beam Processing", J.S. Williams and J.M. Poate eds., Academic Press, New York, 1984, pp 81-97.

[28] W.L. Brown in "Beam-Solid Interactions and Phase Transformations", H. Kurz, G.L. Olson, and J.M. Poate, eds., Materials Research Society, Pittsburgh, PA, 1986, p. 53.

[29] N. Bohr, Matt Fys Medd Kgl Danske Videnskab Selskab, **18**, 8 (1948).

[30] J.F. Ziegler, J.P. Biersack, and U. Littmark, **The Stopping and Range of Ions in Solids**, Pergamon Press, New York, 1986, pp. 41-65.

[31] M. Born and J.E. Mayer, Z. Phys., **75**, 1 (1932).

[32] O.B. Firsov, Zh. Eksp. Theor. Fiz. **32**, 1464 (1957).

[33] A.A. Abrahamson, Phys. Rev. **133**, 693 (1963).

[34] J. Linhard, M. Scharff and H.E. Schiøtt, Matt Fys Medd Kgl Danske Videnskab Selskab, **33**, 14 (1963).

[35] K.B. Winterbon, P. Sigmund, J.B. Sanders, Matt Fys Medd Kgl Danske Videnskab Selskab, **37**, 14 (1970).

[36] A. Sommerfeld, Z. Phys. **78**, 283 (1932).

[37] G. Molière, Z. Naturforsch. **A2**, 133 (1947).

[38] W. Lenz, Z. Phys. **77**, 713 (1932).

[39] H. Jensen, Z. Phys. **77**, 722 (1932).

[40] M.T. Robinson and O.S. Oen, Phys. Rev. **132**, 2385 (1963).

[41] O.S. Oen and M.T. Robinson, J. Appl. Phys., **35**, 2515 (1964).

[42] J.P. Biersack and L.G. Haggmark, Nucl. Instrum. and Methods **174**, 257 (1980).

[43] O.B. Firsov, Zh. Eksp. Theor. Fiz. **36**, 1517 (1959).

[44] J. Linhard and A. Winther, Matt Fys Medd Kgl Danske Videnskab Selskab, **34**, 4 (1964).

[45] J.F. Gibbons, W.S. Johnson, and S.W. Mylroie, **Projected Range Statistics**, Douden, Hutchinson and Ross, Stroudsburg, Pa., 1975.

[46] M.I. Current and D.N. Seidman, Nucl. Instrum. and Methods, **170**, 377 (1980).

[47] J.A. Hudson, and B. Ralph, "Atomic Collision Phenomena in Solids", D.W. Palmer, M.W. Thompson and P. Townsend eds, North Holland, 1970, p. 85.

[48] D.N. Seidman in "Radiation Damage in Metals", N.L. Peterson and S.D. Harkness eds., American Society for Metals, (1976) p. 28.

[49] C.A. English, B.L. Eyre, and M.L. Jenkins, Nature, **263**, 400 (1976).

[50] M.O. Ruault, J. Chaumont, H. Bernas and P. Sigmund, Phys. Rev. Letters, **36**, 1148 (1976).

[51] M.W. Thompson, **Defects and Radiation Damage in Metals**, Cambridge University Press, Cambridge, 1969.

[52] A. Seeger and K.P. Chik, Phys. Stat. Sol., **29**, 455 (1968).

[53] K.H. Bennemann, Phys. Rev., **130**, 1763 (1963).

[54] R.R. Hasiguti, J. Phys. Soc. Japan, **21**, 1927 (1966).

[55] R.A. Swalin, J. Phys. Chem. Solids, **18**, 290 (1961).

[56] F. Seitz, Discuss. Faraday Soc., **5**, 271 (1949).

[57] R. Baurlein, **Radiation Damage in Solids**, Academic Press, New York, 1962, p. 358.

[58] P. Sigmund, Appl. Phys. Lett., **14**, 114 (1969).

[59] R.B. Iverson, private communication.

[60] F.F. Morehead and B.L. Crowder in "First International Conference on Ion Implantation", Thousand Oaks, Gordon and Breach, New York, 1971, p. 25.

[61] J.B. Gibson, A.N. Goland, M. Milgram and G.H. Vineyard, Phys. Rev., **120**, 1229 (1960).

[62] A. Sosin, Phys. Rev., **126**, 1698 (1962).

[63] C. Erginsoy, G.H. Vineyard and A. Englert, Phys. Rev., **133A**, 595 (1964).

[64] G.G. George and E.M. Gunnersen in "VII International Conference on the Physics of Semiconductors", Dunod, Paris, 1964, p. 385.

[65] G.H. Kinchin and R.S. Pease, Rep. Prog. Phys., **18**, 1 (1955).

[66] G.H. Kinchin and R.S. Pease, J. Nucl. Energy, **1**, 200 (1955).

[67] J.B. Sanders, Physica, **32**, 2197 (1966).

[68] P. Sigmund and J.B. Sand in "Proceedings of the International Conference on Applications of Ion Beams to Semiconductor Technology", Edition Ophrys, 1967, p. 215.

[69] J. Linhard, V. Nielsen and M. Scharff, Matt Fys Medd Kgl Danske Videnskab Selskab, **36**, 10 (1968).

[70] K.B. Winterbon, Rad. Effects, **13**, 215 (1972).

[71] D.K. Brice, Rad. Effects, **11**, 227 (1971).

[72] J.A. Brinkman, J. Appl. Phys., **25**, 961 (1954).

[73] J.A. Brinkman, Amer. J. Phys., **24**, 246 (1956).

[74] D.A. Thompson and R.S. Walker, Rad. Effects, **36**, 91 (1978).

[75] P. Sigmund, Appl. Phys. Lett., **25**, 169 (1974).

[76] M.O. Thompson and G.J. Galvin in "Laser-Solid Interactions and Transient Thermal Processing of Materials", J. Narayan,

W.L. Brown and R.A. Lemons eds., North Holland, New York, 1983, p. 3.

[77] L.M. Howe and M.H. Rainville, H.K. Haugen and D.A. Thompson, Nucl. Instrum. and Methods **170**, 419 (1980).

[78] L.M. Howe and M.H. Rainville, Nucl. Instrum. and Methods, **182/183**, 143 (1981).

[79] R.S. Walker and D.A. Thompson, Rad. Effects, **37**, 113 (1978).

[80] D.A. Thompson, A. Golanski, H.K. Haugen, L.M. Howe and J.A. Davies, Rad. Effects Letters, **50**, 125 (1980).

[81] S. Ahmad, B.W. Farmery and M.W. Thompson, Phil. Mag., **A44**, 1387 (1981).

[82] G.H. Vineyard, Rad. Effects, **29**, 295 (1976).

[83] M.T. Robinson and O.S. Oen, Appl. Phys. Lett., **2**, 30 (1963).

[84] K. Guttner, H. Ewald and H. Schmidt, Rad. Effects, **13**, 111 (1972).

[85] M. Yoshida, J. Phys. Soc. Japan, **16**, 44 (1961).

[86] J.R. Beeler, Jr. and P.G. Besco, J. Appl. Phys., **34**, 2873 (1963).

[87] M.T. Robinson and I.M. Torrens, Phys. Rev., **B9**, 5008 (1974).

[88] D.K. Hutchence and S. Hontzeas, Nucl. Instrum. and Methods, **116** 217 (1974).

[89] D.A. Eastham, Nucl. Instrum. and Methods, **125**, 277 (1975).

[90] T. Ishitani, R. Shimizu and K. Murata, Jap. J. Appl. Phys., **11**, 125 (1972).

[91] J.E. Robinson, Rad. Effects, **23**, 29 (1974).

[92] P. Sigmund, Rad. Effects, **1**, 15 (1969).

[93] M.J. Norgett, M.T. Robinson, and I.M. Torrens, Nucl. Eng. Design, **33**, 50 (1974).

[94] Y. Wada and S. Nishimatsu, J. Electrochem. Soc., **125**, 1499 (1978).

[95] L. Mei, M. Rivier, Y. Kwark and R.W. Dutton, J. Electrochem. Soc., **129**, 1791 (1982).

[96] H-J. Kim and C.V. Thompson, to be published

[97] J.E. Palmer, unpublished research.

[98] W.A. Johnson and R.F. Mehl, Trans. AIME, **135**, 416 (1939).

[99] G.F. Bolling and W.C. Winegard, Acta Metall., **6**, 283 (1958).

[100] P. Gordon and T.A. El-Bassyouni, Trans. Am. Inst. Min. Engrs., **233**, 391 (1965).

[101] S.K. Dutta and R.M. Spriggs, J. Am. Ceram. Soc., **53**, 61 (1970).

[102] R.S. Gordon, D.D. Marchant and G.W. Hollenberg, J. Am. Ceram. Soc., **53**, 399 (1970).

[103] J.E. Palmer, C.V. Thompson and H.I. Smith, to be published in J. Appl. Phys.

[104] P.B. Hirsch, et. al., **Electron Microscopy of Thin Crystals**, Robert Krieger Publishing, New York, N.Y., 1965.

[105] **TRIM-86**, IBM PC version, copyright 1986 by J.F. Ziegler, J.P. Biersack and U. Littmark.

[106] J.E. May and D. Turnbull, Trans. AIME, **212**, 773 (1958).

[107] S.R.J. Brueck, B-Y. Tsaur, J.C.C. Fan, D.V. Murphy, T.F. Deutsch and D.J. Silversmith, Appl. Phys. Lett., **40**, 895 (1982).

[108] T.H. Englert, G. Abstreiter and J. Pontcharra, Solid State Commun., **23**, 31 (1980).

[109] M. Chandrasekar, J.B. Renucci, and M. Cardona, Phys. Rev. **B17**, 1623 (1978).

[110] G.A. Sai-Halasz, F.F. Fang, T.O. Sedgwick and A. Segmuller, Appl. Phys. Lett., **36**, 419 (1980).

[111] S.A. Lyon, R.J. Nemanich, N.M. Johnson and D.K. Biegelsen, Appl. Phys. Lett., **40**, 316 1982.

[112] B-Y. Tsaur, J.C.C. Fan and M.W. Geis, Appl. Phys. Lett., **40**, 322 (1982).

[113] T. Nishioka, Y. Shinoda and Y. Ohmachi, J. Appl. Phys., **57**, 276 (1985).

[114] G. Abstreiter, E. Bauser, A. Fischer and K. Ploog, Appl. Phys., **16**, 345 (1978).

[115] S. Ganesan, A.A. Maradudin and J. Oitmaa, Ann. Phys., **56** 556 (1970).

[116] F. Cerdeira, C.J. Buchenauer, F.H. Pollak and M. Cardona, Phys. Rev. **B5**, 580 (1972).

[117] E. Anastassakis, A. Pinczuk, E. Burstein, F.H. Pollak and M. Cardona, Solid State Commun., **8**, 133 (1970).

[118] E.M. Conwell, Proc. I.R.E., **40**, 1327 (1952).

[119] R.M. Martin, Phys. Rev. **B1**, 4005 (1970).

[120] C. Kittel, **Introduction to Solid State Physics**, 2nd edition, J. Wiley and Sons, New York, 1956.

[121] J.W. Martin and R.D. Doherty, **Stability of Microstructure in Metallic Systems**, Cambridge University Press, Cambridge, 1976, pg. 159.

[122] J.F. Nye, **Physical Properties of Crystals**, Oxford University Press, London, 1957.

[123] H. Strack, J. Appl. Phys., **34**, 2405 (1963).

[124] T. Itoh and I. Ohdomari, J. Appl. Phys., bf 41, 434 (1970).

[125] R.L. Minear, D.G. Nelson and J.F. Gibbons, J. Appl. Phys., **43**, 3468 (1972).

[126] K.C. Russell, to be published in **Progress in Materials Science**, J. Christian, P. Haasen and T.B. Massalski, eds., Oxford Univ. Press.

[127] V.F. Stas and L.S. Smirnov, Rad. Effects, **49**, 165 (1980).

[128] O. Meyer and J.W. Mayer, J. Appl. Phys., **41**, 4166 (1970).

[129] E.W. Maby, J. Appl. Phys., **47**, 830 (1975).

[130] G. Holmén, S. Peterström, A. Burén and E. Bogh, Rad. Effects, **24**, 45 (1975).

[131] G. Holmén, A. Burén and P. Högberg, Rad. Effects, **24**, 51 (1975).

[132] I. Golecki, G.E. Chapman, S.S. Lau, B-Y. Tsaur and J.W. Mayer, Phys. Letters, **71A**, 267 (1979).

[133] R.G. Elliman, S.T. Johnson, K.T. Short and J.S. Williams, Mat. Res. Soc. Symp. Proc. **27**, 229 (1984).

[134] R.G. Elliman, S.T. Johnson, A.P. Pogany and J.S. Williams, Nucl. Instr. Meth. **7/8**, 310 (1985).

[135] J.S. Williams, R.G. Elliman, W.L. Brown and T.E. Seidel, Phys. Rev. Lett., **55**, 1482 (1985).

[136] R.G. Elliman, J.S. Williams, D.M. Maher and W.L. Brown, Mat. Res. Soc. Symp. Proc., **51**, 319 (1986).

[137] R.G. Elliman, J.S. Williams, W.L. Brown, A. Leiberich, D.M. Maher and R.V. Knoell, presented at the 1986 Fall Mat. Res. Soc. Symp. A: "Beam-Solid Interactions and Transient Processes", and to be published.

[138] G. Holmén, J. Linnros, and B. Svennson, Appl. Phys. Lett. **45**, 1116 (1984).

[139] J. Linnros, B. Svennson and G. Holmén, Phys. Rev. **B30**, 3629 (1984).

[140] J. Linnros, B. Svennson and G. Holmén, Phys. Rev. **B32**, 2770 (1985).

[141] J. Linnros and G. Holmén, J. Appl. Phys., **59**, 1513 (1986).

[142] G.L. Olson, S.A. Kokorowski, J.A. Roth, and L.D. Hess, Mat. Res. Soc. Symp. Proc. **13**, 141 (1983).

[143] C.V. Thompson, private communication.

[144] J.C. Bravman and R. Sinclair, J. Electron Microscopy Technique, **1**, 53 (1984).

[145] O.W. Holland and J. Narayan, Appl. Phys. Lett., **44**, 758 (1984).

[146] S.M. Sze, **The Physics of Semiconductor Devices**, 2nd ed., John Wiley and Sons, New York, N.Y., 1981, pp. 850-852.